Damping Formulations in Substructure Synthesis

by

Homero L. Gutierrez, Jr.

S.B., Massachusetts Institute of Technology (1993)

Submitted to the Department of Aeronautics and Astronautics
in partial fulfillment of the requirements for the degree of

Master of Science in Aeronautics and Astronautics

at the

MASSACHUSETTS INSTITUTE OF TECHNOLOGY

May 1994

Author_____
Department of Aeronautics and Astronautics
May 6, 1994

Certified by_____
Professor Edward F. Crawley
Department of Aeronautics and Astronautics
Thesis Supervisor

Certified by_____
Dr. Myun C. Kim
The Aerospace Corporation
Thesis Supervisor

Accepted by_____
Professor Harold Y. Wachman
Chairman, Department Graduate Committee

Damping Formulations in Substructure Synthesis

by

Homero L. Gutierrez, Jr.

Submitted to the Department of Aeronautics and Astronautics
on May 6, 1994, in partial fulfillment of the
requirements for the degree of
Master of Science in Aeronautics and Astronautics

Abstract

Experimental substructure synthesis was performed as part of an investigation into the formulation of the system modal damping matrix. Typically in the aerospace industry, substructure models are coupled together into a system model for dynamic loads analyses, such as is done for a launch vehicle and its payload. The system modal mass and stiffness matrices are diagonal, but the modal damping matrix will often contain off-diagonal terms which couple the equations of motion. For simplicity, these terms are usually neglected or approximate techniques are used to diagonalize the matrix. Studies have shown that such approximations can sometimes lead to significant errors in response and load predictions. To provide experimental data, tests were conducted on two generic substructures that could be physically coupled. In addition, passive damping in the form of a constrained viscoelastic material was added in certain tests to one of the substructures in order to increase the amount of damping. The mode shapes, natural frequencies, and damping ratios for each substructure were obtained in mode survey tests, and the results were used to update initial finite element models. The models were analytically coupled by means of the Component Mode Substitution Method, and mode survey tests of the coupled system showed that the predicted modes agreed quite well with the measured modes. Four methods were then used to obtain the system modal damping matrix from substructure test results. Transient response testing was performed with and without the added damping to investigate the different formulations. The measured responses were compared to analytical predictions obtained by integrating the equations of motion in generalized coordinates. In general, no significant differences were seen between the methods when the responses were plotted. More detailed analysis revealed that the method that retained the off-diagonal terms did slightly better on average than the diagonal matrix formulations; however, the variations should be considered minimal. The use of more complex test articles with higher levels of damping should provide a clearer indication of the accuracy of the various damping formulations.

Thesis Supervisor: Dr. Edward F. Crawley
Title: Professor of Aeronautics and Astronautics

Thesis Supervisor: Dr. Myun C. Kim
Title: Engineering Specialist, The Aerospace Corporation

Acknowledgments

The research performed for this thesis was conducted at The Aerospace Corporation in El Segundo, California. My six-month stay there was part of the third work assignment of the MIT Engineering Internship Program, and it followed two consecutive summer internships at the same company. During this association with Aerospace, I had the privilege of working in the Structural Dynamics Department with a group of engineers that I admire greatly. The level of experience and expertise found in the department was inspiring to me, and I sought to emulate their commitment to excellence. I would like to thank Aerospace for the opportunity to work in such a professional environment and to allow me the chance to grow as an engineering student.

A number of people at Aerospace should be mentioned specifically for their invaluable help and support. Dr. Alvar Kabe first took me under his wing almost three years ago and sparked my interest in the field of structural dynamics. As my supervisor, he always had time to check my progress and serve as both a teacher and an advisor. Even after new duties occupied more of his time, he never hesitated to provide advice and encouragement. Dr. Myun Kim, my mentor during the project, offered his unique insight and knowledge, which I could not have done without. He unselfishly gave of his time, and I am extremely grateful for his patience with me. I must also acknowledge my manager, Dr. S. Sam Lee, for his help with the many questions that I posed to him. His assistance was very beneficial, and it ensured the progress of my work. In addition, I am indebted to all the other members of the Structural Dynamics Department, as well as the Titan IV program for the funding that it provided.

I spent countless hours in the Dynamics and Control Laboratory at Aerospace, and I owe many thanks to Dan Marten, Don Taylor, and Marc Macon for their contributions. When problems arose during testing or when I was unsure about something, they could be counted on to lend a hand or offer suggestions. I cannot forget to mention Ed Henrich, who was performing his own series of experiments beside me in the lab. His thought-provoking comments were insightful, and I learned many things from him. I enjoyed sharing my experiences with fellow EIP students Tim Glenn and Jim Miskel. I was also fortunate to come to know Rob Cuddy as a close friend. During my first summer at Aerospace, we shared an office, and from that time on, he was an incredible inspiration to me. I was appreciative

of his constant concern, and I greatly admired his deep faith. Professor Edward Crawley, my advisor at MIT, has been and continues to be a source of encouragement for me. I am grateful to him for taking the time to meet with me in Los Angeles and provide vital input to my project.

I must recognize the Taco Bell on Sepulveda in Manhattan Beach for all of the dinners I picked up at its drive-thru after many late nights of testing. Thanks are also in order to all of the Bolo players for those vicious tank battles we had during lunch. I often needed those breaks at midday.

On a serious note though, I extend a heartfelt thank you to my family for their unconditional love and support over the years. I dedicate this thesis to them. And last, but certainly not least, I thank God for His love and strength. With Him, all things are possible.

Contents

List of Figures

List of Tables

Chapter 1

Introduction

Before the details of this project are given, it is important to begin with some introductory material that describes the larger picture that surrounds this research. The role of structural dynamic models in the loads analysis of a launch vehicle and its payload is explained, and some basic equations are presented. The motivating factors leading to this work are then discussed, followed by the general approach that was used to meet the stated goals.

1.1 Background

1.1.1 Importance of Structural Dynamic Models

Substructure modal synthesis techniques are widely used in the aerospace industry as a means of coupling component models into an overall system model for dynamic loads analyses. This coupling approach is frequently required because of the complexity of large aerospace structures. The number of degrees of freedom (DOF's) contained in a finite element model of the complete system is often too large to be accommodated on even the most powerful of computers. In addition, it is normal for different organizations to be responsible for different components of such systems. The creation of component-level models is therefore a common occurrence, and a need arises for their assembly into a coupled model.

Accurate coupled dynamic models are of utmost necessity when predicting the flight loads experienced by a spacecraft as it is boosted by a launch vehicle. The maximum loads

generally are inertial in nature and are the result of transient flight excitations. Examples of such disturbances include liftoff, gusts, engine ignition and shutdown, payload fairing jettison, and stage separation. The response of the flight vehicle to these forces is a function of the dynamic properties of not only the spacecraft, but the launch vehicle as well. It is these dynamic characteristics that must be accurately captured in the models in order to provide confidence that the predicted loads are reliable estimates.

Initial finite element models, however, typically incorporate approximations of various properties into the modeling process. This unavoidably introduces errors and leads to an inaccurate representation of the desired dynamic properties. Another source of error occurs when an insufficient number of degrees of freedom is present in the model. This becomes a problem when important motion in the frequency range of interest cannot be described by the limited number of coordinates available.

To remedy these deficiencies in the analytical models, a mode survey test is often performed. This test experimentally determines the dynamic characteristics of the structure in a desired frequency range. The data can then be used to adjust the analytical models and yield a better representation of the actual flight vehicles. It is important that the mode survey test be conducted properly and that the results be interpreted adequately. The use of erroneous data can only compound the limitations of the original models, which defeats the purpose of the test.

1.1.2 Mathematical Model of Multiple-Degree-of-Freedom Systems

The dynamic models discussed previously are based upon the equations of motion of a multiple-degree-of-freedom (MDOF) system. Although all structures are continuous, and hence contain an infinite number of DOF's, they can be fairly well approximated by a small subset of these at low frequencies. The finite element method, in particular, discretizes a continuous structure so that the motion of a point on the structure can be expressed in terms of the motion at a finite number of selected points known as nodes.

The equations of motion can be expressed as a set of simultaneous, linear, time-invariant, second-order differential equations. When written compactly using matrix notation, they take the form

$$M\ddot{x}(t) + C\dot{x}(t) + Kx(t) = F(t) \tag{1.1}$$

where M is the mass matrix, C is the damping matrix, K is the stiffness matrix, F is a vector of applied forces, and x is a vector containing the displacements of the nodes in physical coordinates. For a model with N DOF's, M, C, and K are of size $N \times N$, while F and x are of order N. The matrices M and K can be obtained directly from a finite element model, and the forcing functions in F come from a combination of previous flight measurements and other sources. The damping matrix, C, on the other hand, is much more difficult to obtain for a complex structure.

The type of damping represented in Equation 1.1 is referred to as viscous damping. This energy dissipation mechanism is modeled as a rate dependent form of energy loss, and it is an extreme simplification of the more complex phenomena present in actual structures. The sources of other types of damping include structural damping, friction, stick-slip behavior, and free play. The viscous damping model is a linear model that approximates the average contribution of all these phenomena. Although methods exist to generate a C from experimental results (see [6]), this is usually not necessary, as will be shown in the next section.

1.1.3 Modal Coordinates

As stated previously, Equation 1.1 represents a set of simultaneous differential equations. Frequently, either some or all of the coefficient matrices will not be diagonal and will contain off-diagonal terms. The differential equations, therefore, are not independent, but rather are coupled by these terms. Solving these equations becomes a much more difficult process.

One usual way to deal with such a situation is to perform a coordinate transformation. By considering the undamped system in the absence of external forces, the *normal modes* can be determined by solving the eigenvalue problem

$$K\Phi = M\Phi\Omega^2 \tag{1.2}$$

where Ω^2 is an $N \times N$ diagonal matrix consisting of the squares of the circular natural frequencies, and Φ is an $N \times N$ matrix whose ith column contains the normal mode associated with the ith natural frequency. The normal modes, if mass normalized, satisfy the

two orthogonality conditions given by

$$\Phi^T M \Phi = I \tag{1.3}$$

and

$$\Phi^T K \Phi = \Omega^2 \tag{1.4}$$

where I is the $N \times N$ identity matrix. By introducing the transformation $x = \Phi q$ into Equation 1.1 and then premultiplying both sides by Φ^T, the equations of motion in modal coordinates can be expressed as

$$(\Phi^T M \Phi)\ddot{q} + (\Phi^T C \Phi)\dot{q} + (\Phi^T K \Phi)q = \Phi^T F \tag{1.5}$$

Utilizing Equation 1.3 and Equation 1.4, this simplifies to

$$I\ddot{q} + \Gamma\dot{q} + \Omega^2 q = \Phi^T F \tag{1.6}$$

where I is the modal mass matrix, Γ is the modal damping matrix, and Ω^2 is the modal stiffness matrix.

Both I and Ω^2 are diagonal, and for special cases of C, Γ is also diagonal, which results in uncoupled equations of motion in modal coordinates. There are N independent second-order linear differential equations, each representing a single DOF oscillator, and the solutions of these equations for general excitation are well known (refer to [22]). The type of damping that produces a diagonal Γ is known as proportional or classical damping. In this case, Γ can be written as

$$\Gamma = \begin{bmatrix} \ddots & & \\ & 2\zeta_i\omega_i & \\ & & \ddots \end{bmatrix} \tag{1.7}$$

Caughey showed in [4] that proportional damping is equivalent to C being expressed as a power series of the mass and stiffness matrices as follows

$$C = \sum_i a_i M^i + \sum_j b_j K^j \tag{1.8}$$

For non-proportionally damped systems (i.e., systems in which Γ contains off-diagonal terms), the equations of motion given by Equation 1.6 are coupled. The corresponding

solution is approximated by a direct integration of the equations. This technique becomes very costly as the size of the problem increases, and one usual simplification is to force proportional damping by setting all the off-diagonal elements of Γ to zero. Other methods construct an approximate diagonal Γ by different means. It is the formulation of the modal damping matrix which is the focus of the research being presented. This is done within the context of experimental substructure modal synthesis.

1.2 Motivation

The diagonalization of the system modal damping matrix has historically been done by aerospace companies conducting coupled loads analyses. The assumption of light damping is used as the basis for neglecting the off-diagonal terms, which are typically small when compared to the corresponding diagonal elements. Sometimes, Γ is not computed directly, but rather is created by assuming a uniform damping value such as 1% for the ζ_i in Equation 1.7.

Recently, the use of a diagonal Γ in loads analyses has been questioned. An increasing number of studies have revealed cases where such decoupling approximations lead to significant errors in response calculations (see [23], [16], [28], and [29]). An extreme example occurred in August, 1987, during the verification loads analysis of STS-26/TDRS. For a certain liftoff loads case, the peak acceleration response of a TDRS antenna was computed to be $27\,g$ when a diagonal Γ was used. When the analysis was performed again, but this time with the off-diagonal terms retained, the predicted acceleration was reduced to $7.3\,g$. This is documented in [27].

Another instance is shown in [16], which contains a description of a Titan IV stage I shutdown loads analysis. Because of the large critical damping ratios of certain engine modes ($\zeta \approx 26\%$), the fully-populated Γ had fairly large off-diagonal terms. The relative sizes of these terms can be characterized by defining a coupling index matrix α, where

$$\alpha_{ij} = \sqrt{\frac{\Gamma_{ij}^2}{\Gamma_{ii}\Gamma_{jj}}} \tag{1.9}$$

For the case of the Titan IV loads analysis, the largest coupling index value was $(\alpha_{ij})_{\max} = 0.814$. It was shown that appreciable discrepancies arose in the predicted spacecraft loads

when the off-diagonal terms were ignored.

Examples such as the previous two have led to debates in the aerospace industry over whether the coupled damping (i.e., fully-populated Γ) approach should be required for all future loads analyses or only in certain cases. This motivated the project presented herein, and one of the main goals was to provide experimental data for the debate. This was accomplished by performing component modal synthesis on two generic substructures and investigating various methods of creating the system modal damping matrix. Another priority was to compare experimental and analytical results at all stages. The approach that was followed to achieve these broad objectives is given in the next section.

1.3 Approach

Figure 1.1 is a flow diagram that shows the major steps involved in the investigation into modal damping formulations. The initial task was to construct two substructures on which

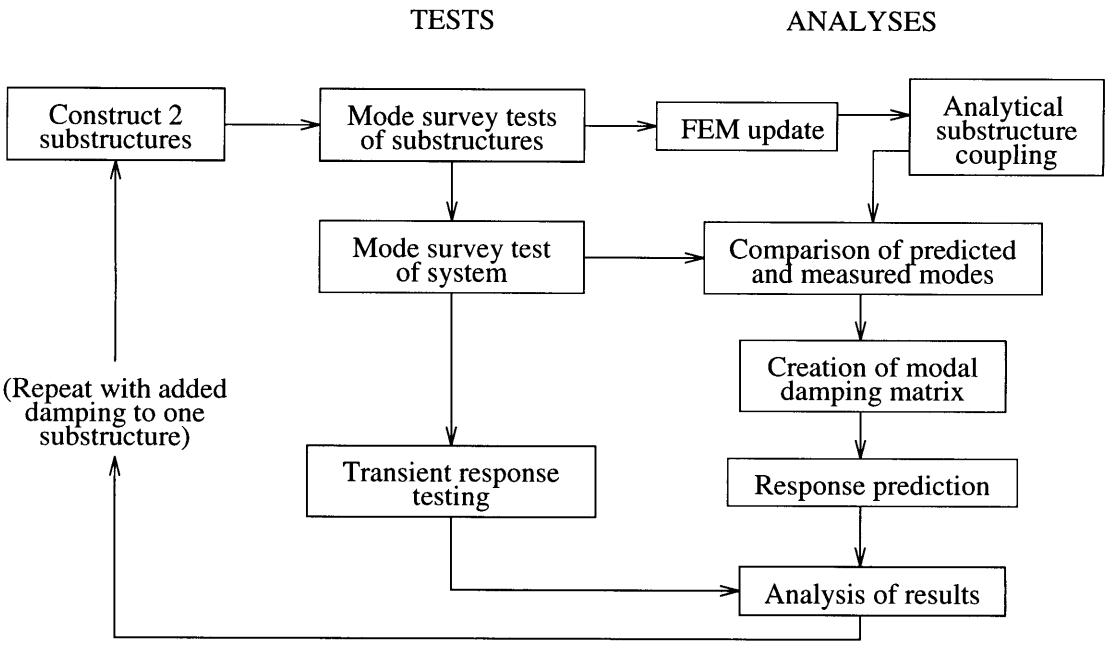

Figure 1.1: Flow diagram showing key steps of the project.

the tests would be performed, and it was required that these substructures be able to be coupled into a system. Throughout the rest of this report, one of the substructures will be referred to as BV (booster vehicle) and the other as SV (space vehicle). The similarity to any

specific launch vehicle and spacecraft, however, is purely artificial, and the only resemblance occurs in the manner in which the two substructures are coupled. The names are meant to help in visualization purposes. There was no attempt at reproducing the dynamic properties of the complex aerospace structures at the heart of the coupled damping debate.

Once the substructures had been constructed, mode survey tests were conducted in order to determine the mode shapes, frequencies, and damping. The initial finite element models (FEM) were then adjusted so as to better match the measured values. These updated models were used in an analytical coupling procedure to obtain predictions of the modes of the coupled system. A mode survey test of the complete system provided an indication of the success of the analytical method.

The next major phase began with the creation of the system modal damping matrix by four commonly used techniques. The differences between the matrices were studied after a series of transient response tests were performed. The measured responses were compared to responses predicted by solving the equations of motion with the different Γ. This entire process first utilized lightly damped substructures in which only inherent damping was present. To increase the effects of non-proportional damping, damping was added to one of the substructures, and the process was repeated. The results for both cases were compared and used to characterize the effect of the increase in damping as well as to identify any differences in the various damping formulations.

1.4 Outline

The remaining chapters provide a more detailed account of the key elements shown in Figure 1.1. Chapter 2 describes the two substructures, including their dimensions, materials, and configuration. The added damping treatment is also discussed, and the physically coupled system is presented. Chapter 3 is an overview of the finite element models that were created and the procedures for model reduction and compatibility. Chapter 4 deals exclusively with the mode survey tests on the substructures and the coupled system. The hardware and software that were used are described, as well as the method used to extract the modes. The results are summarized and conventional mode checks are made. This leads to the updates of the finite element models in Chapter 5, which are then analytically coupled in Chapter 6. The exact details of the damping formulations are given in Chapter 7, and

the transient response testing conducted to compare the methods is the topic of Chapter 8. The conclusions that are made based on the results are offered in Chapter 9. In addition, recommendations for further work are suggested. The data files for the finite element models and some of the important FORTRAN programs that were written are provided in the appendix.

Chapter 2

Description of Test Articles

The two substructures constructed for the project utilized material from an existing test article located in the Dynamics and Control Laboratory of The Aerospace Corporation. The previous test article was the object of a study known as the Structural Dynamics Response Experiment. It was decided to dismantle the structure and reconfigure the parts into two substructures for use in the current project. As a result, some of the same characteristics were maintained in the new test articles. The substructures can be described as building-like, shear structures made from aluminum and steel and possessing one or more distinct levels or "floors." Vertical columns connect the floors and contribute to the flexibility of the substructures, while the floors themselves contribute most of the mass. The columns have a rectangular cross section that leads to a primary bending direction at low frequencies. The design of the substructures was somewhat influenced by the desire to mimic a launch vehicle / payload configuration. The result was one large substructure (BV) and a smaller one (SV) that can be placed atop it to form a coupled system. Detailed descriptions of these test articles are presented in the following sections, followed by a discussion of the added damping treatment and the coupled structure.

2.1 Substructure BV

Figure 2.1 shows a three-view of the test article referred to as BV. Substructure BV consists of three floors and is clamped at its base. The vertical y-direction beams are made from aluminum 6061-T6 with cross-sectional dimensions of $1'' \times \frac{1}{4}''$. The eight upper beams are each $11\frac{1}{2}''$ long, but $\frac{3}{4}''$ is captured by the joint on each end, resulting in only $10''$ of

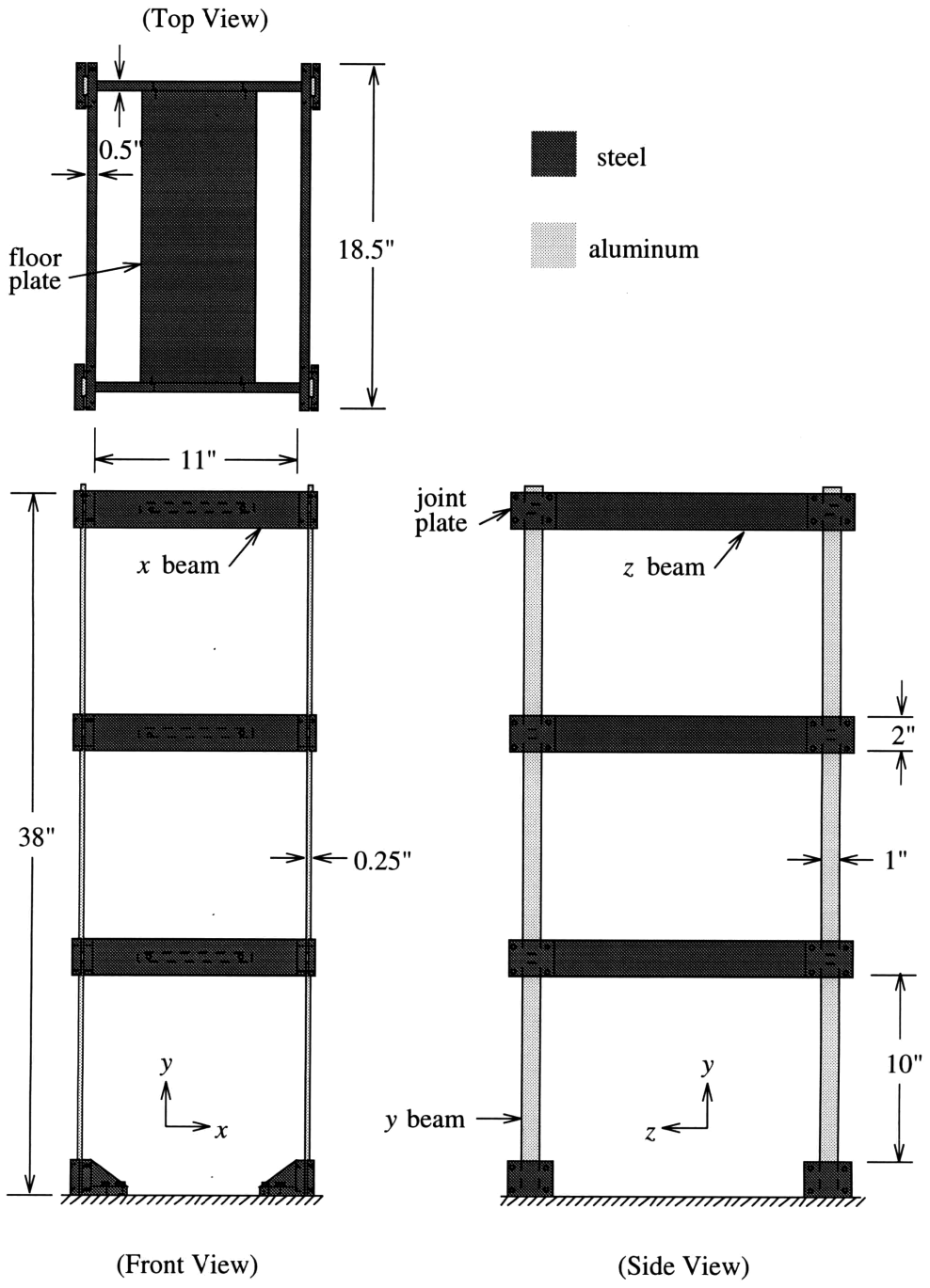

Figure 2.1: Three-view of substructure BV.

exposed length. The four lower beams are $12\frac{3}{4}''$ long and have $\frac{3}{4}''$ captured at the top joint and $2''$ captured at the base joint, thus still leaving $10''$ exposed. Each floor has a frame made up of four steel beams ($2'' \times \frac{1}{2}''$ cross section) connected by two flat-head screws at each joint. The beams in the x direction are $11''$ long, while the ones in the z direction are $18\frac{1}{2}''$ long. In the middle of every floor lies a steel plate of dimensions $6'' \times \frac{1}{2}'' \times 15\frac{1}{2}''$. These plates help to increase the amount of mass at the floor levels. They are attached to the x-direction beams by a pair of Allen-head screws on each end. A close up of a typical joint is shown in Figure 2.2.

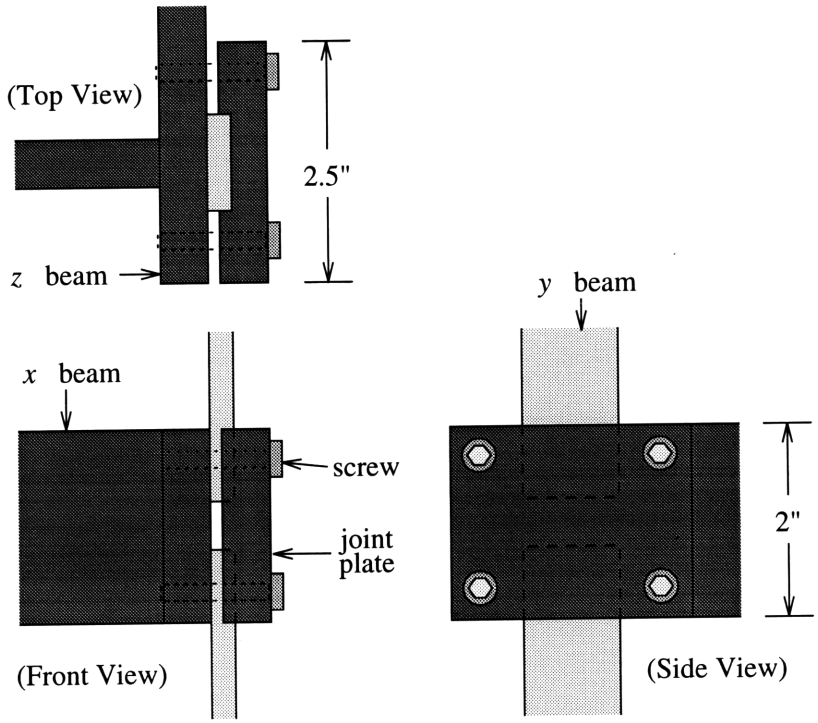

Figure 2.2: Three-view of typical joint.

The aluminum beams enter from the top and bottom and lie flat against a z-direction beam. They are held in place by a notched, steel joint plate that has four Allen-head screws firmly connecting it to the z-direction beams. In addition, four filler bars are used at the top level to maintain the proper orientation of the joint plates. Later, it will be shown that these filler bars are removed when the substructures are physically coupled. A torque wrench was used to ensure that the screws were indeed tight and that they were all pre-loaded with approximately the same amount of torque. Loose joints were not desirable

since any relative motion would lead to friction and cause nonlinear effects to arise during testing. The base joints have four additional, larger screws that are used to attach the entire structure rigidly to a base. This base is itself bolted and cemented to the floor of the laboratory. This enables the structure to achieve a near-perfect cantilevered boundary condition and reduces the chance of dynamic contamination resulting from coupling of the structure and the base. This is extremely important in order to allow pure modes of the structure to be extracted during the testing and analysis phase.

The vertical beams are oriented in such a way that the structure is significantly less stiff in the x direction. Physically, this means that it is easier to cause a displacement in this direction than in either the y or z directions. In the frequency range of interest of 0–60 Hz, the motion of the structure is primarily composed of horizontal movement in the xz plane of each floor. The floors themselves behave basically as a rigid body during such motion. This characteristic is the reason why the substructures are referred to as shear structures. The floors tend to shear with respect to one another and remain horizontal. As will be seen, the modes fall into three categories that are defined by the motion of the floors. They are

- x-bending modes, in which the floors displace only in the x direction,
- z-bending modes, in which the floors displace only in the z direction, and
- torsion modes, in which the floors displace in both directions, resulting in motion that appears as rotation about the y axis.

Motion in the axial (y) direction, however, is not appreciable at these low frequencies. Such properties of the structure helped to dictate the placement of sensors and the location of shakers during the mode survey tests, as will be discussed in Chapter 4.

2.2 Substructure SV

Substructure SV is much smaller and lighter than BV, consisting of only one floor. It has the same overall dimensions for both length and width, which enables it to be easily placed on top of BV. Figure 2.3 shows the details of SV. Four vertical aluminum beams support the single floor that is comprised of four steel beams, as before. Replacing the steel plates found in BV is an aluminum cross-beam with a $\frac{1}{2}''$ square cross-section. Angled brackets are used to connect it to the x-beams. A slit in the cross-beam allows a thinner, vertical

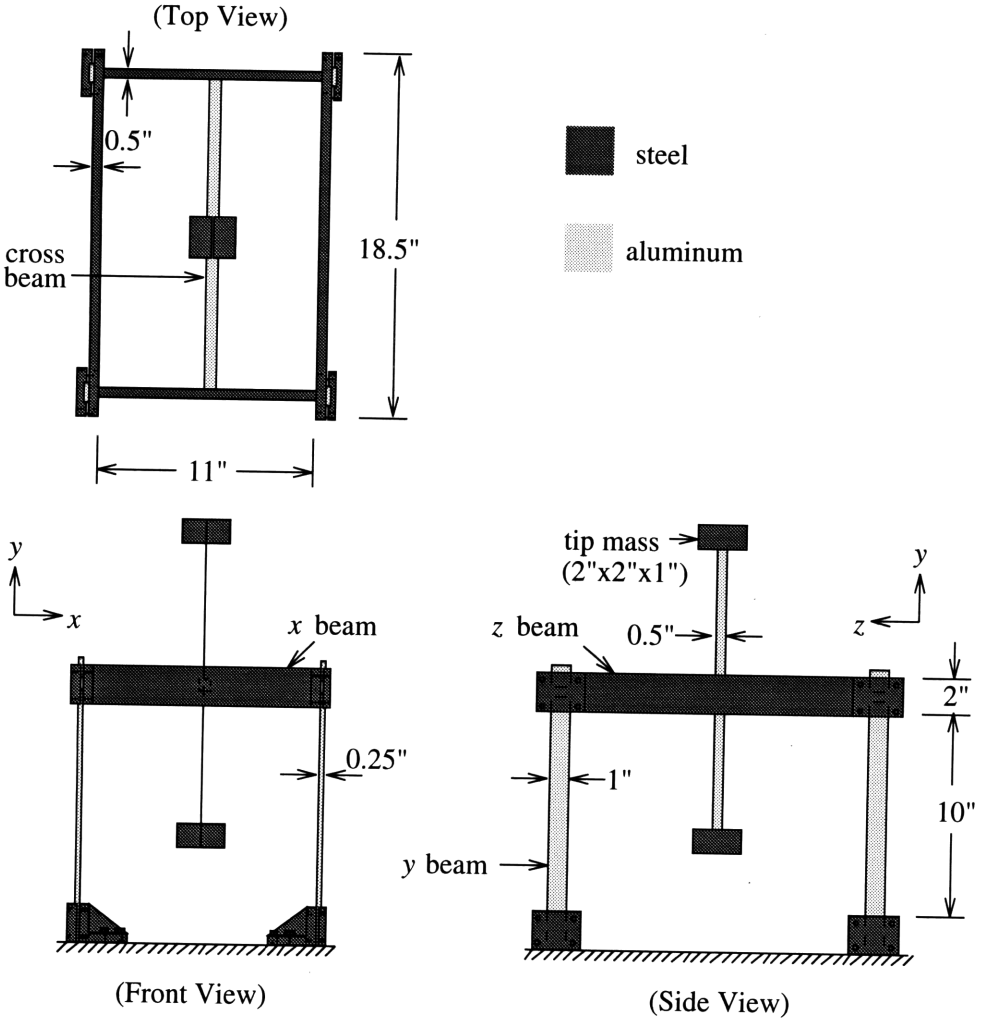

Figure 2.3: Three-view of substructure SV.

aluminum beam ($\frac{1}{8}'' \times \frac{1}{2}'' \times 16\frac{1}{2}''$) to be placed through it. Clamped about the ends of the beam are steel tip masses. This results in flexible appendages with low frequency bending modes. The joints are similar to those of BV, including the use of filler bars, and the same type of base joints permit a cantilevered support for testing. This time, only $\frac{3}{4}''$ of each column is captured at the base joints in order to allow consistency in the coupled structures. To compensate for the missing lengths, filler bars are also used in the base joints. SV can also be described as a shear structure, and the same three types of modes—x-bending, z-bending, and torsion—are present. Due to the lower mass and increased stiffness arising from a shorter height, these modes occur at higher frequencies than the corresponding BV modes. The antenna modes, however, introduce new low frequency modes into the system.

Axial motion of the columns is negligible, and the same holds for the antenna assembly. This fact helps to minimize the number of sensors required during modal testing.

2.3 Added Damping Treatment

Various options were considered for increasing the amount of damping in one of the substructures. It was desired that the damping have a minimum effect on the mass and stiffness properties of the substructure so that a better comparison could be made between the lightly damped and added damping cases. This would enable any differences in the results to be almost directly linked to the increased damping.

The use of sliding friction as a means of energy dissipation was dismissed because of the nonlinearities that it would introduce. The analysis would be more difficult since the measurements would be highly sensitive to the level of excitation during testing. Friction could have been implemented in the project by allowing a floor beam of a substructure to rub against an external piece of material. Although not chosen, this method did lead to a similar concept that was eventually used.

Another option that was looked into involves dampers that work on the basis of kinetic energy. Some are characterized by the movement of one or more particles within a container. As the container vibrates, the particles collide with one another and with the container walls, thereby converting some of the kinetic energy to random heat energy during the inelastic collisions. A series of impact hammer tests were performed on a cantilevered beam with a film container filled with sand placed at the free end of the beam. The damping ratio of the first bending mode did reach as high as 14%, but this method was not chosen because of the nonlinearity problems that would be introduced. The response would not have been linear with respect to the excitation. The added mass of the sand and container, however, was not a concern since the original substructure could be modified by including a rigid mass of the same weight at the same location.

Just as dampers exist that work on the basis of kinetic energy, there are corresponding ones that depend on strain energy. Viscoelastic materials (VEM's) are probably the most familiar and widely used damping materials in this category. They dissipate energy as they undergo strain, and they are more effective when this strain is shear rather than extensional. To help induce shear strain, a constraining layer can be bonded to one side of the VEM

while the opposite side is in contact with the structure of interest. For a fixed thickness of VEM, the amount of damping can be increased by allowing the thickness of the constraining layer to approach that of the structure. For a beam, this is best achieved by splitting it in half along its length and placing a thin VEM layer in between. The resulting composite beam will be significantly more damped, but at the cost of a slight decrease in stiffness.

All of the above methods are passive damping mechanisms. The use of an active damping system was not considered because of the increased complexity that would be involved. It should be noted that piezoelectric materials, which are commonly used in active control systems, can also be incorporated into a passive damping mechanism, as described in [11]. This method was another possibility, but was not chosen because of constraints that arose during the project.

The primary limiting factor that eventually dictated the choice of damping was the time that was available for testing. Severe time constraints favored a method that could be easily added and removed with a minimum amount of assembly. This would allow tests to be conducted rapidly, and in any order, on the damped and undamped configurations. For example, if a test had to be redone on the undamped structure after the damping mechanism had been added, there would be no problem in removing it in a short amount of time. This scenario actually arose during the project and confirmed the rationale behind this requirement. In addition, it was desired that the damping have an effect on a number of modes and not just on one primary mode. As mentioned before, the added damping should also not significantly change the mass or stiffness properties of the undamped structure.

The option of using two half-thickness vertical beams with a layer of VEM in between was not chosen because it did not meet the first requirement. If, for instance, the four lower beams of BV were replaced with the composite beams, the amount of disassembly and reassembly time would be appreciable. Also, it would be extremely difficult to reproduce the same conditions that existed before the structure was taken apart. Any changes that occurred would be difficult to characterize. The use of piezoelectrics on the vertical beams would have led to similar problems. Once the piezoelectric was bonded to the beam, it would be very difficult to remove. This would mean that a separate set of beams would have to be on hand, but then the same assembly concerns as before would exist.

The design that eventually was accepted involved a combination of the friction idea and the use of constrained VEM. Instead of having one of the horizontal floor beams rub against

an external piece of material, it was decided to place a piece of VEM in between. This setup can be seen in Figure 2.4.

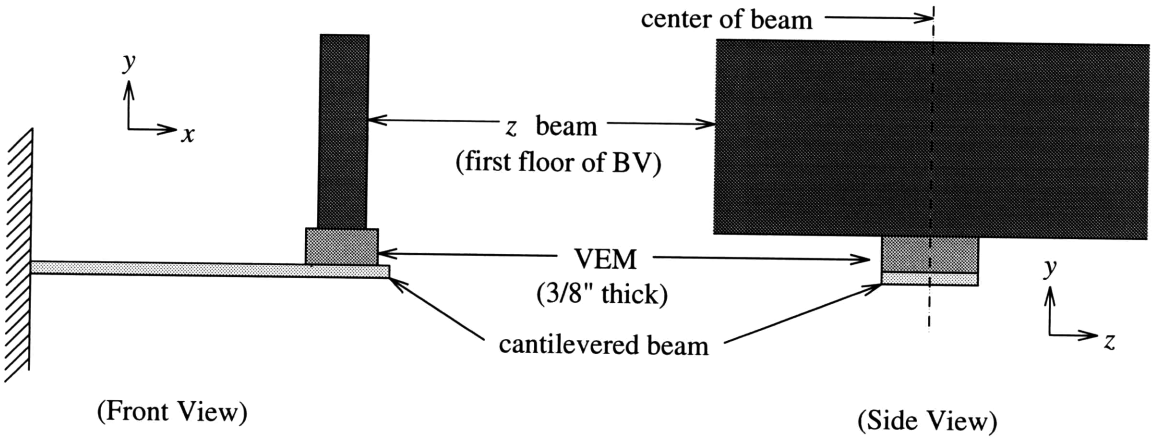

Figure 2.4: Placement of VEM.

A horizontal, cantilevered piece of scrap metal extends under the center of one of the z-direction beams on the first floor of BV. As the beam moves in the xz plane, it places the VEM in shear, which helps to dissipate energy. A side effect is that the VEM adds some of its own stiffness into the system. Although it was hoped that this result could have been avoided, the added stiffness could be accounted for in a fairly simple manner, as will be shown in Chapter 3. It was found that increasing the thickness of the VEM did decrease the amount of stiffness that was introduced; however, this was at the cost of a decrease in the amount of damping. Thus, a compromise had to be made between the two. Several trial thicknesses were tested, and it was found that a $\frac{3}{8}''$ thick piece did provide an adequate amount of damping with an acceptable increase in stiffness. This method did have a greater effect on the damping in the x-bending modes, as would be expected, while it had the least effect on the antenna modes of the coupled system. Since the damping is dependent on the motion of the floor, the higher frequency modes have less added damping because of the smaller amplitude motion.

The specific type of VEM that was used was 3M's SJ 2015 ISD 112, which is appropriate for room temperature conditions. A sample sheet 15 mils thick was obtained, and it was cut into pieces about $1'' \times \frac{1}{2}''$ in size. Twenty-five of these were stacked on top of each other in order to achieve a thickness of $\frac{3}{8}''$. Only pressure is required to adhere the VEM to a surface, and it can be peeled off just as easily. This characteristic was extremely valuable

since it permitted a test with the added damping to be performed within minutes of the completion of a test without the damping.

2.4 Coupled System

In order to couple the substructures together, the base joint plates need to be removed from SV. By then loosening the joint plates on the top level of BV and removing the filler bars, SV's four vertical beams can be slid into the notches of the joint plates. To ensure an exposed beam length of $10''$ and a captured length of $\frac{3}{4}''$ at the joints, two blocks of wood that were $10''$ high were used to brace the top floor of SV and allow it to slide down the desired amount. The screws of the joint plates can then be tightened to secure the beams in place. A view of the coupled system with the added damping treatment can be seen in Figure 2.5.

The coupling of the substructures results in a structure that possesses many of the same properties as its components. As a result, it also resembles a cantilevered, multi-story building frame that deforms primarily in shear. The same types of modes as before can be expected, namely x-bending, z-bending, torsion, and antenna modes. The added damping, when present, is located at the bottom floor.

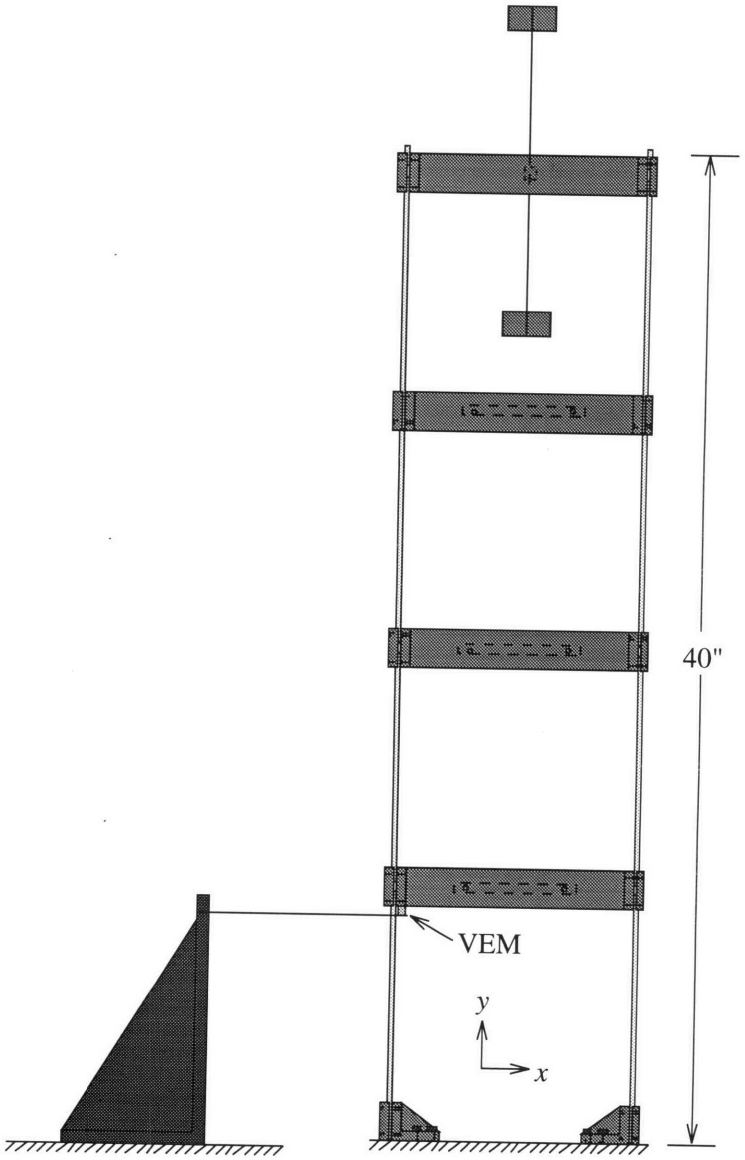

(Front View)

Figure 2.5: Front view of coupled system with added damping.

Chapter 3

Finite Element Modeling

Finite element models serve many important purposes, ranging from static and dynamic analyses to control-oriented applications. An initial finite element model provides a first estimate of the characteristics of the structure being studied. The analytical mode shapes and frequencies can be used in a pre-test analysis to help identify locations for the sensors and actuators of a mode survey test. The results of the mode survey test can then be incorporated in an update of the models in order to provide a better representation of the structure. Consequently, the corrected models allow further analyses to yield more accurate predictions. Because of these reasons, the creation of finite element models of the substructures BV and SV began even before the actual structures were assembled. This chapter describes the general procedure used in developing these models and explains how the critical joint areas were treated. The details of the substructure models are then presented, followed by a discussion of how the number of DOF's was reduced and how the models were modified to enable them to be used in the analytical coupling procedure.

3.1 Methodology

In order to be useful, finite element models must be able to capture the dynamics of a system over a desired frequency range. This can be achieved by ensuring that a sufficient number of DOF's are present in the model so that the motion of the structure can be reproduced throughout the range of frequencies. On the other hand, the inclusion of too many DOF's could lead to a model whose size is unnecessarily large. Such a model would not be efficient since smaller size models could represent the motion accurately at a lower

computational cost. This was kept in mind as the finite element models were created with the use of NASTRAN.

One of the first choices that had to be made involved the selection of the types of elements to use in the models. Since the substructures are made almost entirely of beams, it appeared natural to use beam elements for these components. In NASTRAN, this is accomplished by specifying CBEAM cards for each element. However, CBEAM's can accommodate very complicated beam-like elements, and the actual beams in the structure are simple and symmetric. This meant that the CBAR element could be used instead since CBAR is a bending element that does not account for any complicated behavior. A CBAR card only requires one grid point on either end of the element to be specified, along with one reference grid point to define the element coordinate system. The corresponding PBAR card indicates the material and the geometric properties of the element. For the case of the substructures, CBAR's were used for the vertical beams, the x beams, and the z beams of BV and SV, as well as for the cross beam and tip mass beam of SV. Even though the xz plates located at each floor of BV fit the description of plates rather than beams, their local bending motion occurs at much higher frequencies than the 0–60 Hz range of interest. Thus, they were modeled by CBAR's in order to account for their mass distribution.

It is quite apparent that any local bending modes of the steel beams will occur at high frequencies, and that one element per beam is all that is required in the mesh. However, it is not as apparent if a single element can be used for each of the vertical aluminum beams. To reach a definite conclusion, a simple beam analysis was performed. Each vertical beam can be thought of as having a near-clamped boundary condition on each end. This implies that the actual boundary condition lies between being simply supported and perfectly clamped. As a lower bound, assume a simply-supported condition on each end. From [6], the frequency of the first mode for this case is given by

$$\omega_1 = \frac{\pi^2}{L^2}\sqrt{\frac{EI}{\rho A}} \tag{3.1}$$

where L is the length of the beam, EI is the bending stiffness, and ρA is the mass per unit length. Substituting the values appropriate for the aluminum beams results in

$$\omega_1 = \frac{\pi^2}{(10\,\text{in})^2}\sqrt{\frac{(10^7\,\frac{\text{lb}}{\text{in}^2})(0.0013\,\text{in}^4)}{(0.00025\,\frac{\text{sn}}{\text{in}^3})(0.25\,\text{in}^2)}} = 1425\,\frac{\text{rad}}{\text{s}} \tag{3.2}$$

which implies

$$f_1 = \frac{\omega_1}{2\pi} = \frac{1425 \frac{\text{rad}}{\text{s}}}{2\pi} = 227\,\text{Hz} \tag{3.3}$$

Thus, no local bending will occur below 60 Hz, and a single CBAR can be used for each y beam.

Another type of element that can be found in the models is a concentrated mass. The CONM2 card allows translational and rotary masses to be given at a particular grid point. This enables each tip mass on the antenna assembly of SV to be accounted for by concentrating the mass at its center. This element is also used to distribute the remaining structural mass (i.e, screws, joint plates, accelerometers) not included in the beam elements. The remaining two elements that can be found in both substructure models are described in the following section on the modeling of the joints.

3.2 Model of Joints

The way that the joints were treated played a crucial role in the modeling process. Although they can be considered to be rigid as a first approximation, the joints do contribute some degree of flexibility. If there was to be any hope of adjusting the initial models to better match the experimental results, a way to account for this flexibility was needed. This flexibility would also deal with boundary conditions that were not perfectly clamped.

A typical method used to introduce flexibility is to connect pairs of DOF's by general spring elements. By making a spring extremely stiff, the corresponding DOF's will not have any relative motion between them, and this will nearly represent the enforcement of a rigid connection. Then by making the spring softer, relative motion will begin to occur, thereby allowing some amount of flexibility. In NASTRAN, spring elements can be defined using the CELAS1 card. A pair of DOF's is specified, and the corresponding spring constant is given in a PELAS card.

As an example, consider the interface between one of the vertical beams and the base. Ideally, if the connection was truly clamped, the lower grid would undergo no displacement. In actuality, a small amount of motion will take place. Figure 3.1 shows the method that accommodates such motion. Grid point 1 is the lower point of the beam and grid point 2 is an additional node that is defined to have the same coordinates as 1. Grid point 2 has all of its DOF's fixed in order to represent the base. Each DOF of 1 is connected by a

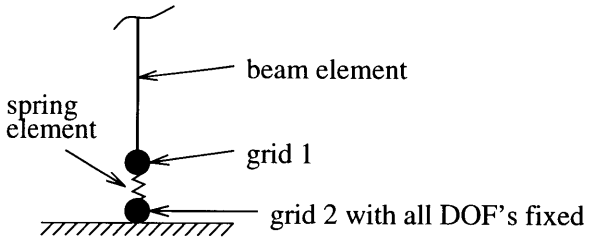

Figure 3.1: Spring elements at base.

spring element to the same type of DOF of 2. In the figure, the grid points are purposely separated in order to emphasize the fact that they are joined by spring elements. Also, only one vertical spring is shown for simplicity. The other two extensional springs and three torsional springs are present in practice. By choosing to soften certain spring constants, the connection can be made to be less stiff in the corresponding directions.

For the other joints not located at the base, a similar method can be employed. Not only are CELAS1 elements used, but RBAR's as well. An RBAR specifies a master-slave relationship between specified DOF's of a master (independent) node and a slave (dependent) node. Figure 3.2 shows a three-view of a typical joint, with the components of the finite element model superimposed on it. These components are detailed further in Figure 3.3. Grids C and D represent the locations where the y beams enter into the joint assembly. Grid A is one end of the x beam and is on the interface between the connecting x and z beams. Grid B is on the centerline of the z beam, but it does not actually represent the end of the beam. The three additional grids (B1, B2, and B3) are defined to coincide with B; however, they are shown displaced in the figure for clarity purposes. RBAR's force these grids to have the same motion as A,C, and D. CELAS1's then tie B1, B2, and B3 to B, thus allowing A,C, and D to undergo relative motion. As before, adjusting the various spring constants will change the amount of flexibility present within the joint.

As can be seen, the actual joint plate is not directly modeled. Its mass, in addition to the remaining mass due to screws and captured beam lengths, is concentrated at B. For the case of joints at the top level of either BV or SV, the grid points B3 and D are not used. A similar use of RBAR and CELAS1 elements can be found in the antenna assembly portion of SV. This option for increased flexibility is introduced at the intersections between the aluminum cross beam and x beams, between the cross beam and tip mass beam, and between the tip mass beam and the tip masses.

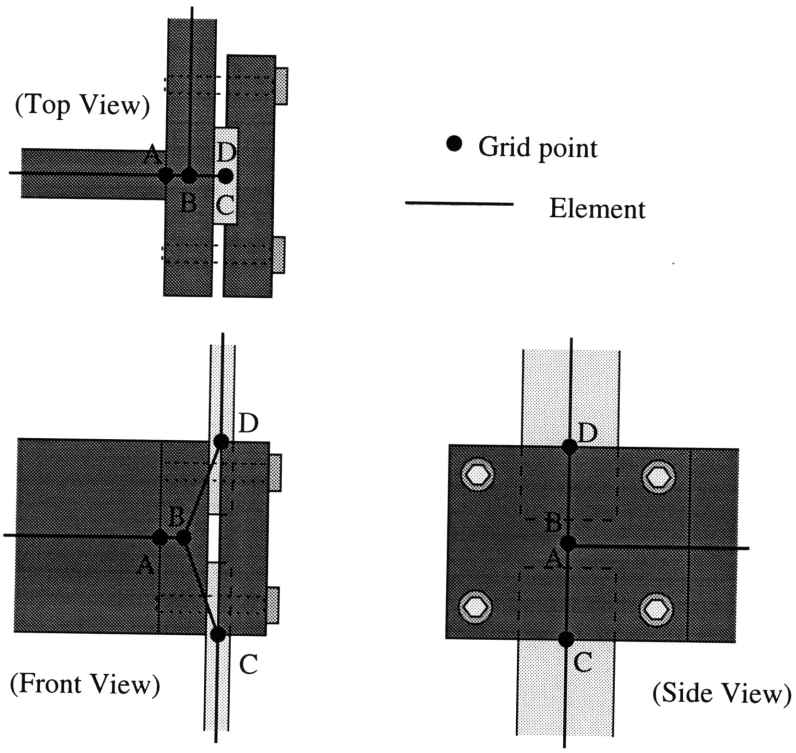

Figure 3.2: Joint modeling.

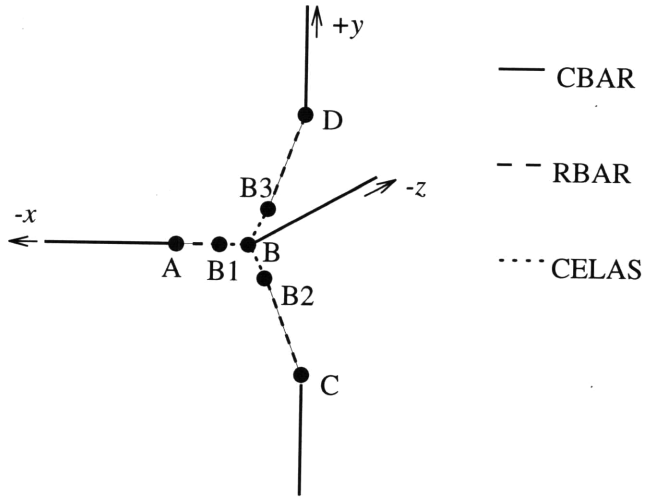

Figure 3.3: Elements used at joints.

3.3 Initial Models

The finite element models of the two substructures were created using the methods described in the previous sections. The coordinates of the grid points were based on physical measurements. Average densities were computed for the different types of beams, and these values were used instead of the typical densities for steel and aluminum that can be found in tables of material properties. The concentrated masses at the joints were obtained by determining the amount of mass not accounted for by the beam elements. An approximate value of the inertia of this mass was computed about the point at which the mass was lumped. To simulate rigid joints, all the spring constants were given values of 10^{10}. This was done for both original models of BV and SV. Figure 3.4 shows the two models side by side. Each line represents some type of element, and each dot is a grid point. Although not indicated in the figure, collocated grid points do exist (as discussed in the previous section). To avoid unnecessary clutter, only a select number of points are labeled. Some of these points will be referred to in Chapter 4 to identify accelerometer and shaker locations.

The initial models allowed six DOF's to be active at every independent node. This resulted in a total of 324 DOF's for BV and 162 DOF's for SV. As a consequence, the mass and stiffness matrices of BV were of size 324×324, and for SV, they were of size 162×162. Normally, NASTRAN reorders these matrices so as to produce matrices of a smaller bandwidth, which helps to reduce the computational time. However, in order not to have to keep track of what the NASTRAN ordering was (which could change if additional nodes were added), it was decided to force the DOF ordering to correspond to the order in which the nodes were numbered. This made the coupling process described in Chapter 6 easier since the mass and stiffness matrices have to be partitioned into interface and non-interface coordinates. The additional computer time was probably negligible since the NASTRAN jobs were sent to a CRAY-2 supercomputer. In addition, a lumped mass approach for creating the mass matrix was selected, which meant that the matrix would be diagonal.

Once all the necessary bulk data cards were entered in the correct format, a real, normal modes analysis was performed in NASTRAN. Analytical modes below 100 Hz were sought, even though the frequency range of interest was below 60 Hz. There was no guarantee that modes slightly higher than 60 Hz would not physically appear at lower frequencies. This

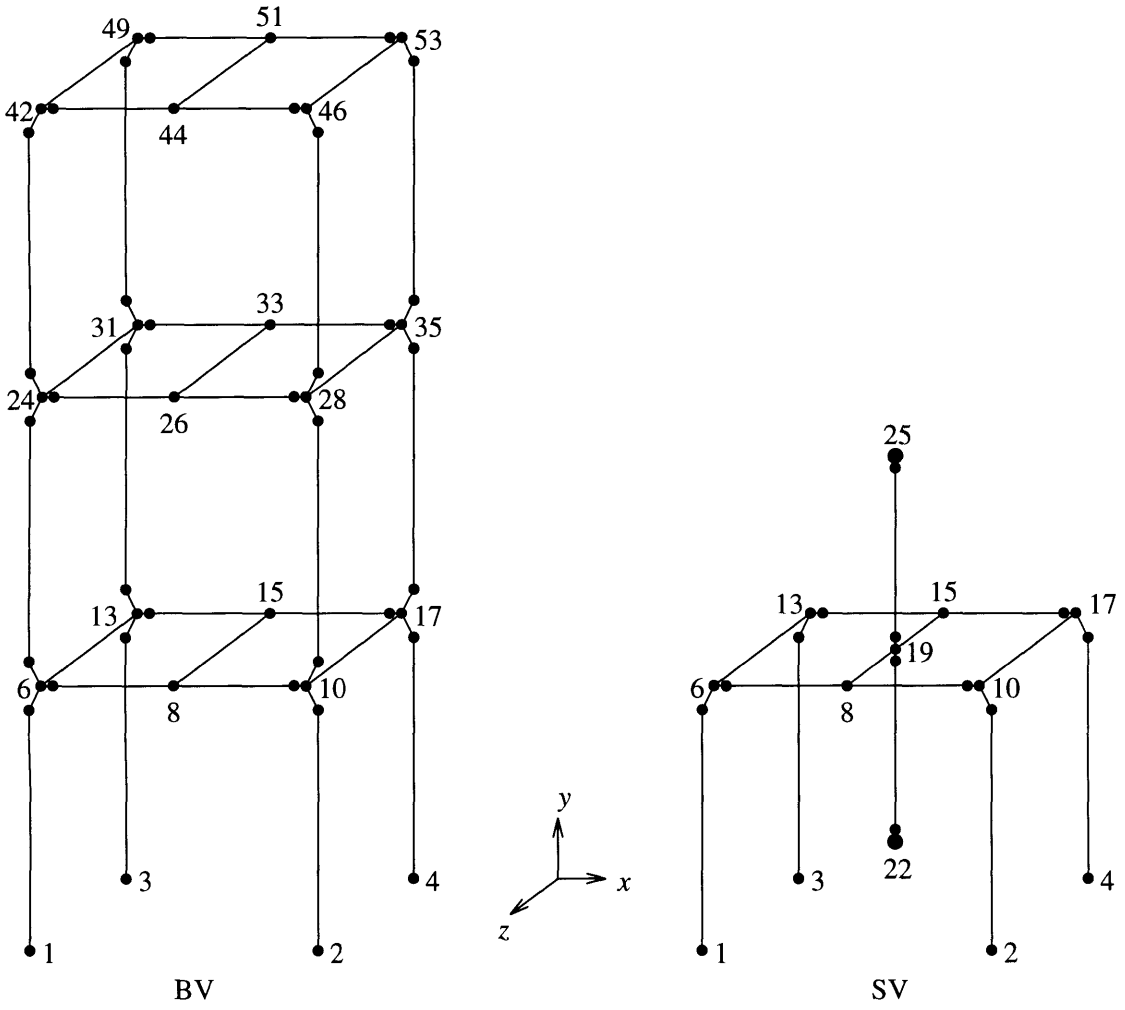

Figure 3.4: Finite element models. (Note: Only a selected number of grid points are shown, and of those, a few are labeled. For clarity, none of the elements are labeled. For each model, the origin of the coordinate system is at grid 3.)

fact was the basis for the conservative approach.

Even without generating and running the finite element models, the types of modes to expect can be easily predicted. Consider BV first, and imagine it as a cantilevered beam modeled by three lumped masses (corresponding to each floor). In general, each mass can have six DOF's, but restrict the motion to two translational DOF's perpendicular to the axial direction and one rotational DOF about the main axis. The other DOF's can be neglected at low frequencies. The translational DOF's lead to bending of the "beam", while the rotational DOF leads to torsion. Thus, there will be three distinct types of motion— two bending and one torsion. Since there are a total of three DOF's for each type, a maximum

of three modes are expected for each. This means that a total of nine modes are possible in all. The three modes for a given type are illustrated in Figure 3.5. Initially, all three floors move in phase, but for the higher modes, they become out of phase. Although the figure might seem applicable for only the bending cases, the phase relationships between floors are still valid for the torsion case. In this instance, the floors rotate with respect to one another.

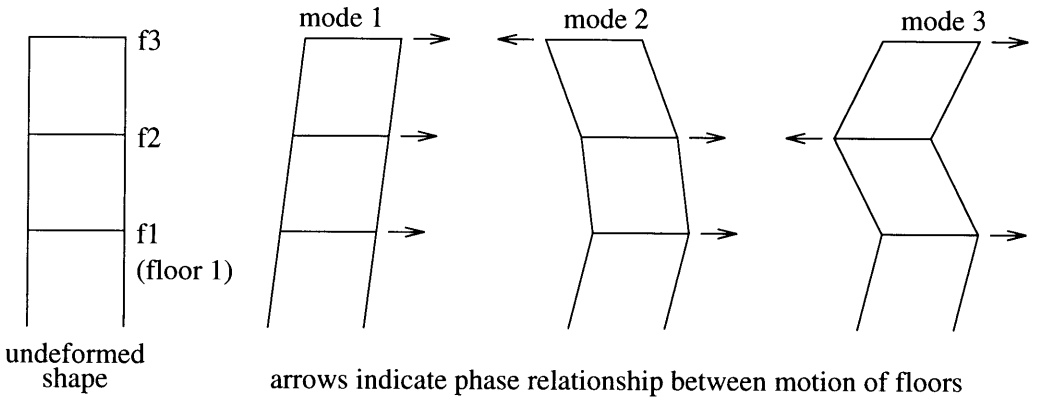

Figure 3.5: Three primary BV modes for a given type of motion.

These nine modes were all predicted by the initial BV model, and the results are given in Table 3.1. In the mode shape descriptions, the motion of each floor is given by either $\pm x$, $\pm z$, or $\pm ry$, where x and z indicate bending modes, and ry indicates a torsion mode (rotation about y). The plus or minus sign determines the phase relationship between the floors. The nine modes were the only ones that appeared below 100 Hz.

Table 3.1: Predicted Modes of Initial BV Finite Element Model Below 100 Hz

Mode #	Frequency (Hz)	Description
1	6.08	x-bending (f1,f2,f3:$+x$)
2	16.86	torsion (f1,f2,f3:$+ry$)
3	17.02	x-bending (f1,f2:$+x$,f3:$-x$)
4	23.08	z-bending (f1,f2,f3:$+z$)
5	24.61	x-bending (f1,f3:$+x$,f2:$-x$)
6	45.58	torsion (f1,f2:$+ry$,f3:$-ry$)
7	63.22	torsion (f1,f3:$+ry$,f2:$-ry$)
8	64.06	z-bending (f1,f2:$+z$,f3:$-z$)
9	91.91	z-bending (f1,f3:$+z$,f2:$-z$)

A similar process can be used to predict the modes of SV that will appear in the NASTRAN analysis. In this case, SV only has one floor, so three modes are expected (one for each type of motion). In addition, the antenna will have modes of its own. Since there are two tip masses, the modes should come in pairs; one mode where the masses move out of phase, and one where the masses move in phase. With this in mind, the three types of modes expected for the antenna will be doubled. As a result, a total of nine SV modes should be predicted (three floor modes and six antenna modes). Figure 3.6 shows the three modes for each type of motion, and Table 3.2 confirms this result.

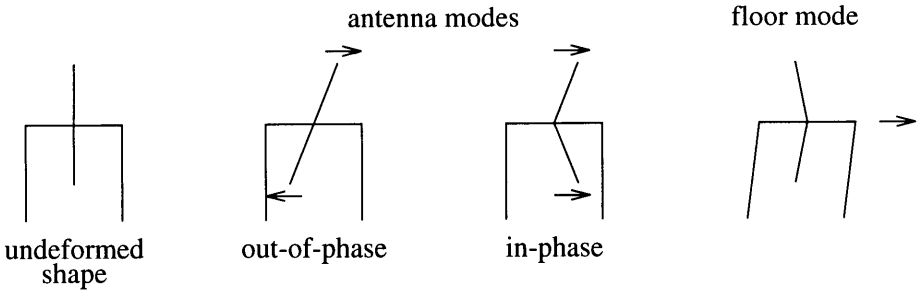

Figure 3.6: Three primary SV modes for a given type of motion.

Table 3.2: Predicted Modes of Initial SV Finite Element Model Below 100 Hz

Mode #	Frequency (Hz)	Description
1	7.08	antenna out-of-phase x-bending
2	7.23	antenna in-phase x-bending
3	17.78	x-bending (f1:+x)
4	27.03	antenna out-of-phase z-bending
5	29.11	antenna in-phase z-bending
6	42.92	torsion (f1:+ry)
7	48.57	antenna out-of-phase torsion
8	48.58	antenna in-phase torsion
9	69.94	z-bending (f1:+z)

It should be mentioned that the pure antenna torsion modes were very difficult to excite in the mode survey tests. The modes were heavily coupled with the antenna bending modes and other modes of the structure. As a result, the mode shapes were not extracted from the test results. An attempt was made, however, during the model update process to adjust the torsional spring constants at the connection between the tip mass beams and the cross

beam, as will be seen in Chapter 5. This at least enabled the predicted frequencies of these modes to better match the measured values. During the transient response tests, the frequencies of excitation were below these values, which allowed the antenna torsion modes to be of little importance during this phase.

Another item of great importance is how close the translational mass of the each model came to the total measured mass. There will be success criteria used in subsequent chapters that assume a highly accurate mass matrix. Thus, a check should be made to see if at least there is a small difference between the two values. Utilizing six rigid-body vectors, NASTRAN calculates a 6×6 mass matrix which contains the translational masses in the x, y, and z directions as well as mass moments of inertia. The three translational masses are identical, and the resulting value for each substructure is shown below along with the total measured mass. The high degree of correlation allows some confidence to be placed on the derived mass matrix.

Substructure	Measured mass (kg)	Model mass (kg)	% error
BV	44.68	44.56	−0.26
SV	10.07	10.09	−0.15

3.4 Model Reduction

Initial finite element models, such as the ones described previously, generally have more DOF's than are necessary for a dynamic analysis at low frequencies. A small subset of these DOF's is usually sufficient to predict all significant motion. In addition, measurements during testing are only provided at certain DOF's. As a result, there exists a need to reduce the models to a chosen set of DOF's. In NASTRAN, this is accomplished with the use of ASET1 cards. The DOF's listed in these cards become the "active" DOF's. Both the stiffness matrix and mass matrix are reduced to these DOF's, and one common method used to condense the matrices can be found in [10]. The resulting matrices are of order $n \times n$, where n is the number of active DOF's. If these matrices are then used in the typical eigenvalue problem to determine the mode shapes and frequencies, the resulting modes will be given in terms of the active set.

In the project, both substructure models were reduced to a set of DOF's that provided all the necessary information for the purposes of mode shape animation. These DOF's are the three translations for each of the nodes labeled in Figure 3.4, with the exception of

the base nodes. The modal animation program that was used is called NOMAD, and it is an Aerospace-developed tool for mode visualization. It reads in the coordinates of the nodes, the connectivity between the nodes, and the displacements of the nodes for each mode. The labeled nodes in Figure 3.4 were the only ones used for animation; thus, the analytical modes could be immediately plotted. The reduced model sizes were 54 DOF's for BV and 27 DOF's for SV. This represents a decrease in the original sizes by a factor of 6. It should be mentioned that the ASET's that were used depended on the type of model. For the purpose of model update, the just-described models were used. For the analytical coupling process, a different ASET was specified in order to meet certain requirements of the procedure.

As will be seen in the next chapter, the sensors in the mode survey tests did not correspond to the DOF's of the size 54 BV model or the size 27 SV model. Rigid-body assumptions enabled some of these DOF's to be related to others, which led to a further reduced DOF set (16 DOF's for BV; 12 for SV). What normally is done is to create a so-called Test-Analysis Model (TAM) whose active DOF set has a one-to-one correspondence with the DOF's measured by the sensors. However, this was not done in the project since the experimental mode shapes were expanded to the DOF's of the finite element models. Mode shape expansion techniques have been developed (e.g., see [24], [14]) that create a transformation matrix that relates either the measured or the analytical modes to the expanded modes. Instead of using such methods, this transformation matrix was derived from rigid-body assumptions. These relationships will be described in more detail in the next chapter. To show that in fact only minor differences are present between the two methods (TAM vs. expansion) for the structures in the project, the modes of BV were computed using the different ASET's. Table 3.3 shows how the natural frequencies compare, and it gives the elements on the diagonal of the cross-orthogonality matrix. This matrix is defined as $\phi_{54}^T M_{16} \phi_{16}$, where ϕ_{54} consists of the rows of the modal matrix from the 54 DOF model that correspond to the 16 DOF's of the other model. M_{16} is the mass matrix of the 16 DOF model, and ϕ_{16} is the the modal matrix. A diagonal term equal to one implies perfect correlation between the pair of modes (assuming proper normalization of the modes). As can be seen, all the modes are virtually identical, and the frequencies change slightly in a few of the modes. The larger differences in frequency occur at the higher frequencies, but these are out of the range of interest. A similar result holds for the SV case.

Table 3.3: Comparison of Modes of BV for 54 DOF Model and 16 DOF Model

Mode	Analytical frequencies (Hz)		Diagonal term
#	54 DOF model	16 DOF model	of cross-ortho
1	6.08	6.08	1.000000
2	16.86	16.86	0.999985
3	17.02	17.02	1.000000
4	23.08	23.14	1.000000
5	24.61	24.61	1.000000
6	45.58	45.59	0.999940
7	63.22	63.24	0.999978
8	64.06	65.40	0.999993
9	91.91	96.32	0.999988

3.5 Coupling Compatibility

The original finite element models did not take into account that they eventually would be coupled together. The coupling procedure discussed in Chapter 6 assumes that a common interface exists between the substructures. In Figure 3.4, the top four corner nodes of BV do not physically correspond to the four base nodes of SV when BV and SV are coupled. They are, in fact, offset slightly in space. For the purposes of model update, this did not play a role since the updates occurred independently. Testing had been performed on the separate substructures, and the results did not depend on the existence of the other substructure. In order to allow compatibility during the coupling process, however, the finite element model of BV was modified by the addition of four nodes at the top level that would be collocated with the four SV base nodes. The manner in which the added nodes and elements are defined are consistent with the modeling of joints described in Section 3.2. The DOF's of BV and SV could then be separated into sets of interface and non-interface DOF's. To avoid unnecessary repetition, only the updated models used by the coupling program are included in Appendix A. Comments are provided that explain the changes made to the original models.

Chapter 4

Mode Survey Tests

Once the two substructures had been assembled, the mode survey tests were able to commence. The purpose of these tests was to experimentally identify the mode shapes, natural frequencies, and damping ratios associated with all the substructure modes below 60 Hz. The results could then be used to adjust the finite element models before the coupling of the models proceeded. A mode survey test of the physically coupled system would then allow the accuracy of the coupling method to be checked. This chapter discusses the specific type of mode survey test that was employed and describes the hardware and software used to perform the testing. The actual configuration during testing is then presented, followed by a summary of how the modes were extracted from the gathered data. The resulting modes are then given for BV (with and without added damping), for SV, and finally for the coupled structure BVSV (for both damping cases). Checks are done on these modes to ensure that they were extracted properly, and any slight inconsistencies are then corrected.

4.1 Procedure

In general, modal testing involves subjecting a structure to one or more applied forces and measuring the response at several locations. There are two distinct approaches that are commonly used when mode survey tests are conducted. The first, known as the multi-point sine-dwell method, has been a standard for several decades. It involves distributing a number of shakers (actuators) at various locations, and exciting the test article at a single frequency. The principal objective is to have the shakers positioned and their forces appropriated so as to isolate a specific mode. The natural frequency and mode shape can

be measured directly without the need for complicated data processing and analysis. This procedure is then repeated for other target modes. Some drawbacks are that the method can be very time-consuming and that the force appropriation problem can be quite difficult to solve.

The second modal testing method is characterized by the use of frequency response functions (i.e., transfer functions). It has seen increasing popularity since the advent of high-speed data acquisition systems. A single shaker applies a random force with a sufficient frequency content to excite all the modes of interest simultaneously. The measured force and responses are sampled and processed into frequency response functions (FRF's). The modal parameters such as natural frequencies, mode shapes, and damping ratios are then extracted from the FRF's through a process of curve-fitting. This method is more automated than the sine-dwell method and, consequently, can yield the structure's modes in a significantly shorter amount of time. For more complicated structures, several shakers can be used to apply independent, randomly-varying forces and provide a better energy input distribution.

The two methods both have their advantages and disadvantages, and they can at times produce different results. (See [5], which compares the results of various methods used on the Galileo spacecraft.) It was decided to employ the single-point random method during the project for a variety of reasons. The availability of only a single shaker amplifier limited the number of actuators to one. The presence in the Dynamics and Control Laboratory of a dedicated front-end and a workstation with modal testing and analysis software favored the FRF approach. Once the shaker was in place, a test could be conducted, data acquired, and an analysis performed relatively quickly. This was important considering that five separate mode survey tests were required in the project (2 for BV, 1 for SV, and 2 for BVSV).

Having selected the single-point random method, the next steps were to identify DOF's to measure during testing and to choose the location of the shaker. As was shown in the last chapter, the modes predicted by the finite element models for both substructures consist of only three types—bending in two orthogonal directions, and torsion about the vertical axis. Due to the simplified nature of the substructures, no coupling of these types of motion appeared in the modes. The three types occurred independently of one another. As a result, instead of orienting the shaker so as to excite the structures along all three axes, it was restricted to cause excitation in only the horizontal (xz) plane. This would be sufficient to cause the bending and torsion modes to occur. In order to try and obtain the best

modes possible, two different tests were performed for each configuration. In one instance, the shaker was oriented in the x direction. Only the x-bending and torsion modes were extracted from the data collected in these series of tests. For the other case, the shaker was oriented in the z direction, and only z-bending modes were extracted from the collected data. The two sets of modes were then combined, and checks were made on this new set. In all cases, the shaker was driven by a random signal with frequency content of 0–60 Hz.

Although no modes were anticipated in the vertical (y) direction, sensors were still used to provide axial measurements. Instead of assuming that all DOF's in the y direction had zero response, the limited number of sensors set aside for these measurements allowed the true level of response to be approximated. The primary sensors were those measuring in the x and z directions, and their locations will be shown in Section 4.3.

4.2 Experimental Hardware and Software

The main components of a particular mode survey test were

- the test article under consideration and its support
- an actuator to excite the structure
- a power amplifier for the actuator
- sensors to provide measurements
- signal-conditioning amplifiers for the sensors
- a front-end consisting of
  - D/A converter to produce an analog source signal
  - A/D converters (with filters) for digital sampling of the measurements
- a workstation running software for data processing, storage, and analysis

The flow diagram in Figure 4.1 shows how all the components work collectively. The actuator consisted of an MB Dynamics electrodynamic shaker which could produce a force on the order of 30 lbs (although this much force was never needed during the course of the project). This type of shaker converts a supplied input signal to an alternating magnetic

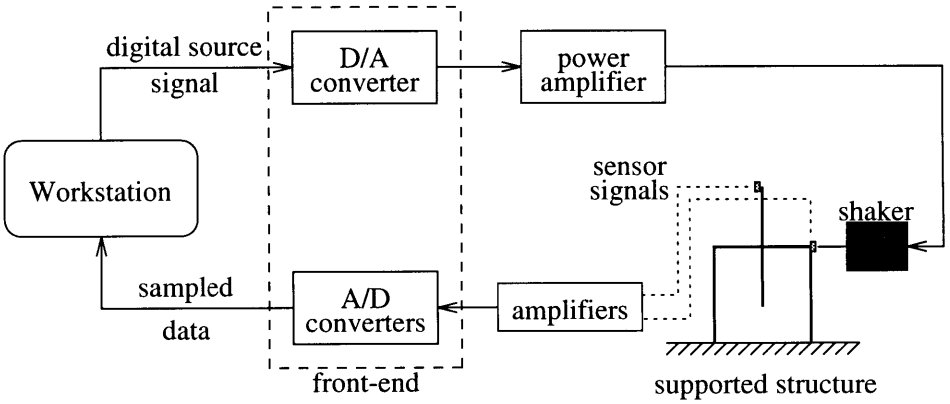

Figure 4.1: Flow diagram showing main components used during mode survey testing.

field. A coil placed within the field is joined to the main drive shaft. Thus, varying the magnetic field will result in a certain amplitude and frequency of shaft motion. A knob on the shaker amplifier allows this amplitude to be adjusted as desired. For a given signal that enters the amplifier, the amount of force applied to the shaker can be increased or decreased by the appropriate knob setting. The knob can be turned in fixed increments, thereby allowing consistency among tests. The linearity of the test articles was checked by performing multiple tests at different force levels and seeing how the FRF's were changed. Ideally, for a linear structure, there should be no difference in the various FRF's.

The actual connection to the structure was made via a number of other parts, the most important of which was the stinger. A stinger can be a very thin rod (or on the other hand, a thick wire). A welding rod was used in the tests, and it had a diameter between 1 and 2 mm. It was attached to the shaker on one end and to an adapter on the other end. A Kistler force transducer (Model 9712A50) was placed between the adapter and a small block of aluminum that was glued to the desired place on the structure. The force transducer had a sensitivity of about 100 mV/lbf, and it was used to provide a measurement of the applied force. This was important since transfer functions from the force input to the responses were desired. The various parts are shown in detail in Figure 4.2.

The amount of exposed stinger length proved to be an important consideration. When some of the first trial tests were conducted, several unexplained modes appeared in the transfer functions. It was soon discovered that the stinger was too short and that it was actually introducing quite a bit of lateral stiffness loading to the structure. This inadvertently modified the structure and resulted in the altered modes. By changing the length to

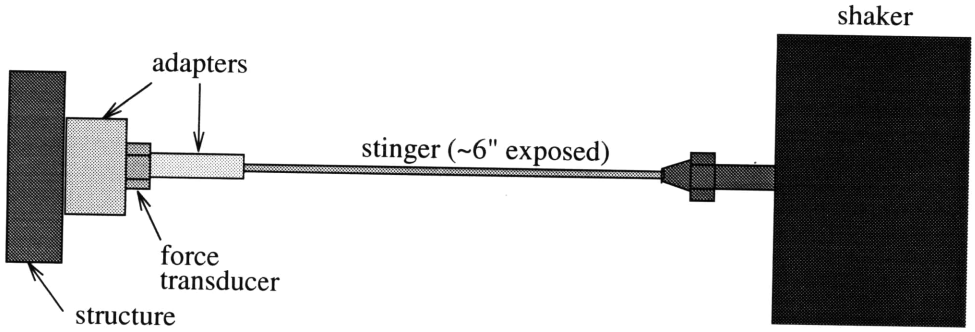

Figure 4.2: Attachment of shaker to structure.

about 6″, this coupling was greatly diminished. The shaker itself was suspended from an overhead support, and a large spring helped to isolate the shaker from outside disturbances.

The remaining sensors consisted of Kistler accelerometers (Model 8630A50) with sensitivities close to $100\,\mathrm{mV}/g$ and an acceleration range of $\pm 50\,g$. They had a single sensing axis which was perpendicular to the surface to which they were mounted. Each accelerometer was attached to the structure by means of a strong, instant glue. This enabled them to remain attached even at the higher frequencies. The accelerometers that were used had been calibrated prior to other tests, and so the same calibration values were kept. Before reaching the A/D converters of the front-end, the accelerometer signals were sent to signal-conditioning amplifiers in order to improve the signal-to-noise ratio. Either a gain of 1 or 10 could be specified at each amplifier, depending on the strength of the signal.

The wires from the accelerometers to the amplifiers were carefully run along and taped to the beams of the structure. This kept the wires from moving back and forth and colliding with each other and the structure, which could have caused unwanted damping. This phenomena was originally observed as a large increase in damping for the antenna modes. The damping was reduced significantly by running the wires for the tip mass accelerometers along the cross beam and then either up or down to the appropriate tip mass. Before this was done, the wires had been allowed to hang limply and have the tip masses support their weight.

At the heart of the data acquisition hardware was a DIFA SCADAS front-end consisting of up to four D/A converters (called QDAC) and a maximum of 30 channels of A/D converters. Each channel also possessed filters that could provide low-pass or band-pass filtering. Controlling this front-end was an HP9000 workstation that met all of the data

processing, storage, and analysis needs. The LMS CADA-X software [20] on the HP was the main tool for both modal testing and analysis. Within it, the test configuration could be defined and all the necessary test parameters specified.

For each substructure, as well as for the coupled system, a simplified geometrical description of each was stored in appropriate geometry files. The files consisted of nodes, their coordinates, and the connectivity between nodes. After mode shapes had been extracted from the measured data, the geometry model could be shown on the screen and animated to provide a first indication of the experimental modes shapes. The DOF's at which the force transducer and the accelerometers were located could be defined with respect to these nodes and in directions corresponding to a local coordinate system. In all cases, the nodal coordinate systems were consistent with the global system that was used for the finite element models. For each test, all of the sensors had to be identified with a channel of the front-end. This identification consisted of specifying some type of label for each sensor, the dimension of the quantity that was being measured (e.g., force, acceleration), the units (e.g., lbf, g), and finally a calibration value. In addition, each channel was associated with a specific DOF of the geometry model. This relationship was given in terms of the node number and the direction (e.g., $+x$).

Some of the most important test parameters that could be specified and that were used in all of the mode survey tests are given in Table 4.1. The source signal that was created to

Table 4.1: Commonly Used Test Parameters

Parameter	Value	Parameter	Value
Source signal	noise (0–60 Hz)	Channel amplification	autoranging
Overload mode	flag	Overload retry	3
Data center frequency	30 Hz	Bandwidth	60 Hz
Number of spectral lines	2048	Filter cutoff	60 Hz
Averaging type	stable	Number of averages	20
Averaging overlap	50%	Window type	Hanning
Measurement function	FRF	Estimator	H1

drive the shaker consisted of band-limited white noise with a frequency content of 0–60 Hz. The autoranging feature allowed samples to be taken before the actual test began, and then the gains on all the channels were adjusted so as to maximize the number of bits used in the A/D converters. In the case of an overload, data would be retaken at most three

more times, and a warning flag would appear. The frequency range of interest was below 60 Hz, and this was specified by choosing a bandwidth of 60 Hz centered about 30 Hz. The filter cutoff frequency could only be given as a certain percentage of this bandwidth, so a value of 100% was selected. The number of spectral lines within the bandwidth was set at 2048. The CADA-X software automatically set the blocksize to be twice this number, which implied a total of 4096 points would be taken per acquisition. The sampling rate was also automatically set at about twice the highest frequency of interest. This resulted in an acquisition duration of 34.13 s, and a frequency resolution of $\frac{1}{34.13\,\mathrm{s}} \approx 0.03\,\mathrm{Hz}$. A stable averaging type was used, and 20 averages were taken using a 50% overlap. To minimize the effects of leakage, a Hanning window was applied to the measured data. The FRF's were computed using the H1 estimator.

Once everything had been defined properly, the test was able to begin. The system was armed, and then data was collected once the shaker was activated. After each average, the updated FRF's of selected DOF's were plotted on the screen. When the data acquisition session was over, a visual inspection of all the computed FRF's and coherences was made. A clearly bad coherence indicated a faulty sensor, and the test was rerun after the problem had been corrected. All the coherences had values close to zero for frequencies below about 2 Hz, and this was a result of the accelerometers not giving consistent readings at such low frequencies. Because of the low levels of response in the vertical direction, the coherences corresponding to accelerometers in this direction were not as good as others. When the FRF's were considered acceptable, they were saved in the project database for subsequent use in the analysis phase.

4.3 Sensor and Actuator Placement

The choice of accelerometer and shaker locations was based on a combination of intuition and knowledge of the expected modes of the structures. As discussed previously, it was decided to have the shaker excite only in the horizontal plane and to move the shaker between two different directions in order to obtain specific sets of modes. Placing the shaker at the top level of each structure would require the least amount of shaker force since the lever arm with respect to the base would be the largest. Also, the top floor was not a node in the bending modes, which meant that these modes could be excited. To best

excite the torsion modes, the force should be applied at one of the corners of the floor. For most of the tests, the shaker was placed so as to excite at a corner and either in the x or z direction. However, during the tests on BV, it was noticed that some of the z-bending modes had some slight torsional motion. The shaker was moved from the corner to the center of the beam (as shown in Figure 4.3) to see if the coupling continued. Figure 4.3 shows the CADA-X geometry models that were defined for the tests. They were meant for visualization purposes, and the nodes are a subset of the grid points in the finite element models. The model for the coupled structure, BVSV, was just a combination of these two.

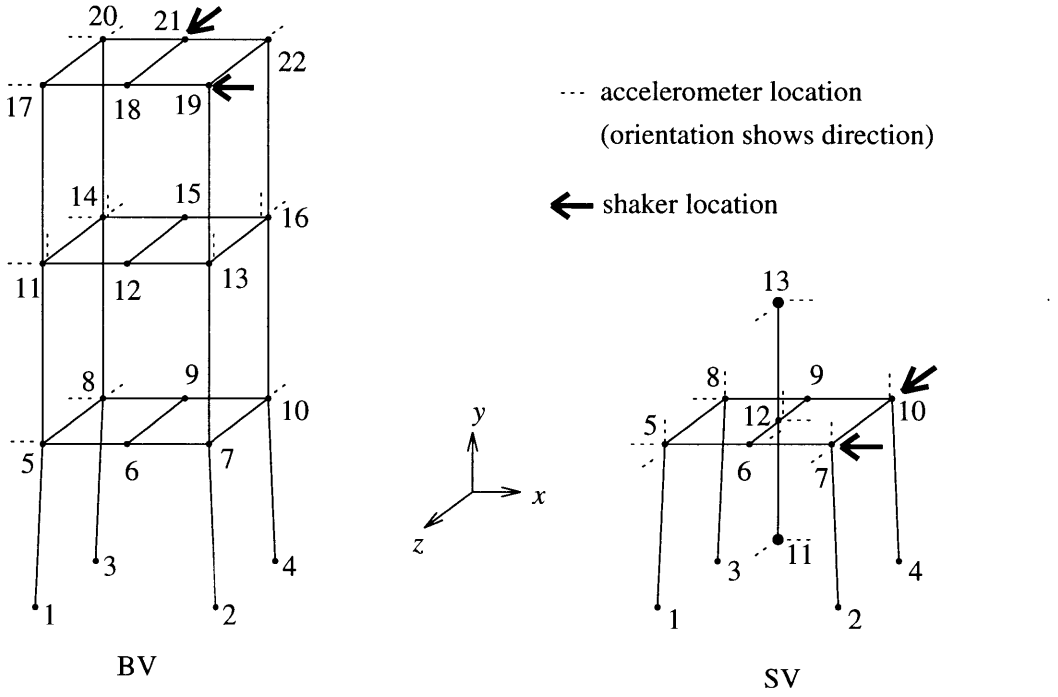

Figure 4.3: Experimental geometry models showing accelerometer and shaker locations.

The placement of the accelerometers was determined primarily by rigid-body considerations. Figure 4.4 indicates the only DOF's that need to be measured at each floor if the floor is assumed to behave as a rigid body in a plane. Thus, only four accelerometers were needed per floor for measurements of xz motion. (The same result can be concluded from the absence of local modes of the floor beams in the analytical predictions.) Each tip mass required two accelerometers, and a total of three were placed at the center of the cross beam supporting the antenna assembly. As mentioned previously, motion in the y direction was not as great as the other two directions, but accelerometers were set up to provide these

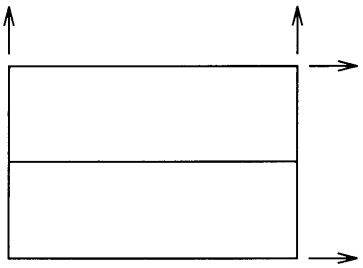

Figure 4.4: Independent DOF's assuming rigid-body, planar motion of floor.

measurements for the sake of completeness.

The following tables summarize the locations of sensors and the placement of the shakers for the different mode survey tests. The DOF specified for each shaker location corresponds to the DOF at which the force transducer was placed. The test model DOF's correspond to the labeling in Figure 4.3, while the FEM DOF's correspond to the labeling in Figure 3.4. The notation "SV:5:$-x$", for instance, refers to the DOF in the $-x$ direction at node 5 of substructure SV. Table 4.2 is applicable to the tests on SV, Table 4.3 to the tests on BV, and Table 4.4 to the tests on BVSV.

Table 4.2: Sensor and Actuator Placement for SV Testing

Accel. #	DOF (test model)	DOF (FEM)	Accel. #	DOF (test model)	DOF (FEM)
1	SV:5:$-x$	SV:6:$-x$	2	SV:5:$+y$	SV:6:$+y$
3	SV:5:$+z$	SV:6:$+z$	4	SV:7:$+z$	SV:10:$+z$
5	SV:8:$-x$	SV:13:$-x$	6	SV:11:$+x$	SV:22:$-x$
7	SV:11:$+z$	SV:22:$+z$	8	SV:12:$+x$	SV:19:$+x$
9	SV:12:$+y$	SV:19:$+y$	10	SV:12:$+z$	SV:19:$+z$
11	SV:13:$+x$	SV:25:$+x$	12	SV:13:$+z$	SV:25:$+z$
Shaker location #	DOF (test model)	DOF (FEM)	Shaker location #	DOF (test model)	DOF (FEM)
1	SV:7:$-x$	SV:10:$-x$	2	SV:10:$+z$	SV:17:$+z$

4.4 Mode Extraction Method

Once the FRF's had been computed for a given test, the experimental modal analysis phase could begin. This involved modal parameter estimation techniques that adjusted the

Table 4.3: Sensor and Actuator Placement for BV Testing

Accel. #	DOF (test model)	DOF (FEM)	Accel. #	DOF (test model)	DOF (FEM)
1	BV:5:$-x$	BV:6:$-x$	2	BV:8:$-x$	BV:13:$-x$
3	BV:8:$-z$	BV:13:$-z$	4	BV:10:$-z$	BV:17:$-z$
5	BV:11:$-x$	BV:24:$-x$	6	BV:11:$+y$	BV:24:$+y$
7	BV:13:$+y$	BV:28:$+y$	8	BV:14:$-x$	BV:31:$-x$
9	BV:14:$+y$	BV:31:$+y$	10	BV:14:$-z$	BV:31:$-z$
11	BV:16:$+y$	BV:35:$+y$	12	BV:16:$-z$	BV:35:$-z$
13	BV:17:$-x$	BV:42:$-x$	14	BV:20:$-x$	BV:49:$-x$
15	BV:20:$-z$	BV:49:$-z$	16	BV:22:$-z$	BV:53:$-z$
Shaker location #	DOF (test model)	DOF (FEM)	Shaker location #	DOF (test model)	DOF (FEM)
1	BV:19:$-x$	BV:46:$-x$	2	BV:21:$+z$	BV:51:$+z$

Table 4.4: Sensor and Actuator Placement for BVSV Testing

Accel. #	DOF (test model)	DOF (FEM)	Accel. #	DOF (test model)	DOF (FEM)
1	BV:5:$-x$	BV:6:$-x$	2	BV:8:$-x$	BV:13:$-x$
3	BV:8:$-z$	BV:13:$-z$	4	BV:10:$-z$	BV:17:$-z$
5	BV:11:$-x$	BV:24:$-x$	6	BV:11:$+y$	BV:24:$+y$
7	BV:13:$+y$	BV:28:$+y$	8	BV:14:$-x$	BV:31:$-x$
9	BV:14:$+y$	BV:31:$+y$	10	BV:14:$-z$	BV:31:$-z$
11	BV:16:$+y$	BV:35:$+y$	12	BV:16:$-z$	BV:35:$-z$
13	BV:17:$-x$	BV:42:$-x$	14	BV:20:$-x$	BV:49:$-x$
15	BV:20:$-z$	BV:49:$-z$	16	BV:22:$-z$	BV:53:$-z$
17	SV:5:$-x$	SV:6:$-x$	18	SV:5:$+y$	SV:6:$+y$
19	SV:5:$+z$	SV:6:$+z$	20	SV:7:$+z$	SV:10:$+z$
21	SV:8:$-x$	SV:13:$-x$	22	SV:11:$+x$	SV:22:$-x$
23	SV:11:$+z$	SV:22:$+z$	24	SV:12:$+x$	SV:19:$+x$
25	SV:12:$+y$	SV:19:$+y$	26	SV:12:$+z$	SV:19:$+z$
27	SV:13:$+x$	SV:25:$+x$	28	SV:13:$+z$	SV:25:$+z$
29	SV:7:$+y$	SV:10:$+y$	30	SV:8:$+y$	SV:14:$+z$
31	SV:10:$+y$	SV:17:$+y$			
Shaker location #	DOF (test model)	DOF (FEM)	Shaker location #	DOF (test model)	DOF (FEM)
1	SV:7:$-x$	SV:10:$-x$	2	SV:10:$+z$	SV:17:$+z$

parameters of a model to better match the measured data. The method that was available in the LMS CADA-X software and that seemed most appropriate to use is known as the Least Squares Complex Exponential (LSCE) method. In the frequency domain, the transfer function matrix $H(s)$ relating displacement to force input can be expressed as

$$H(s) = \sum_{j=1}^{N} \left[\frac{R_j}{s - \lambda_j} + \frac{R_j^*}{s - \lambda_j^*} \right] \tag{4.1}$$

where N is the number of modes, R is the residue matrix, $s = i\omega$, and $\lambda = -\zeta\omega_n + i\omega_n\sqrt{1-\zeta^2}$. (The notation $(\,)^*$ indicates a complex conjugate.) Taking the inverse Fourier Transform of Equation 4.1 yields the corresponding impulse response function (IRF) matrix $h(t)$ in the time domain, which can be written as

$$h(t) = \sum_{j=1}^{N} \left[R_j e^{\lambda_k t} + R_j^* e^{\lambda_k^* t} \right] \tag{4.2}$$

The LSCE method works on measured data in the time domain rather than in the frequency domain, and as a result, Equation 4.2 is used as the parametric model. Inspection of this equation reveals that the pole values λ_k do not depend on any particular input or output DOF. The poles are global characteristics of the structure and should theoretically be the same for all FRF's. The LSCE method takes advantage of this fact by using all the measured data simultaneously to estimate these global parameters. It begins with an initial assumption on the number of modes and then solves for the λ_k in a least-squares sense using an equation that is not a function of the residues. The method actually uses a discrete form of Equation 4.2 due to the sampled nature of the data.

CADA-X permits the user to select a frequency band for the analysis of a chosen set of measured FRF's. It then creates what is known as a stabilization diagram. A single mode is assumed to exist in the analysis band, and the estimates of pole frequency and damping are computed. This is repeated for an increasing number of assumed modes in the model, and the calculated frequencies and damping are compared to those of previous models. The stabilization diagram shows how the poles evolve when the number of modes is increased. It is expected that poles corresponding to the true modes of the structure should not change significantly for models larger than the correct size model; however, due to imperfections present in the data, additional poles will be present. These so-called computational poles

will appear in different locations for different size models. They will also usually have very high damping ratios associated with them. The stabilization diagram clearly shows poles that remain stable, and it is these poles that can be selected for the remaining analysis. It should be noted that an option is given to include residual terms that account for modes outside of the analysis band. This is important since modes out of the bandwidth still have an effect on the FRF's.

Once the poles have been selected, the LSCE frequency domain method is employed to solve for the residues. This time, Equation 4.1 is used with the addition of upper and lower residual terms. The residues are local characteristics and depend on the particular input and output DOF's. They appear linearly in Equation 4.1 and can be solved for directly. These residues are generally complex, containing both magnitude and phase information. Each residue can be expressed as the product of two mode shape coefficients and a scaling factor. Thus, the mode shapes can be obtained once the residues are known. In order for a direct comparison to be made with the real, normal modes of the finite element models, it was desired to convert the measured complex modes into real modes. The technique used by CADA-X is known as amplitude normalization. This involves taking the magnitude of each component of the complex mode shape and then adjusting the sign to better match the phase relationships. This approach is only correct for systems with proportional damping. It can yield a poor approximation for systems with significant effects of non-proportional damping, as discussed in [18]. For the structures in the project, the complexity of the modes was slight, even for the cases of added damping. Thus, this method did produce reasonable approximations for modes of the hypothetical undamped structures. As an illustration, the scatter plot of the 16 calculated complex mode shape coefficients for the BV mode with the highest damping is shown in Figure 4.5. As can be seen, all the points lie almost entirely on the real axis. The amplitude normalization procedure forces them to be on this axis (i.e, forces real modes). Even in this case, such an approximation is a good one. After the real modes were obtained, they could then be used in mode checks and compared with the analytical modes during the the updates of the finite element models.

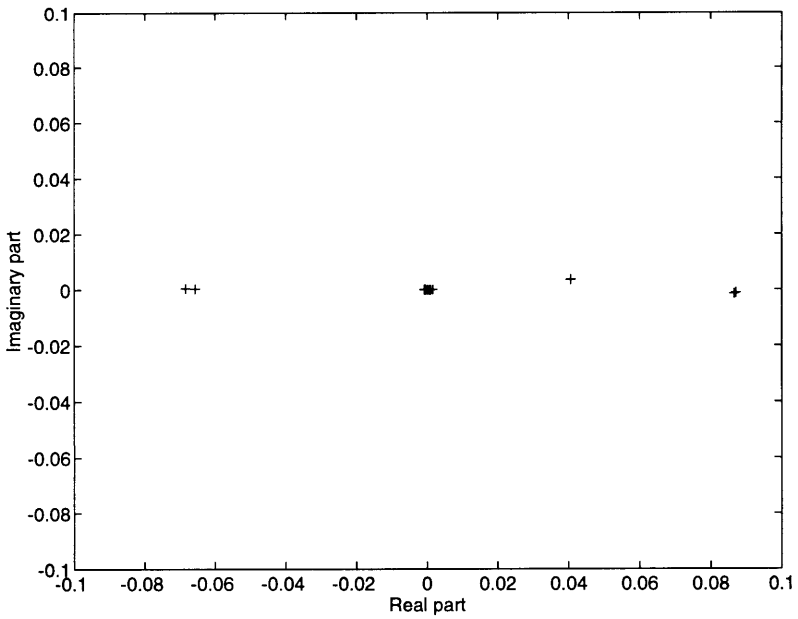

Figure 4.5: Scatter plot of measured complex BV mode.

4.5 Results

Before the measured modes obtained in the different tests are presented, it is important to confirm that the structures can indeed be considered linear under normal testing conditions. One way in which linearity can be checked is to change the force level between two tests and then compare their FRF's. If the response depends linearly on the input, then the FRF (ratio of output to input) should remain the same for both cases. Figure 4.6 shows the measured FRF's for two tests on BV in which the setting on the shaker amplifier was increased by 20% from one test to another. The two curves seem to coincide perfectly, which suggests linear behavior about this operating point. Similar results hold for substructure SV and the coupled system.

4.5.1 Substructure BV

The FRF's shown in Figure 4.6 are driving point FRF's of substructure BV without added damping. A driving point FRF is obtained when the response is collocated with the applied force. It is characterized by an alternating pole-zero pattern (alternating peaks and valleys) in the magnitude plot. Each peak corresponds to a mode, and a total of seven are visible in the figure. These modes are summarized in Table 4.5.

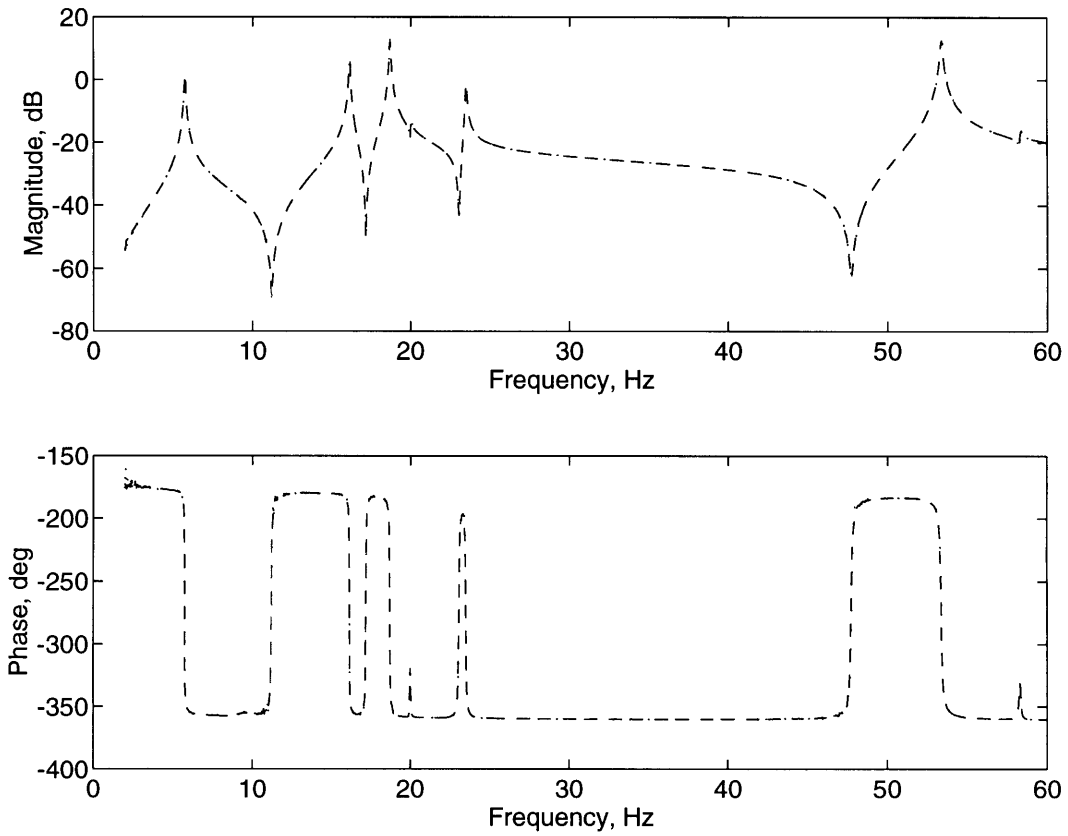

Figure 4.6: Measured driving point FRF's for two tests ($\cdots$, $--$) having a 20% difference in shaker force amplification.

Table 4.5: Measured Modes of BV Without Added Damping

Mode #	Frequency (Hz)	Damping (%)	Description
1	5.72	0.41	x-bending (f1,f2,f3:+x)
2	16.14	0.16	x-bending (f1,f2:+x,f3:−x)
3	18.68	0.17	torsion (f1,f2,f3:+ry)
4	19.98	0.14	z-bending (f1,f2,f3:+z)
5	23.46	0.16	x-bending (f1,f3:+x,f2:−x)
6	53.33	0.14	torsion (f1,f2:+ry,f3:−ry)
7	58.29	0.11	z-bending (f1,f2:+z,f3:−z)

A few observations can be made when these results are compared to the analytical modes given in Table 3.1. One of the first is that the order of the modes has changed. The two analytical torsion modes have swapped places with the next highest bending modes. Also, all of the measured bending mode frequencies are lower than the analytical predictions. This is a consequence of using rigid joints in the model. The model, therefore, is too stiff, which leads to an overprediction of the bending frequencies. The predicted torsion modes, on the other hand, have frequencies that are lower than the measured values. This can be explained by the fact that a lumped mass approach was used. It will be shown in the next chapter that computing a consistent mass matrix instead will cause the analytical torsional frequencies to increase significantly, with only a minor effect on the bending mode frequencies.

To have some degree of confidence in the values extracted for the frequencies and damping ratios, the variation of these values needed to be observed from test to test. The usual way this was done in the project was to obtain the values for one test. Then another test was performed with a small change in the shaker amplification setting, but with everything else remaining the same. The parameters extracted from this new test were then checked for consistency with the old values. If the frequencies and damping ratios had only slight variations, then one of the sets of results was kept for further use. Otherwise, more tests were conducted to provide clarification. As an example, the parameters that were obtained for BV in other tests are given below. They compare rather well with the values given in Table 4.5. For the other mode survey tests, such examples will not be given, but it should be stressed that consistency was verified in all cases.

Mode #	1	2	3	4	5	6	7
Freq. (Hz)	5.73	16.15	18.69	19.98	23.47	53.35	58.30
Damping (%)	0.39	0.15	0.16	0.13	0.15	0.13	0.12

When the damping treatment was added to BV, the damping ratios of the modes did increase as expected. In addition, the damping had the greatest effect on the x-bending modes. In Figure 4.7, the driving point FRF's for both cases are superimposed. The three peaks corresponding to the x-bending modes are noticeably smaller, with the decrease in the second one being the most pronounced. This agrees with the results reflected in Table 4.6.

The coupling procedure presented in Chapter 6 uses what are known as interface-loaded modes. These modes are obtained by collapsing the mass and stiffness properties of one

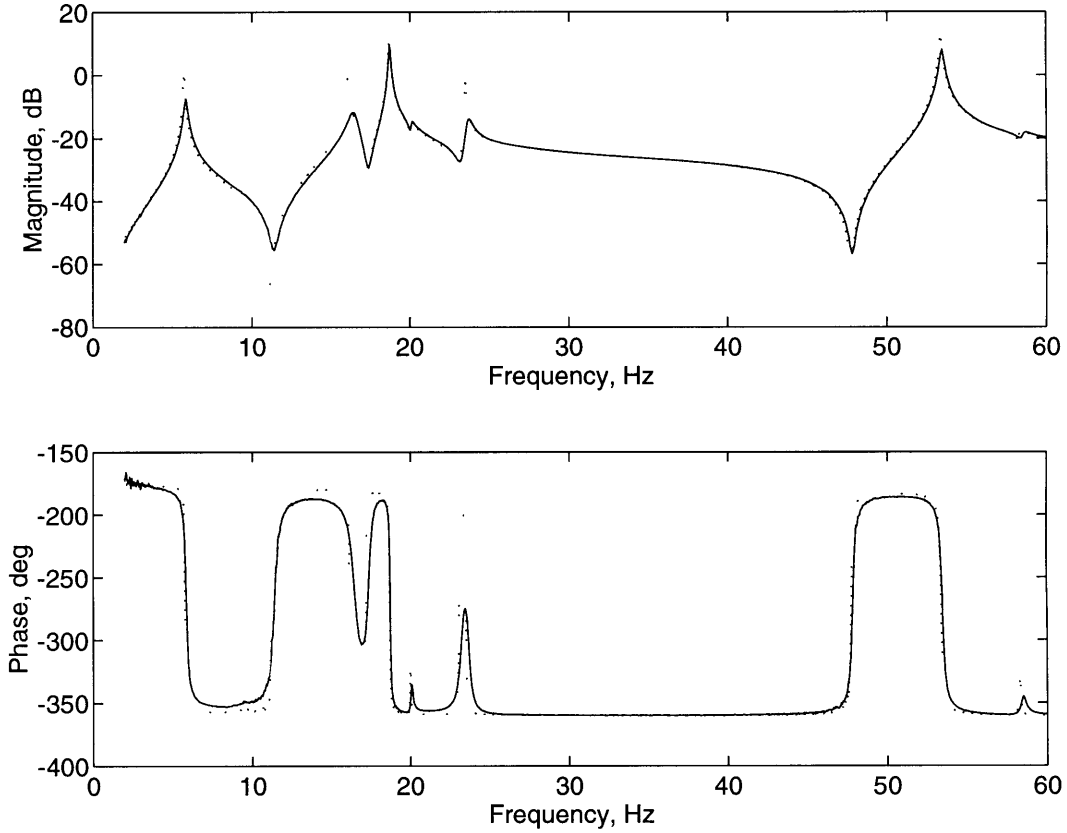

Figure 4.7: Measured driving point FRF's for BV with (—) and without (···) added damping.

Table 4.6: Measured Modes of BV With Added Damping

Mode #	Frequency (Hz)	Damping (%)	Description
1	5.83	1.80	x-bending (f1,f2,f3:+x)
2	16.46	1.93	x-bending (f1,f2:+x,f3:−x)
3	18.71	0.26	torsion (f1,f2,f3:+ry)
4	20.06	0.42	z-bending (f1,f2,f3:+z)
5	23.62	0.88	x-bending (f1,f3:+x,f2:−x)
6	53.42	0.24	torsion (f1,f2:+ry,f3:−ry)
7	58.47	0.35	z-bending (f1,f2:+z,f3:−z)

substructure onto the interface coordinates of the other and then computing the modes of the modified substructure. This leads to better convergence to the system modes. As will be seen, substructure BV will undergo the analytical interface loading. This implies that the damping ratios for BV used in predicting the damping of the coupled system must correspond to the interface-loaded modes. The damping ratios shown in Tables 4.5 and 4.6, however, do not include the effects of any type of loading. To account for this, additional tests were performed that attempted to introduce some degree of mass loading. It was assumed that the stiffness loading was negligible and that a way to approximate the mass loading would be sufficient. This was achieved by using a variety of spare parts that had a total mass within 0.15% of SV's measured mass. This extra material was either rigidly attached or taped to the top floor of BV. A series of tests were then performed, with the goal being only to extract the new damping ratios. The mode shapes and frequencies were not vital since they would be analytically computed using the updated FEM's. As would be expected, the original BV modes did change somewhat, but not enough to cause modes to swap places. The damping ratios for the series of tests were averaged, and the results (in %) for both damping cases are as follows.

Mode #	1	2	3	4	5	6	7
No added damping	0.47	0.16	0.17	0.11	0.16	0.14	0.10
Added damping	1.55	1.98	0.31	0.35	1.11	0.23	0.40

When compared with the levels of damping without mass loading, the results for the first case do not differ appreciably. In fact, it would be hard to justify that the changes were due to the mass loading instead of variations from test to test. The results for the second case, however, do reveal some significant differences that can be attributed to the mass loading. It is these values of modal damping shown above that were used in the damping formulations of Chapter 7.

4.5.2 Substructure SV

Substructure SV, despite its smaller size, was quite difficult to test because of the local antenna modes. The antenna modes came in pairs, with the tip masses moving in phase in one mode and out of phase in the other. The motion of the rest of the structure for the out-of-phase modes was much smaller than for the in-phase modes, and as a result, the out-of-phase modes were difficult to excite cleanly from an applied force at the first

floor. Figure 4.8 has two measured FRF's plotted. One is the driving point FRF, and the other is an FRF corresponding to a DOF of one of the tip masses. (In both instances, the applied force is in the x direction.) The two low-frequency, closely-spaced antenna modes are clearly visible in the tip mass FRF, while the two torsion antenna modes around 39 Hz appear only as a single peak.

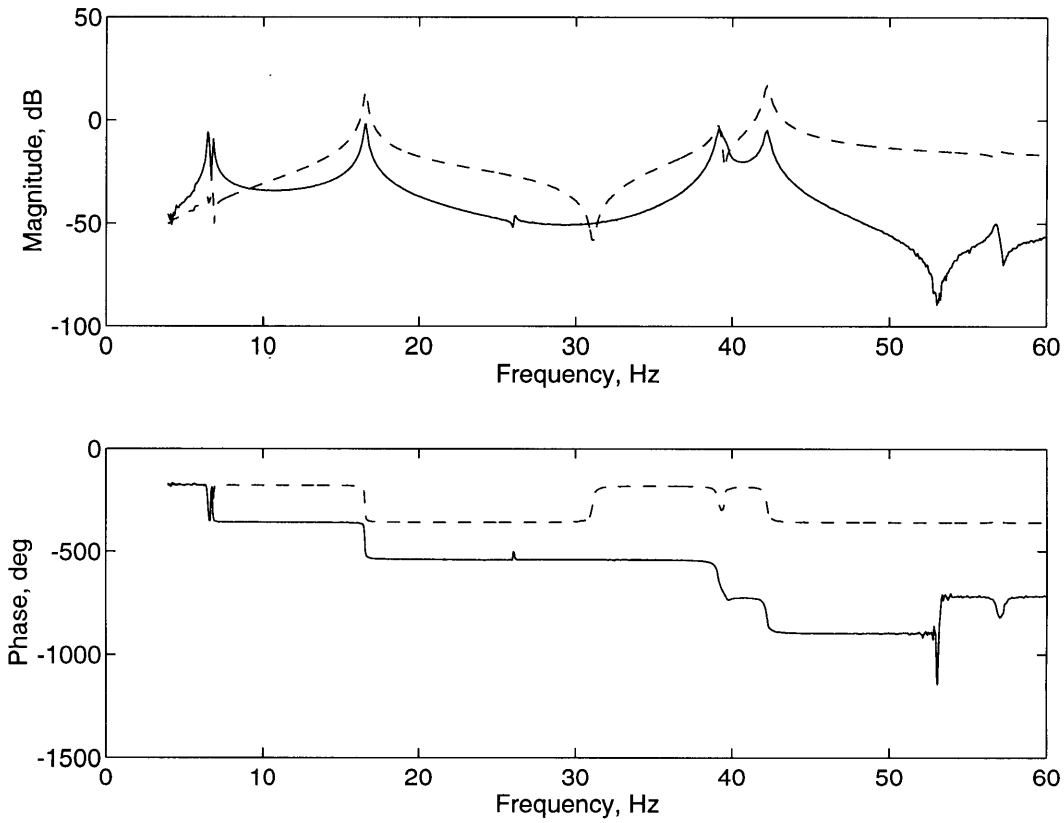

Figure 4.8: Measured FRF's for SV. (a) $--$, driving point FRF (b) — , tip mass FRF.

To provide a better indication of the z bending modes, Figure 4.9 shows the FRF for a tip mass DOF for excitation in the z direction. The z-bending antenna modes can now be seen. Table 4.7 summarizes the modal parameters that were obtained for the nine modes.

Upon comparing the measured frequencies with the original FEM predictions given in Table 3.2, it is noticed that the FEM overpredicts in all cases. This again is due to the use of rigid joints in the model. The higher stiffness results in higher frequencies. The largest discrepancy is in the antenna torsion modes. There is almost a 10 Hz difference between the analytical and measured frequencies. Also, unlike what was noticed in BV, the FEM global torsion mode occurs at a higher frequency than what was measured.

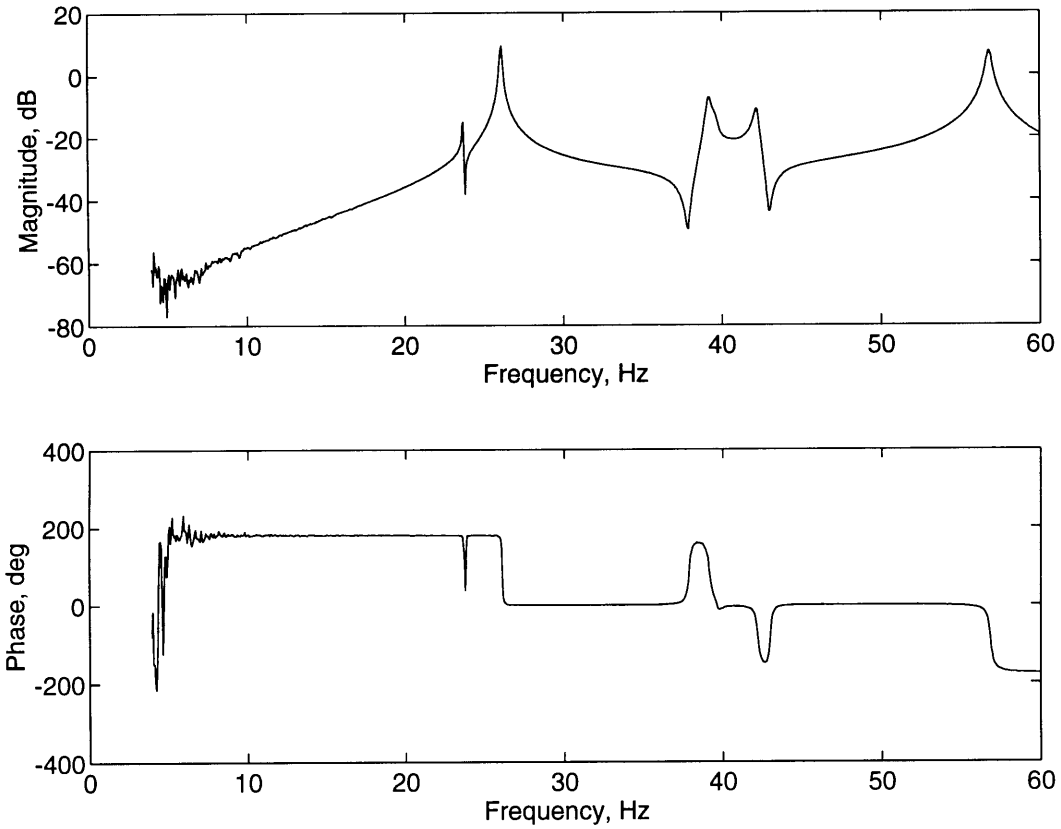

Figure 4.9: Measured FRF for SV (excitation in z, response in z).

Table 4.7: Measured Modes of SV

Mode #	Frequency (Hz)	Damping (%)	Description
1	6.47	0.26	antenna out-of-phase x-bending
2	6.79	0.27	antenna in-phase x-bending
3	16.55	0.30	x-bending (f1:+x)
4	23.67	0.08	antenna out-of-phase z-bending
5	26.06	0.14	antenna in-phase z-bending
6	39.10	0.39	antenna out-of-phase torsion
7	39.61	0.46	antenna in-phase torsion
8	42.18	0.30	torsion (f1:+ry)
9	56.77	0.25	z-bending (f1:+z)

Due to the difficulty in obtaining clean antenna torsion modes, their mode shapes were not extracted. As will become evident later on, the transient response tests were run at frequencies below these modes. This allowed the well-identified low-frequency modes to be used in the response predictions. It was these modes that were of interest since the added damping had a greater effect on them.

4.5.3 Coupled System

The total number of sensors used in the mode survey tests of the coupled system was greater than the number of channels available on the front-end. To accommodate this, two separate tests had to be performed to gather all the data. The accelerometers were divided into two groups—the x and z accelerometers were placed in one group, and the y accelerometers were placed in another. One test was run in which the measurements from the first group were taken. New cable connections were made to the front-end channels, and an identical test was run to acquire the y measurements. The two sets of data were then combined and used in the modal analysis. Figure 4.10 presents the driving point FRF's (excitation in x) for both damping cases. The measured frequencies and damping ratios are shown in Table 4.8 (no added damping) and in Table 4.9 (added damping).

Table 4.8: Measured Modes of BVSV Without Added Damping

Mode #	Frequency (Hz)	Damping (%)	Description
1	4.71	0.50	x-bending (f1,f2,f3,f4:$+x$)
2	6.62	0.17	antenna out-of-phase x-bending
3	7.08	0.20	antenna in-phase x-bending
4	13.91	0.19	x-bending (f1,f2:$+x$; f3,f4:$-x$)
5	15.06	0.21	torsion (f1,f2,f3,f4:$+ry$)
6	16.45	0.16	z-bending (f1,f2,f3,f4:$+z$)
7	20.94	0.14	x-bending (f1,f4:$+x$; f2,f3:$-x$)
8	24.06	0.09	antenna out-of-phase z-bending
9	24.98	0.11	x-bending (f1,f3:$+x$; f2,f4:$-x$)
10	27.39	0.08	antenna in-phase z-bending
11	40.47	0.16	antenna out-of-phase torsion
12	40.90	0.12	antenna in-phase torsion
13	42.58	0.19	torsion (f1,f2:$+ry$; f3,f4:$-ry$)
14	49.71	0.10	z-bending (f1,f2:$+z$; f3,f4:$-z$)

The same types of modes that can be found in BV and SV are also evident in the

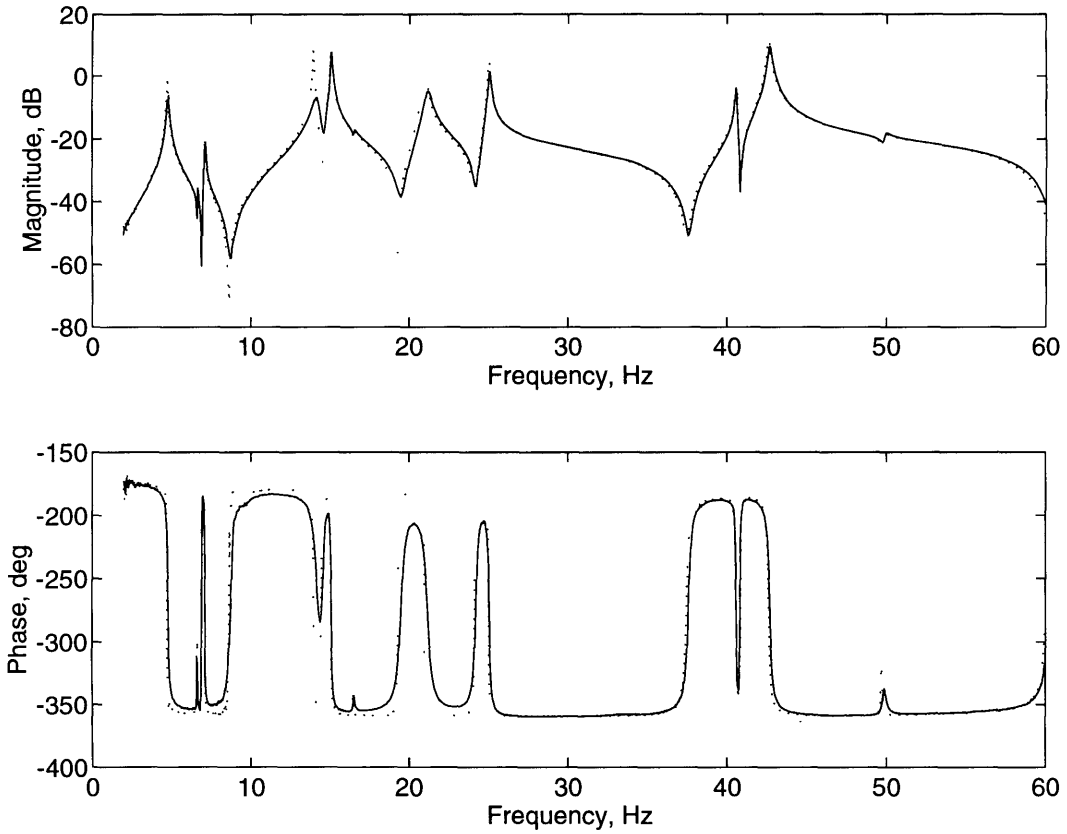

Figure 4.10: Measured driving point FRF's for BVSV with (—) and without (···) the added damping in BV.

Table 4.9: Measured Modes of BVSV With Added Damping

Mode #	Frequency (Hz)	Damping (%)	Description
1	4.77	1.27	x-bending (f1,f2,f3,f4:+x)
2	6.62	0.17	antenna out-of-phase x-bending
3	7.09	0.30	antenna in-phase x-bending
4	14.13	1.57	x-bending (f1,f2:+x ; f3,f4:−x)
5	15.08	0.30	torsion (f1,f2,f3,f4:+ry)
6	16.48	0.35	z-bending (f1,f2,f3,f4:+z)
7	21.13	1.04	x-bending (f1,f4:+x ; f2,f3:−x)
8	24.03	0.09	antenna out-of-phase z-bending
9	25.02	0.30	x-bending (f1,f3:+x ; f2,f4:−x)
10	27.37	0.09	antenna in-phase z-bending
11	40.55	0.10	antenna out-of-phase torsion
12	40.91	0.07	antenna in-phase torsion
13	42.67	0.27	torsion (f1,f2:+ry ; f3,f4:−ry)
14	49.84	0.30	z-bending (f1,f2:+z ; f3,f4:−z)

measured modes of the coupled system. Although some of the substructure modes (e.g., the SV antenna modes) remain dominant and isolated in the coupled system, there was a shift in frequencies. The global bending and torsion modes of BV dropped in frequency because of the additional mass due to SV, while all the antenna modes experienced slight increases in frequencies. The added damping continued to have the largest effect on the x-bending modes. As with the case of the tests on SV, the pure antenna torsion modes could not be obtained, but their frequencies and damping were measured. Chapter 6 will analytically couple the updated FEM's and compare the predicted natural frequencies and mode shapes with the measured values of these tests. Chapter 7 will use various methods to predict the measured system damping.

4.6 Measured Mode Checks

It was vital to check the quality of the extracted modes before they were used in subsequent analyses. There was no guarantee that an error had not occurred in either the testing or extraction stages. One common check was to see how close the modes came to satisfying orthogonality. It is known that true modes must be orthogonal to each other with respect to the mass matrix. This can be written as $\phi^T M \phi = I$, where ϕ is the modal matrix, M is the mass matrix, and I is the identity matrix. This assumes that the modes have been properly normalized to produce unity modal mass.

4.6.1 Substructure BV

The implementation of this check required that the measured modes be expanded to the DOF's of the mass matrix (i.e., the DOF's in the ASET). Instead of utilizing the expansion techniques mentioned in Section 3.4, the transformation matrix was assembled by hand using rigid-body assumptions. Table 4.10 shows the relationship between the non-measured and measured DOF's that together constitute the ASET for BV. The nodes are in the FEM numbering scheme, as given in Figure 3.4. Each ASET DOF is assigned the mode shape coefficient of the associated measured DOF. For instances where two measured DOF's are listed, then the ASET DOF is computed to be their average.

Thus, the self-orthogonality check can be determined by using the expanded measured modes, $\overline{\phi}_m$ (mass normalized), and the NASTRAN mass matrix, M_a. The computation

Table 4.10: Mapping Between ASET DOF's and Measured DOF's for BV ($\star$ represents accelerometer location)

ASET DOF	Msrd. DOF	ASET DOF	Msrd. DOF	ASET DOF	Msrd. DOF
6:x	$\star$	6:y	24:y	6:z	13:z
8:x	6:x	8:y	24:y,28:y	8:z	13:z,17:z
10:x	6:x	10:y	28:y	10:z	17:z
13:x	$\star$	13:y	31:y	13:z	$\star$
15:x	13:x	15:y	31:y,34:y	15:z	13:z,17:z
17:x	13:x	17:y	34:y	17:z	$\star$
24:x	$\star$	24:y	$\star$	24:z	31:z
26:x	24:x	26:y	24:y,28:y	26:z	31:z,35:z
28:x	24:x	28:y	$\star$	28:z	35:z
31:x	$\star$	31:y	$\star$	31:z	$\star$
33:x	31:x	33:y	31:y,35:y	33:z	31:z,35:z
35:x	31:x	35:y	$\star$	35:z	$\star$
42:x	$\star$	42:y	24:y	42:z	49:z
44:x	42:x	44:y	24:y,28:y	44:z	49:z,53:z
46:x	42:x	46:y	28:y	46:z	53:z
49:x	$\star$	49:y	31:y	49:z	$\star$
51:x	49:x	51:y	31:y,35:y	51:z	31:z,35:z
53:x	49:x	53:y	35:y	53:z	$\star$

$\overline{\phi}_m^T M_a \overline{\phi}_m$ yields a matrix that should approximate the identity matrix for cleanly-measured modes. This does assume that the mass matrix is exact, but since the model masses have been shown to be very close to the measured masses, this assumption is not unrealistic. Table 4.11 is the orthogonality check for the lightly damped BV, and Table 4.12 is the check for the added damping case. The established criterion at The Aerospace Corporation for well-extracted modes is that the off-diagonal terms should be less than 0.1. The maximum off-diagonal terms in the tables are boldfaced, and it can be seen that both cases easily satisfy this requirement. The modes have been normalized to produce values of 1 along the diagonal. The indices of an off-diagonal element refer to the two modes that contribute to that element. For example, if the $(2,3)$ term is relatively large, this means that the second measured mode is contaminated by motion corresponding to the third mode. The reverse is also true since the orthogonality matrix is symmetric.

To determine the effect that the damping had on the modes, a cross-orthogonality check was performed. This involves using both sets of modes in the triple product with the mass matrix. Table 4.13 shows the result, and it appears that minor changes occurred in the

Table 4.11: Orthogonality Check of Measured BV Modes

$$\begin{bmatrix} \mathbf{1.00} & -0.03 & \mathbf{-0.04} & 0.00 & 0.00 & -0.03 & 0.00 \\ -0.03 & \mathbf{1.00} & -0.01 & 0.00 & -0.01 & 0.00 & 0.00 \\ \mathbf{-0.04} & -0.01 & \mathbf{1.00} & -0.03 & -0.01 & -0.02 & 0.00 \\ 0.00 & 0.00 & -0.03 & \mathbf{1.00} & 0.00 & 0.00 & -0.02 \\ 0.00 & -0.01 & -0.01 & 0.00 & \mathbf{1.00} & -0.02 & 0.00 \\ -0.03 & 0.00 & -0.02 & 0.00 & -0.02 & \mathbf{1.00} & 0.00 \\ 0.00 & 0.00 & 0.00 & -0.02 & 0.00 & 0.00 & \mathbf{1.00} \end{bmatrix}$$

Table 4.12: Orthogonality Check of Measured BV Modes for Added Damping Case

$$\begin{bmatrix} \mathbf{1.00} & 0.03 & \mathbf{0.04} & 0.00 & 0.00 & 0.03 & 0.00 \\ 0.03 & \mathbf{1.00} & -0.02 & 0.00 & -0.02 & 0.00 & 0.00 \\ \mathbf{0.04} & -0.02 & \mathbf{1.00} & -0.03 & 0.00 & -0.02 & 0.00 \\ 0.00 & 0.00 & -0.03 & \mathbf{1.00} & 0.00 & 0.00 & -0.02 \\ 0.00 & -0.02 & 0.00 & 0.00 & \mathbf{1.00} & -0.03 & 0.00 \\ 0.03 & 0.00 & -0.02 & 0.00 & -0.03 & \mathbf{1.00} & 0.00 \\ 0.00 & 0.00 & 0.00 & -0.02 & 0.00 & 0.00 & \mathbf{1.00} \end{bmatrix}$$

Table 4.13: Cross-orthogonality of Measured BV Modes for Both Damping Cases

$$\begin{bmatrix} \mathbf{1.00} & -0.02 & 0.00 & 0.00 & 0.00 & 0.00 & 0.00 \\ 0.02 & \mathbf{1.00} & 0.00 & 0.00 & -0.03 & 0.00 & 0.00 \\ 0.00 & 0.00 & \mathbf{1.00} & \mathbf{0.04} & 0.00 & 0.00 & 0.00 \\ 0.00 & 0.00 & \mathbf{-0.04} & \mathbf{1.00} & 0.00 & 0.00 & 0.00 \\ 0.00 & 0.03 & 0.00 & 0.00 & \mathbf{1.00} & 0.00 & 0.00 \\ 0.00 & 0.00 & 0.00 & 0.00 & 0.00 & \mathbf{1.00} & 0.02 \\ 0.00 & 0.00 & 0.00 & 0.00 & 0.00 & -0.02 & \mathbf{1.00} \end{bmatrix}$$

mode shapes when the damping was added. Some coupling between modes 3 and 4 is evident, which seems to imply that the damping treatment caused some torsional motion to enter into the first z-bending mode.

4.6.2 Substructure SV

The orthogonality check for SV also required that the measured modes be expanded to the ASET DOF's of the FEM. The assumed relationships are given in Table 4.14. (Refer to Figure 3.4 for the node numbering.) The antenna torsion modes were not included, and this is the reason the matrix has a size of 7×7 instead of 9×9.

Table 4.14: Mapping Between ASET DOF's and Measured DOF's for SV ($\star$ represents accelerometer location)

ASET DOF	Msrd. DOF	ASET DOF	Msrd. DOF	ASET DOF	Msrd. DOF
6:x	$\star$	6:y	$\star$	6:z	$\star$
8:x	6:x	8:y	6:y	8:z	6:z,10:z
10:x	6:x	10:y	6:y	10:z	$\star$
13:x	$\star$	13:y	6:y	13:z	6:z
15:x	13:x	15:y	6y	15:z	6:z,10:z
17:x	13:x	17:y	6:y	17:z	10:z
19:x	$\star$	19:y	$\star$	19:z	$\star$
22:x	$\star$	22:y	19:y	22:z	$\star$
25:x	$\star$	25:y	19:y	25:z	$\star$

The resulting orthogonality check is given in Table 4.15. The diagonal terms and the largest off-diagonal terms are in boldface. The maximum off-diagonal elements have a

Table 4.15: Orthogonality Check of Measured SV Modes

$$\begin{bmatrix} \mathbf{1.00} & -0.04 & 0.00 & -0.01 & 0.01 & -0.02 & 0.00 \\ -0.04 & \mathbf{1.00} & 0.01 & 0.00 & 0.02 & -0.02 & 0.00 \\ 0.00 & 0.01 & \mathbf{1.00} & 0.00 & 0.00 & 0.02 & 0.00 \\ -0.01 & 0.00 & 0.00 & \mathbf{1.00} & 0.03 & 0.00 & 0.02 \\ 0.01 & 0.02 & 0.00 & 0.03 & \mathbf{1.00} & \mathbf{-0.06} & 0.00 \\ -0.02 & -0.02 & 0.02 & 0.00 & \mathbf{-0.06} & \mathbf{1.00} & 0.01 \\ 0.00 & 0.00 & 0.00 & 0.02 & 0.00 & 0.01 & \mathbf{1.00} \end{bmatrix}$$

magnitude of 0.06, which is still below the 0.1 level. The two modes that have the most coupling are the antenna in-phase z-bending mode and the global torsion mode.

4.6.3 Coupled System

The expansion of the modes of BVSV utilized most of the same relationships described in Tables 4.10 and 4.14. One difference was that instead of having only one accelerometer measure the y motion of the floor of SV, a total of four were used. Since this floor of SV was now located at a height that was three times as great, the axial motion would be larger, but to what extent was not known. The additional relationships only affected the y DOF's and will not be given here because the x and z motions were the most important, and these relationships have been previously stated.

The analytical mass matrix of BVSV used in the orthogonality checks did come from a finite element model of the coupled system. This model, however, was generated solely for this purpose. The coupling procedure described in Chapter 6 was the method employed to predict the modes of BVSV.

The orthogonality check for the modes of BVSV without the damping treatment is given in Table 4.16. When damping was added, the check on the measured modes produced a similar result, which is shown in Table 4.17. (Because of width considerations, only the magnitudes of all terms are shown.) The two antenna torsion modes were not included in either modal matrix. Thus, columns (rows) 11 and 12 correspond to modes 13 and 14.

Table 4.16: Orthogonality Check of Measured BVSV Modes

$$\begin{bmatrix}
\mathbf{1.00} & 0.04 & 0.01 & 0.01 & 0.02 & 0.00 & 0.00 & 0.00 & 0.00 & 0.00 & 0.00 & 0.00 \\
0.04 & \mathbf{1.00} & 0.05 & 0.00 & 0.00 & 0.00 & 0.00 & 0.03 & 0.00 & 0.01 & 0.01 & 0.00 \\
0.01 & 0.05 & \mathbf{1.00} & 0.01 & 0.00 & 0.00 & 0.00 & 0.00 & 0.00 & 0.02 & 0.00 & 0.00 \\
0.01 & 0.00 & 0.01 & \mathbf{1.00} & 0.01 & 0.00 & 0.01 & 0.00 & 0.00 & 0.00 & 0.00 & 0.00 \\
0.02 & 0.00 & 0.00 & 0.01 & \mathbf{1.00} & 0.03 & 0.00 & 0.00 & 0.02 & 0.00 & \mathbf{0.08} & 0.00 \\
0.00 & 0.00 & 0.00 & 0.00 & 0.03 & \mathbf{1.00} & 0.00 & 0.03 & 0.00 & 0.02 & 0.01 & 0.01 \\
0.00 & 0.00 & 0.00 & 0.01 & 0.00 & 0.00 & \mathbf{1.00} & 0.00 & 0.02 & 0.00 & 0.00 & 0.00 \\
0.00 & 0.03 & 0.00 & 0.00 & 0.00 & 0.03 & 0.00 & \mathbf{1.00} & 0.00 & 0.02 & 0.00 & 0.01 \\
0.00 & 0.00 & 0.00 & 0.00 & 0.02 & 0.00 & 0.02 & 0.00 & \mathbf{1.00} & 0.00 & 0.00 & 0.00 \\
0.00 & 0.01 & 0.02 & 0.00 & 0.00 & 0.02 & 0.00 & 0.02 & 0.00 & \mathbf{1.00} & 0.06 & 0.00 \\
0.00 & 0.01 & 0.00 & 0.00 & \mathbf{0.08} & 0.01 & 0.00 & 0.00 & 0.00 & 0.06 & \mathbf{1.00} & 0.03 \\
0.00 & 0.00 & 0.00 & 0.00 & 0.00 & 0.01 & 0.00 & 0.01 & 0.00 & 0.00 & 0.03 & \mathbf{1.00}
\end{bmatrix}$$

The measured modes in both damping cases still exhibit good orthogonality. The largest off-diagonal terms in both checks have magnitudes of 0.08, which is close to the limit of 0.1, but is still satisfactory. This coupling appears in the first two global torsion modes.

Table 4.17: Orthogonality Check of Measured BVSV Modes (Added Damping Case)

1.00	0.03	0.03	0.02	0.02	0.00	0.00	0.02	0.00	0.00	0.00	0.00
0.03	**1.00**	0.07	0.00	0.00	0.00	0.00	0.03	0.00	0.01	0.01	0.00
0.03	0.07	**1.00**	0.02	0.01	0.00	0.00	0.01	0.00	0.02	0.00	0.00
0.02	0.00	0.02	**1.00**	0.01	0.00	0.02	0.00	0.00	0.00	0.00	0.00
0.02	0.00	0.01	0.01	**1.00**	0.03	0.00	0.00	0.02	0.00	**0.08**	0.00
0.00	0.00	0.00	0.00	0.03	**1.00**	0.00	0.00	0.00	0.02	0.02	0.01
0.00	0.00	0.00	0.02	0.00	0.00	**1.00**	0.00	0.02	0.00	0.00	0.00
0.02	0.03	0.01	0.00	0.00	0.00	0.00	**1.00**	0.00	0.04	0.06	0.07
0.00	0.00	0.00	0.00	0.02	0.00	0.02	0.00	**1.00**	0.00	0.00	0.00
0.00	0.01	0.02	0.00	0.00	0.02	0.00	0.04	0.00	**1.00**	0.06	0.00
0.00	0.01	0.00	0.00	**0.08**	0.02	0.00	0.06	0.00	0.06	**1.00**	0.04
0.00	0.00	0.00	0.00	0.00	0.01	0.00	0.07	0.00	0.00	0.04	**1.00**

As was done for BV, the cross-orthogonality between the two sets of modes can be computed and used to examine the effect that the damping had on the mode shapes. This is shown in Table 4.18, and it is evident that there is good correlation between the modes.

Table 4.18: Cross-orthogonality Check of Measured BVSV Modes for Both Damping Cases

1.00	0.00	0.02	0.01	0.00	0.00	0.00	0.01	0.00	0.00	0.00	0.00
0.00	**1.00**	0.00	0.00	0.00	0.00	0.00	0.00	0.00	0.00	0.00	0.00
0.02	0.00	**1.00**	0.00	0.00	0.00	0.00	0.00	0.00	0.00	0.00	0.00
0.01	0.00	0.00	**1.00**	0.00	0.00	**0.03**	0.00	0.00	0.00	0.00	0.00
0.00	0.00	0.00	0.00	**1.00**	0.01	0.00	0.00	0.00	0.00	0.00	0.00
0.00	0.00	0.00	0.00	0.01	**1.00**	0.00	0.00	0.00	0.00	0.00	0.00
0.00	0.00	0.00	**0.03**	0.00	0.00	**1.00**	0.00	0.02	0.00	0.00	0.00
0.01	0.00	0.00	0.00	0.00	0.00	0.00	**1.00**	0.00	0.00	**0.03**	**0.03**
0.00	0.00	0.00	0.01	0.00	0.00	0.02	0.00	**1.00**	0.00	0.00	0.00
0.00	0.00	0.00	0.00	0.00	0.00	0.00	0.00	0.00	**1.00**	0.00	0.00
0.00	0.00	0.00	0.00	0.00	0.00	0.00	**0.03**	0.00	0.00	**1.00**	0.01
0.00	0.00	0.00	0.00	0.00	0.00	0.00	**0.03**	0.00	0.00	0.01	**1.00**

4.7 Orthogonalization of Measured Modes

The fact that the orthogonality checks do not exactly produce identity matrices implies that the measured modes are not orthogonal with respect to the analytical mass matrix. The off-diagonal terms, however, are small, which suggests that the measured modes are

very close to satisfying the orthogonality condition. For a better comparison with the analytical modes during the update of the substructure models, the measured modes can be corrected so that they indeed meet the orthogonality criteria. (The analytical modes automatically satisfy the condition since they are derived from the mass and stiffness matrices.) A correction matrix C is sought such that if $\overline{\phi}_m$ are the expanded, measured modes, then the product $\overline{\phi}_m C$ will produce new modes ϕ_m that are orthogonal. It is shown in [26] that if only small errors are present, then any corrections to the measured modes based on orthogonality will only correct symmetric errors. If a symmetric C is assumed, then C can be determined as follows. The orthogonalized modes ϕ_m should satisfy

$$\phi_m^T M_a \phi_m = I \tag{4.3}$$

Substituting $\phi_m = \overline{\phi}_m C$ results in

$$(\overline{\phi}_m C)^T M_a (\overline{\phi}_m C) = I$$

$$C^T \overline{\phi}_m^T M_a \overline{\phi}_m C = I$$

$$C^T (\overline{\phi}_m^T M_a \overline{\phi}_m) C = I$$

But the symmetry of C implies $C^T = C$, which leads to

$$(\overline{\phi}_m^T M_a \overline{\phi}_m) = (C^{-1})(C^{-1}) = C^{-2}$$

The left-hand side of the equation is just the orthogonality check that was performed in the previous section. The required C is given by

$$C = (\overline{\phi}_m^T M_a \overline{\phi}_m)^{-\frac{1}{2}} \tag{4.4}$$

and the corrected modes are

$$\phi_m = \overline{\phi}_m (\overline{\phi}_m^T M_a \overline{\phi}_m)^{-\frac{1}{2}} \tag{4.5}$$

To compute the inverse square root, let $\overline{\phi}_m^T M_a \overline{\phi}_m = \overline{I}$. If Λ is the diagonal matrix of eigenvalues and Θ is the matrix of eigenvectors corresponding to $\overline{I}$, then

$$\overline{I}^{-\frac{1}{2}} = \Theta \Lambda^{-\frac{1}{2}} \Theta^T \tag{4.6}$$

All of the measured modes extracted in the mode survey tests were orthogonalized using the symmetric correction matrix procedure outlined above. The FEM updates discussed in the next chapter sought to produce analytical modes that were as close as possible to the corrected modes.

Chapter 5

Finite Element Model Updates

Once the mode shapes and frequencies of the substructures were obtained experimentally, the next step was to adjust the finite element models (FEM's) so that the analytical modes were closer to the measured ones. The refined substructure models could then be used in the coupling procedure in order to predict the modes of the complete system. This chapter presents the guidelines that were followed and the general approach taken during modification of the models. The criteria that were established to determine successful updates are then specified. Finally, the results are given for the different substructures.

5.1 Strategy

The main goal of the update process was to yield models that reproduced the measured dynamic properties as closely as possible. Since FEM's are usually representative of the undamped structures (only the mass and stiffness properties are considered), the only comparison that could be made was between the undamped mode shapes and natural frequencies. For the levels of damping in the tests, the damped natural frequencies were, for all practical purposes, equal to the undamped natural frequencies. Also, the amplitude normalization technique mentioned in Chapter 4 was used to approximate undamped mode shapes from the measured complex modes. Thus, the undamped properties could be obtained from the extracted modes and compared with the FEM results.

There are numerous approaches that have been developed to bring a FEM into better agreement with test results. Some use input/output responses (usually in the form of transfer functions) to compare analytical predictions with the measured responses. (Refer

to [2] for a practical example.) Although this has the advantage of not having to pair analytical and experimental modes, the analytical model does have to incorporate damping, something which the FEM lacks. Probably the most widely used means of comparison is based on normal modes. The FEM is adjusted until certain criteria that deal with the normal modes are met.

The adjustments can occur at two distinct levels. The mass and stiffness matrices can be directly altered, or the focus can be on the element parameters given in the bulk data of the FEM. The various mathematically-based methods of the mass/stiffness approach usually work on the stiffness matrix alone or a combination of the mass and stiffness matrices. (For example, see [9] or [19].) The analytical modes obtained from the modified M and K can be made to reproduce the measured modes exactly. Although the result is what is desired, these methods tend to make arbitrary changes to the matrices, sometimes in ways that are not consistent with the true properties of the structure. Because the modifications are not justifiable, recent trends have steered away from these techniques and have centered on ways to adjust the design parameters in the FEM. As a result, the parameter update approach was used in the project.

Before the errors due to inaccurate parameters could be considered, it was necessary to ensure that there were no other sources of errors. These other types are non-parametric in nature and can be attributed to such things as simple input errors in the FEM bulk data or improper modeling of the structure. One example is how the mass matrix was formulated. Initially, a lumped mass approach was specified, but this resulted in a significant difference between the predicted and analytical frequencies of the torsion modes. At the start of the update process, it soon became apparent that this presented a serious problem. The bending modes occurred at frequencies that were higher than the measurements. This suggested that the joint stiffnesses needed to be made softer. The torsion modes, on the other hand, occurred at frequencies that were lower than the measured values. Making the joints softer would only worsen these frequencies. Such a contradiction could only be remedied by specifying a consistent mass matrix, which resulted in more manageable torsional frequencies.

Once it was determined that such discrepancies had been eliminated, the choice of which parameters to update could be made. For complicated structures, the location of regions needing modification can be identified by techniques such as the one presented in [21];

however, due to the simplified nature of the substructures, these regions were determined by inspection. The joints were obvious locations of initial error in system properties. The spring elements at the joints were purposely introduced to permit changes in the stiffness properties. The antenna assembly was another area in which small initial errors could cause significant differences in results. The top and bottom portions of the antenna were modeled as being perfectly symmetric about the center cross-beam. Any difference in length between the upper and lower beams, for example, would result in non-symmetric antenna bending modes.

In general, errors in mass were considered to be negligible (once a consistent mass matrix was specified). The measured mass of each component had been used to obtain the element densities, and the total model mass was extremely close to the measured mass of the substructures. Thus, the mass properties were very well known. The two locations at which changes were made were the two tip masses. Accounting for the additional weight of the accelerometers did have a small, but significant, effect on the frequencies of the antenna modes.

Geometrical measurement errors were also neglected for the most part. The various components had been machined to specified dimensions, and it was these values that were used in determining such properties as cross-sectional area and moments of inertia. The dimensions that were not known with as much certainty were the exposed lengths of the vertical beams. They depended more on the act of assembly rather than machining. Table 5.1 summarizes the parameters considered for updating.

Table 5.1: Parameters Identified for Potential Updating

Parameter	SV Model		BV Model	
Description	# Available	# Changed	# Available	# Changed
Spring constants of				
base joints	6	3	12	6
regular joints	12	2	12	2
antenna joints	24	18	—	—
VEM	—	—	6	2
Added antenna tip mass	2	2	—	—
Antenna length	2	2	—	—

Having identified possible parameters to be updated, the actual update process could

begin. Normally, a formal sensitivity analysis is performed that provides a quantitative measure of how small modifications to certain parameters affect the analytical mode shapes and frequencies, and this usually involves perturbation analysis. However, the relative simplicity of the substructures enabled the sensitivities to be obtained qualitatively by intuition. For instance, considering the spring elements of the joints at the base, it was assumed that the ry spring constants had the most effect on the torsion modes, that the rz spring constants affected primarily the x-bending modes, and that the rx spring constants contributed mostly to the z-bending modes. Similar relationships were also assumed to be valid for the other joints as well.

The updates were a trial-and-error process that consisted of targeting modes one at a time and determining the required parameter changes that would bring the specific mode shape and frequency closer to the measured values. The various spring constants were modified first as much as possible until no further improvements could be made. For the case of substructure BV, this was all that was needed, but for the case of SV, a few extra mass and length considerations (mentioned above) resulted in even better results.

A short FORTRAN program was written to take the mass and stiffness matrices of the altered model and compare the predicted modes with the measured modes. If the modification produced an improved result, the parameter was further changed. This was repeated until a somewhat optimum value was found. A new mode was then targeted, the applicable parameter identified, and the trial-and-error iteration performed again. During these steps, the sensitivities described above became apparent. The process was made easier by the fact that there existed a one-to-one correspondence between certain modes and spring constants. This meant that a change in a spring constant corresponding to an ry DOF would primarily affect the torsional modes. The effects on the other types of modes would not be noticeable. There were some instances in the antenna modes when a change would improve, say, the in-phase bending mode, but would cause the out-of-phase bending mode to become worse. In such cases, an acceptable compromise was found. The total number of parameters that were changed is given in Table 5.1.

5.2 Success Criteria

The degree of correlation between the experimental and analytical normal modes was determined by checks on the orthogonality and natural frequencies. If the FEM mode shapes, ϕ_a, are similar to the measured mode shapes, ϕ_m, then the cross-orthogonality between the two sets of modes should be nearly satisfied. This implies that

$$\phi_a{}^T M_a \phi_m = \overline{I} \approx I \tag{5.1}$$

assuming that the modes are normalized so that they produce unity modal mass. The criteria used at The Aerospace Corporation to establish acceptable analytical mode shapes are

$$\left|\overline{I}_{ij}\right| \begin{cases} \geq 0.95 & \text{for } i = j \\ \leq 0.10 & \text{for } i \neq j \end{cases} \tag{5.2}$$

Not only must the mode shapes be similar, but the natural frequencies should be close as well. A good cross-orthogonality check does not necessarily imply that the predicted and measured frequencies will be in agreement. A simple measure of the difference in frequencies is the percent error. If $f_a^{(i)}$ is the natural frequency of the ith FEM mode, and $f_m^{(i)}$ corresponds to the ith measured mode, then it has been found through experience that the criterion

$$\left|\frac{f_a^{(i)} - f_m^{(i)}}{f_m^{(i)}}\right| \times 100\% \leq 3\% \quad \text{for all } i \tag{5.3}$$

is an acceptable condition for frequency correlation.

Equations 5.2 and 5.3 should be satisfied simultaneously in order to say that the FEM update has been successful. The FORTRAN program that was used did compute both checks after each change in the FEM. The iterations were continued until it became apparent that no further changes caused appreciable improvements, and at that point, the FEM was considered to be correlated with the test results.

5.3 Results

The entire process described in the previous sections was performed for substructure BV (for both damping cases) and for substructure SV. The amount of success is shown in terms of the cross-orthogonality and frequency error checks.

5.3.1 Substructure BV

The only changes that needed to be made in the model of BV without the added damping were in the spring constants specified in the PELAS cards. The torsional spring constants corresponding to rotational DOF's about the x and z axes were lowered by factors on the order of 10^5. Table 5.2 shows the cross-orthogonality check of the final model.

Table 5.2: Cross-orthogonality Check Between Updated FEM and Measured BV Modes (No Added Damping)

$$\begin{bmatrix} \mathbf{1.00} & 0.00 & 0.00 & 0.00 & 0.00 & 0.00 & 0.00 \\ 0.00 & \mathbf{1.00} & 0.00 & -0.01 & 0.00 & 0.00 & 0.00 \\ 0.00 & 0.00 & \mathbf{1.00} & 0.03 & 0.00 & 0.00 & 0.00 \\ 0.00 & 0.01 & -0.03 & \mathbf{1.00} & 0.00 & 0.00 & 0.00 \\ 0.00 & 0.00 & 0.00 & 0.00 & \mathbf{1.00} & 0.00 & 0.00 \\ 0.00 & 0.00 & 0.00 & 0.00 & 0.00 & \mathbf{1.00} & \mathbf{0.05} \\ 0.00 & 0.00 & 0.00 & 0.00 & 0.00 & \mathbf{-0.05} & \mathbf{1.00} \end{bmatrix}$$

The diagonal terms did not exactly equal 1, but were typically like 0.9998. Thus, to two decimal places, these terms rounded to 1.00. The largest off-diagonal terms have magnitudes of 0.05, and it is quite apparent that the two sets of mode shapes are very similar. The frequency errors are presented below, and the maximum error is about 1.5% for the updated model, in contrast to the maximum error of 15.5% in the original model. Both checks indicate a successful update.

Mode #	1	2	3	4	5	6	7
% error (updated model)	−0.02	−0.85	0.20	1.51	−0.13	−0.90	−1.05
Avg. magnitude % error = 0.67%					Std. deviation = 0.56		
% error (original model)	6.29	5.45	−9.74	15.5	4.90	−14.5	9.90
Avg. magnitude % error = 9.47%					Std. deviation = 4.26		

For the case of added damping, the FEM had to be slightly altered to include spring elements at the location of the viscoelastic material. It was evident during testing that the material did introduce some stiffness since the frequencies of the modes increased. As before, only changes in joint spring constants were required to yield a satisfactory updated model. The spring constants of the elements at the damping location that were found to be needed corresponded to translation in the x and z directions. (Refer to the NASTRAN bulk data in Appendix A.1 for the specific constants used in the PELAS cards.) The cross-

Table 5.3: Cross-orthogonality Check Between Updated FEM and Measured BV Modes (Added Damping)

$$\begin{bmatrix} \mathbf{1.00} & 0.00 & 0.00 & 0.00 & 0.00 & 0.00 & 0.00 \\ 0.00 & \mathbf{1.00} & 0.00 & -0.01 & 0.00 & 0.00 & 0.00 \\ 0.00 & 0.00 & \mathbf{1.00} & 0.04 & 0.00 & 0.00 & 0.00 \\ 0.00 & 0.01 & -0.04 & \mathbf{1.00} & 0.00 & 0.00 & 0.00 \\ 0.00 & 0.00 & 0.00 & 0.00 & \mathbf{1.00} & 0.00 & 0.00 \\ 0.00 & 0.00 & 0.00 & 0.00 & 0.00 & \mathbf{1.00} & \mathbf{-0.07} \\ 0.00 & 0.00 & 0.00 & 0.00 & 0.00 & \mathbf{0.07} & \mathbf{1.00} \end{bmatrix}$$

orthogonality check in Table 5.3 shows that all the diagonal terms still round to a value of 1.00, and that the maximum off-diagonal terms now have magnitudes of 0.07. This increase reveals that the damping treatment has caused more coupling between the second torsion and z-bending modes to occur. Nevertheless, the check still satisfies the requirement that the off-diagonal terms be less than 0.10. The frequency errors are given below, and the maximum error of 1.5% is safely within the 3% criterion. The average magnitude error has seen an increase from the case of no added damping.

Mode #	1	2	3	4	5	6	7
% error	0.50	−1.23	0.22	1.50	−0.34	−0.96	−1.19
Avg. magnitude % error = 0.85%					Std. deviation = 0.50		

5.3.2 Substructure SV

Not only were changes in the joint stiffnesses needed for the update on the SV model, but length and mass alterations of the antenna assembly were required as well. When the experimental antenna bending modes were animated, a non-symmetric behavior was observed. The motion of one of the tip masses was either larger or smaller than the motion of the other. To accommodate this, different spring elements were prescribed for the upper and lower intersection of the cross-beam and the vertical tip mass beam. In addition, it was conceivable that an error on the order of $\frac{1}{16}''$ was possible when measuring the exposed lengths of the upper and lower portion of the tip mass beam. The upper length was increased by this amount, while the lower length was decreased by the same amount. It was found that accounting for the masses of the two accelerometers on each of the tip masses helped to reduce the frequencies of the antenna modes. These changes can be found in the NASTRAN model of SV in Appendix A.2. The resulting cross-orthogonality check in Table 5.4 shows

that one of the diagonal elements no longer rounds to 1.00, but it is above the established cutoff value of 0.95. The largest off-diagonal term of 0.06 indicates that the analytical and measured mode shapes correlate reasonably well.

Table 5.4: Cross-orthogonality Check Between Updated FEM and Measured SV Modes

$$\begin{bmatrix} \mathbf{1.00} & -0.03 & 0.00 & 0.00 & 0.00 & 0.00 & 0.00 \\ 0.03 & \mathbf{1.00} & 0.00 & 0.00 & 0.00 & 0.00 & 0.00 \\ 0.00 & 0.00 & \mathbf{1.00} & 0.00 & 0.00 & 0.00 & 0.00 \\ 0.00 & 0.00 & 0.00 & \mathbf{1.00} & 0.03 & 0.02 & 0.00 \\ 0.00 & 0.00 & 0.00 & -0.03 & \mathbf{1.00} & 0.02 & 0.00 \\ 0.00 & 0.00 & 0.01 & -0.02 & -0.02 & \mathbf{0.99} & \mathbf{-0.06} \\ 0.00 & 0.00 & 0.00 & 0.00 & 0.00 & \mathbf{0.06} & \mathbf{1.00} \end{bmatrix}$$

Mode #	1	2	3	4	5	6	7
% error (updated model)	−0.21	−1.92	0.08	2.01	−2.10	−0.54	−0.75
Avg. magnitude % error = 1.09%					Std. deviation = 0.89		
% error (original model)	9.43	6.48	7.43	14.2	11.7	1.75	23.2
Avg. magnitude % error = 10.6%					Std. deviation = 6.83		

The frequency errors shown above are generally larger than the errors found in the two BV cases. The largest magnitude error of 2.1% is nearer the critical value of 3%, but it still meets the criterion. The original model has a maximum error of 23.2%. One of the main problems encountered during the update process was that the antenna z-bending modes (modes 4 and 5) would respond differently to changes made to correct the frequencies. An attempt to reduce the error in mode 4 would cause the error in mode 5 to increase. A compromise was reached that allowed these errors to be on the order of 2%, but opposite in sign. A similar, but not as severe, problem occurred in the antenna x-bending modes (modes 1 and 2). It should be noted that the seven modes shown do *not* include the antenna torsion modes. (Reasons for their neglect were given in the previous chapter.) The analytical frequencies of these modes, however, were adjusted to better match the measured values, and the corresponding frequency errors that were achieved were 0.46% and 0.09%, respectively.

Chapter 6

Analytical Substructure Coupling

The updated finite element models of the substructures can be analytically coupled in order to predict the modes of the complete system. The specific method that is outlined in this chapter is applicable to the type of component modes measured in the mode survey tests. After the method is explained mathematically, the actual implementation of it will be described. The resulting predicted system modes are then compared to the corresponding measured system modes. This provides an indication of the accuracy of the coupling procedure.

6.1 Component Mode Substitution Method

The coupling of substructures for dynamic analysis usually involves a form of the general technique known as component mode synthesis. First developed by Hurty in 1965 ([17]), component mode synthesis utilizes various types of substructure modes and enforces compatibility and equilibrium along the interfaces, which leads to a system model. The use of a truncated set of modes reduces the number of generalized DOF's of a system and can yield an accurate representation of its dynamic properties. Numerous other papers on component mode synthesis have appeared (e.g., [8], [15], [3], [25]), and the generality of the method has increased significantly. The constraints placed on the interface DOF's of component modes have been reduced over the years since the presentation of Hurty's original method, and now methods involving complex modes for cases of damped structures and methods in the frequency domain have evolved. For a review of component mode synthesis techniques, refer to [7].

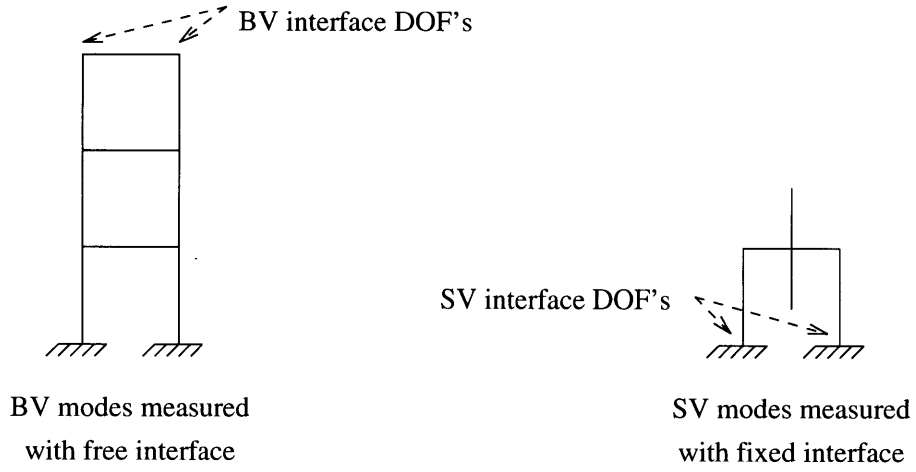

Figure 6.1: Substructure interface DOF's during testing.

The specific method that was employed to couple the models of substructures BV and SV is referred to as Component Mode Substitution, and was introduced by Benfield and Hruda ([3]) in 1971. This method is particularly suited to the current project because of the manner in which the substructures were tested. It requires that if the modes of one component are computed with interface DOF's fixed, then the modes of the other component must be computed with interface DOF's free. Although this technique is not as general as others, it is often used to couple launch vehicle models to payload models. Figure 6.1 shows how this requirement is satisfied by the configuration of the substructures during modal testing.

The notation that will be used to describe the DOF's is as follows:

$\overline{x}_B$ = BV interface DOF's

$\hat{x}_B$ = BV non-interface DOF's

$\overline{x}_S$ = SV interface DOF's

$\hat{x}_S$ = SV non-interface DOF's

The undamped equations of motion for the uncoupled components can be combined and written as

$$M\ddot{x} + Kx = F \tag{6.1}$$

where

$$M = \begin{bmatrix} [M_B] & 0 \\ 0 & [M_S] \end{bmatrix}, \quad K = \begin{bmatrix} [K_B] & 0 \\ 0 & [K_S] \end{bmatrix}, \quad \text{and} \quad x = \begin{Bmatrix} x_B \\ x_S \end{Bmatrix} = \begin{Bmatrix} \hat{x}_B \\ \overline{x}_B \\ \hat{x}_S \\ \overline{x}_S \end{Bmatrix}$$

To improve the accuracy of the method, approximate dynamic effects due to SV can be obtained by collapsing its mass and stiffness properties onto the interface DOF's, and then "loading" them onto the interface DOF's of BV. This results in the calculated interface-loaded modes of BV more closely resembling the system modes.

Let the static response of SV be determined by

$$\begin{Bmatrix} \hat{F}_S \\ \overline{F}_S \end{Bmatrix} = \begin{bmatrix} K_{NN} & K_{NI} \\ K_{IN} & K_{II} \end{bmatrix}_S \begin{Bmatrix} \hat{x}_S \\ \overline{x}_S \end{Bmatrix} \tag{6.2}$$

where $[K_S]$ has been partitioned according to non-interface and interface DOF's. To relate internal DOF's to interface DOF's, external forces at the internal DOF's are set to zero (i.e., $\hat{F}_S = 0$). Equation 6.2 can be used to show that the relation between $\hat{x}_S$ and $\overline{x}_S$ is given by

$$\{\hat{x}_S\} = -[(K_{NN})_S^{-1}][(K_{NI})_S]\{\overline{x}_S\} = [T_c]\{\overline{x}_S\} \tag{6.3}$$

where the columns of $[T_c]$ are commonly called the constraint modes. Thus,

$$\begin{Bmatrix} \hat{x}_S \\ \overline{x}_S \end{Bmatrix} = \begin{bmatrix} T_c \\ I \end{bmatrix} \{\overline{x}_S\} \tag{6.4}$$

To determine the reduced-mass and reduced-stiffness matrices, the expressions for kinetic energy and potential energy can be written by making use of Equation 6.4.

$$\begin{aligned} \text{KE} &= \frac{1}{2}\{\dot{x}_S\}^T[M_S]\{\dot{x}_S\} = \frac{1}{2}\{\dot{\overline{x}}_S\}^T \underbrace{\begin{bmatrix} T_c \\ I \end{bmatrix}^T \begin{bmatrix} M_{NN} & M_{NI} \\ M_{IN} & M_{II} \end{bmatrix}_S \begin{bmatrix} T_c \\ I \end{bmatrix}}_{\equiv \left[\overline{M}_S\right]} \{\dot{\overline{x}}_S\} \\ &= \frac{1}{2}\{\dot{\overline{x}}_S\}^T \left[\overline{M}_S\right] \{\dot{\overline{x}}_S\} \end{aligned} \tag{6.5}$$

$$\begin{aligned} \text{PE} &= \frac{1}{2}\{x_S\}^T[K_S]\{x_S\} = \frac{1}{2}\{\overline{x}_S\}^T \underbrace{\begin{bmatrix} T_c \\ I \end{bmatrix}^T \begin{bmatrix} K_{NN} & K_{NI} \\ K_{IN} & K_{II} \end{bmatrix}_S \begin{bmatrix} T_c \\ I \end{bmatrix}}_{\equiv\left[\overline{K}_S\right]} \{\overline{x}_S\} \\ &= \frac{1}{2}\{\overline{x}_S\}^T\left[\overline{K}_S\right]\{\overline{x}_S\} \end{aligned} \tag{6.6}$$

Both the reduced-mass matrix, $\left[\overline{M}_S\right]$, and the reduced-stiffness matrix, $\left[\overline{K}_S\right]$, can be expressed in terms of a triple product. These matrices can then be "overloaded" onto the interface portions of the mass and stiffness matrices of BV in order to solve for the interface-loaded modes, $[\phi]_{BL}$, and frequencies, ω^2_{BL}, which satisfy for the i th mode

$$\left(-(\omega^2_{BL})_i \begin{bmatrix} (M_{NN})_B & (M_{NI})_B \\ (M_{IN})_B & (M_{II})_B + \overline{M}_S \end{bmatrix} + \begin{bmatrix} (K_{NN})_B & (K_{NI})_B \\ (K_{IN})_B & (K_{II})_B + \overline{K}_S \end{bmatrix}\right) \begin{Bmatrix} \hat{\phi}_i \\ \overline{\phi}_i \end{Bmatrix}_{BL} = 0 \tag{6.7}$$

The modes needed from SV are its "cantilever" modes, and they correspond to the solution of

$$\left[-(\omega^2_S)_i(M_{NN})_S + (K_{NN})_S\right]\{\hat{\phi}_i\}_S = 0 \tag{6.8}$$

where ω^2_S are the frequencies of the fixed-interface modes $[\hat{\phi}_S]$. As can be seen, only the non-interface portions of $[M_S]$ and $[K_S]$ are used.

The coupling procedure begins by expressing the non-interface displacements of SV in terms of displacements relative to the fixed interface, $\hat{x}_R$, plus displacements resulting from motion of the interface. This leads to

$$\{\hat{x}_S\} = \{\hat{x}_R\} + [T_c]\{\overline{x}_S\} \tag{6.9}$$

where $\{\hat{x}_R\}$ represents the relative coordinates, and $[T_c]$ is the constraint matrix given in Equation 6.3. Now transform coordinates from the original x as follows

$$\begin{Bmatrix} \hat{x}_B \\ \overline{x}_B \\ \hat{x}_S \\ \overline{x}_S \end{Bmatrix} = \underbrace{\begin{bmatrix} [I] & 0 & 0 & 0 \\ 0 & [I] & 0 & 0 \\ 0 & 0 & [I] & [T_c] \\ 0 & 0 & 0 & [I] \end{bmatrix}}_{\equiv[T1]} \begin{Bmatrix} \hat{x}_B \\ \overline{x}_B \\ \hat{x}_R \\ \overline{x}_S \end{Bmatrix} \tag{6.10}$$

Enforcing the compatibility $\{\overline{x}_B\} = \{\overline{x}_S\}$ at the interface DOF's results in the transformation

$$\begin{Bmatrix} \hat{x}_B \\ \overline{x}_B \\ \hat{x}_R \\ \overline{x}_S \end{Bmatrix} = \underbrace{\begin{bmatrix} [I] & 0 & 0 \\ 0 & [I] & 0 \\ 0 & 0 & [I] \\ 0 & [I] & 0 \end{bmatrix}}_{\equiv[T2]} \begin{Bmatrix} \hat{x}_B \\ \overline{x}_B \\ \hat{x}_R \end{Bmatrix} \tag{6.11}$$

The modes obtained in Equation 6.7 and Equation 6.8 can be used to transform from physical to modal coordinates. For BV, this is defined by

$$\begin{Bmatrix} \hat{x}_B \\ \overline{x}_B \end{Bmatrix} = \begin{bmatrix} \hat{\phi} \\ \overline{\phi} \end{bmatrix}_{BL} \{q_B\} \tag{6.12}$$

while for SV, it is defined by

$$\{\hat{x}_R\} = \left[\hat{\phi}\right]_S \{q_S\} \tag{6.13}$$

These transformations can be conveniently written as

$$\begin{Bmatrix} \hat{x}_B \\ \overline{x}_B \\ \hat{x}_R \end{Bmatrix} = \underbrace{\begin{bmatrix} \begin{bmatrix} \hat{\phi} \\ \overline{\phi} \end{bmatrix}_{BL} & 0 \\ 0 & \left[\hat{\phi}\right]_S \end{bmatrix}}_{\equiv[T3]} \begin{Bmatrix} q_B \\ q_S \end{Bmatrix} \tag{6.14}$$

Combining the three transformations leads to

$$\begin{Bmatrix} \hat{x}_B \\ \overline{x}_B \\ \hat{x}_S \\ \overline{x}_S \end{Bmatrix} = \underbrace{\begin{bmatrix} \begin{bmatrix} \hat{\phi} \\ \overline{\phi} \end{bmatrix}_{BL} & 0 \\ [T_c]\left[\overline{\phi}\right]_{BL} & \left[\hat{\phi}\right]_S \\ \left[\overline{\phi}\right]_{BL} & 0 \end{bmatrix}}_{=[T1][T2][T3]\equiv[T]=\text{coupling transf.}} \begin{Bmatrix} q_B \\ q_S \end{Bmatrix} \tag{6.15}$$

which gives the displacements, x, of the coupled system in terms of the generalized coordinates, q, via the interface-loaded modes of BV, the fixed-interface modes of SV, and the constraint modes of SV.

By making the substitution $x = Tq$ into Equation 6.1 and then premultiplying by T^T,

the result is

$$(T^T M T)\ddot{x} + (T^T K T)x = T^T F \tag{6.16}$$

or

$$M^*\ddot{q} + K^* q = F^* \tag{6.17}$$

where M^* is the system modal mass, K^* is the system modal stiffness, and F^* is the system modal force. The coupled system modes, Φ, and frequencies, Ω^2, are obtained from the eigenvalue problem

$$\left(-\Omega_i^2 M^* + K^*\right)\Phi_i = 0 \tag{6.18}$$

These modes can be expressed back in physical coordinates by using $\Psi = T\Phi$, where Ψ is the physical modal matrix.

The composition of M^* and K^* can now be investigated. Look at M^* first, which is calculated from $M^* = T^T M T$. This triple product leads to $M^* =$

$$\left[\begin{array}{c|c} \begin{bmatrix}\hat{\phi}\\ \overline{\phi}\end{bmatrix}_{BL}^T [M_B] \begin{bmatrix}\hat{\phi}\\ \overline{\phi}\end{bmatrix}_{BL} + \begin{bmatrix}[T_c]\left[\overline{\phi}\right]_{BL}\\ \left[\overline{\phi}\right]_{BL}\end{bmatrix}^T [M_S] \begin{bmatrix}[T_c]\left[\overline{\phi}\right]_{BL}\\ \left[\overline{\phi}\right]_{BL}\end{bmatrix} & \begin{bmatrix}[T_c]\left[\overline{\phi}\right]_{BL}\\ \left[\overline{\phi}\right]_{BL}\end{bmatrix}^T [M_S] \begin{bmatrix}\left[\hat{\phi}\right]_S\\ 0\end{bmatrix} \\ \hline \begin{bmatrix}\left[\hat{\phi}\right]_S\\ 0\end{bmatrix}^T [M_S] \begin{bmatrix}[T_c]\left[\overline{\phi}\right]_{BL}\\ \left[\overline{\phi}\right]_{BL}\end{bmatrix} & \begin{bmatrix}\left[\hat{\phi}\right]_S\\ 0\end{bmatrix}^T [M_S] \begin{bmatrix}\left[\hat{\phi}\right]_S\\ 0\end{bmatrix} \end{array}\right] \tag{6.19}$$

Consider the upper-left term, and notice that it can be rewritten as

$$\begin{bmatrix}\hat{\phi}\\ \overline{\phi}\end{bmatrix}_{BL}^T [M_B] \begin{bmatrix}\hat{\phi}\\ \overline{\phi}\end{bmatrix}_{BL} + \begin{bmatrix}\hat{\phi}\\ \overline{\phi}\end{bmatrix}_{BL}^T \left[\begin{array}{c|c} 0 & 0 \\ \hline 0 & \underbrace{\begin{bmatrix}[T_c]\\ [I]\end{bmatrix}^T [M_S] \begin{bmatrix}[T_c]\\ [I]\end{bmatrix}}_{=\overline{M}_S \text{ (see Equation 6.5)}} \end{array}\right] \begin{bmatrix}\hat{\phi}\\ \overline{\phi}\end{bmatrix}_{BL}$$

$$= \begin{bmatrix}\hat{\phi}\\ \overline{\phi}\end{bmatrix}_{BL}^T \begin{bmatrix}(M_{NN})_B & (M_{NI})_B\\ (M_{IN})_B & (M_{II})_B + \overline{M}_S\end{bmatrix} \begin{bmatrix}\hat{\phi}\\ \overline{\phi}\end{bmatrix}_{BL} = [I] \tag{6.20}$$

This assumes that the interface-loaded modes from Equation 6.7 are mass normalized. The

lower-right term leads to a similar simplification

$$\begin{bmatrix} \left[\hat{\phi}\right]_S \\ 0 \end{bmatrix}^T [M_S] \begin{bmatrix} \left[\hat{\phi}\right]_S \\ 0 \end{bmatrix} = \left[\hat{\phi}\right]_S^T [(M_{NN})_S] \left[\hat{\phi}\right]_S = [I] \tag{6.21}$$

likewise assuming mass-normalized, fixed-interface modes from Equation 6.8. The upper-right term, however, can only be reduced to

$$\begin{bmatrix} [T_c]\left[\overline{\phi}\right]_{BL} \\ \left[\overline{\phi}\right]_{BL} \end{bmatrix}^T [M_S] \begin{bmatrix} \left[\hat{\phi}\right]_S \\ 0 \end{bmatrix} = \left[\overline{\phi}\right]_{BL}^T [T_c]^T [(M_{NN})_S] \left[\hat{\phi}\right]_S + \left[\overline{\phi}\right]_{BL}^T [(M_{IN})_S] \left[\hat{\phi}\right]_S$$

$$= \left[\overline{\phi}\right]_{BL}^T \left([T_c]^T [(M_{NN})_S] + [(M_{IN})_S] \right) \left[\hat{\phi}\right]_S = [\alpha] \tag{6.22}$$

and due to symmetry, the lower-left term is $[\alpha]^T$. Thus,

$$M^* = \begin{bmatrix} [I] & [\alpha] \\ [\alpha]^T & [I] \end{bmatrix} \tag{6.23}$$

K^*, on the other hand, can be simplified to a diagonal matrix as follows. Replacing all of the M's with K's in Equation 6.19 results in an upper-left term of

$$\begin{bmatrix} \hat{\phi} \\ \overline{\phi} \end{bmatrix}_{BL}^T \begin{bmatrix} (K_{NN})_B & (K_{NI})_B \\ (K_{IN})_B & (K_{II})_B + \overline{K}_S \end{bmatrix} \begin{bmatrix} \hat{\phi} \\ \overline{\phi} \end{bmatrix}_{BL} = \begin{bmatrix} \ddots & & \\ & \omega^2 & \\ & & \ddots \end{bmatrix}_{BL} \tag{6.24}$$

Similarly, the lower-right term becomes

$$\begin{bmatrix} \left[\hat{\phi}\right]_S \\ 0 \end{bmatrix}^T [K_S] \begin{bmatrix} \left[\hat{\phi}\right]_S \\ 0 \end{bmatrix} = \left[\hat{\phi}\right]_S^T [(K_{NN})_S] \left[\hat{\phi}\right]_S = \begin{bmatrix} \ddots & & \\ & \omega^2 & \\ & & \ddots \end{bmatrix}_S \tag{6.25}$$

The upper-right term is

$$\left[\overline{\phi}\right]_{BL}^T [T_c]^T [(K_{NN})_S] \left[\hat{\phi}\right]_S + \left[\overline{\phi}\right]_{BL}^T [(K_{IN})_S] \left[\hat{\phi}\right]_S$$

$$= \left[\overline{\phi}\right]_{BL}^T \left([T_c]^T [(K_{NN})_S] + [(K_{IN})_S] \right) \left[\hat{\phi}\right]_S \tag{6.26}$$

but since $[T_c] = -[(K_{NN})_S^{-1}][(K_{NI})_S]$, the term can further simplified to

$$\begin{aligned}
&\left[\overline{\phi}\right]_{BL}^T \left(-[(K_{NI})_S]^T[(K_{NN})_S]^{-T}[(K_{NN})_S] + [(K_{IN})_S]\right) \left[\hat{\phi}\right]_S \\
&= \left[\overline{\phi}\right]_{BL}^T (-[(K_{IN})_S][I] + [(K_{IN})_S]) \left[\hat{\phi}\right]_S \\
&= \left[\overline{\phi}\right]_{BL}^T \underbrace{(-[(K_{IN})_S] + [(K_{IN})_S])}_{=0} \left[\hat{\phi}\right]_S = 0
\end{aligned} \tag{6.27}$$

This also holds for the lower-left term. Consequently, K^* becomes

$$K^* = \begin{bmatrix} \begin{bmatrix} \ddots & & \\ & \omega^2 & \\ & & \ddots \end{bmatrix}_{BL} & 0 \\ 0 & \begin{bmatrix} \ddots & & \\ & \omega^2 & \\ & & \ddots \end{bmatrix}_S \end{bmatrix} \tag{6.28}$$

Usually only a truncated number of substructure modes and frequencies are used. If n_{BL} equals the number of kept BV interface-loaded modes, and n_S equals the number of kept SV cantilever modes, then both M^* and K^* will be of size $(n_{BL}+n_S)\times(n_{BL}+n_S)$. These forms of M^* and K^* can then be used to determine Φ, which will also be of order $(n_{BL} + n_S)$. It should be stressed that the simplified forms of M^* and K^* given in Equations 6.23 and 6.28 are a direct result of using interface-loaded modes. If for some reason these modes are not used, then the more general expressions for M^* and K^* will be required.

All of the above steps have permitted the coupled system modes to be predicted. These real, normal modes are obtained by considering the ideal, undamped system. The next chapter will deal with predicting the damped properties of the system by a variety of formulations.

6.2 Implementation of Method

The Component Mode Substitution Method outlined above was implemented by a FORTRAN subroutine that was written specifically for this task. The subroutine made use of

MATRIX, a computer program developed by the Aerospace Corporation to perform matrix manipulations, linear algebra operations, and a number of other functions. MATRIX consists of dozens of routines that can be called to operate on the desired matrices. Each matrix is stored as a two-dimensional array in a dataset and is assigned to a FORTRAN unit. As an example, the line of code

```
CALL TRANSP(20,21)
```

sends the matrix placed on unit 20 to the MATRIX routine called TRANSP (which takes the transpose of a matrix), and then places the result on unit 21.

The coupling routine code is given in Appendix B.1. It first reads the mass and stiffness matrices of the updated finite element models of BV and SV. Depending on whether the desired modes are either of the system with or without the added damping, the corresponding model of BV is chosen. The stiffness matrix K_S is then partitioned and the required submatrices are used to compute the constraint mode matrix T_c according to Equation 6.3. The reduced-interface matrices of SV are determined and then overloaded onto the mass and stiffness matrices of BV. The MATRIX eigensolver routine DEVEC is called to compute the interface-loaded modes and frequencies of BV by solving Equation 6.7. DEVEC takes a mass and stiffness matrix as input and returns the corresponding eigenvalues (frequencies squared) and eigenvectors (mode shapes). In a similar manner, the fixed-interface modes of SV follow from Equation 6.8. A truncated set of modes is chosen and used to create M^* and K^* by taking advantage of the simplified forms of Equations 6.23 and 6.28. DEVEC is called again to determine the system frequencies and modes (in generalized coordinates). These modes are then transformed to physical coordinates and the rows (DOF's) are reordered so as to match the DOF ordering of the measured modes. A comparison is made between the predicted and measured system modes by performing a cross-orthogonality check and computing the percent errors of the predicted modal frequencies. The results are presented in the following section.

6.3 Comparison of Predicted and Measured System Modes

The primary means of comparison, as stated previously, are the cross-orthogonality check of the mode shapes and the percent errors of the modal frequencies. Let Ψ_m be the measured mode shapes, Ψ_a be the analytically predicted mode shapes, and M_a be the

analytical mass matrix. Then the cross-orthogonality check is defined as $\Psi_a^T M_a \Psi_m$, while the percent error for the i th modal frequency is given by $\frac{f_a^{(i)} - f_m^{(i)}}{f_m^{(i)}} \times 100\%$. Table 6.1 shows the check for the no-added damping situation, and Table 6.2 shows the check for the case of added damping. (To keep a reasonable width for the table, only the element magnitudes are given.) The frequency errors are presented in Table 6.3. The two antenna torsion modes were not included in the cross-orthogonality checks since their mode shapes were not extracted. Thus, the same twelve modes are compared in all of the tables.

Table 6.1: Cross-orthogonality Check for System Without Added Damping

1.00	0.00	0.00	0.01	0.00	0.00	0.00	0.00	0.00	0.00	0.00	0.00
0.00	**1.00**	0.00	0.00	0.00	0.00	0.00	0.01	0.00	0.00	0.00	0.00
0.00	0.00	**1.00**	0.00	0.00	0.00	0.00	0.00	0.00	0.00	0.00	0.00
0.01	0.00	0.00	**1.00**	0.01	0.02	0.00	0.00	0.00	0.00	0.00	0.00
0.00	0.00	0.00	0.01	**1.00**	0.02	0.00	0.00	0.00	0.00	0.04	0.01
0.00	0.00	0.00	0.02	0.00	**1.00**	0.00	0.00	0.00	0.01	0.01	0.01
0.00	0.00	0.00	0.00	0.00	0.00	**1.00**	0.00	0.02	0.00	0.00	0.00
0.00	0.01	0.00	0.00	0.00	0.00	0.00	**1.00**	0.00	0.03	0.00	0.00
0.00	0.00	0.00	0.00	0.00	0.00	0.02	0.00	**1.00**	0.00	0.00	0.00
0.00	0.00	0.00	0.00	0.00	0.00	0.00	0.03	0.00	**1.00**	0.03	0.01
0.00	0.00	0.00	0.00	0.03	0.00	0.00	0.00	0.00	0.03	**0.99**	**0.06**
0.00	0.00	0.00	0.00	0.00	0.01	0.00	0.00	0.00	0.00	**0.05**	**1.00**

Table 6.2: Cross-orthogonality Check for System With Added Damping

1.00	0.00	0.00	0.00	0.00	0.00	0.01	0.01	0.00	0.00	0.00	0.00
0.00	**1.00**	0.00	0.00	0.00	0.00	0.00	0.01	0.00	0.00	0.00	0.00
0.00	0.00	**1.00**	0.00	0.00	0.00	0.00	0.00	0.00	0.00	0.00	0.00
0.00	0.00	0.00	**1.00**	0.01	0.02	0.00	0.00	0.00	0.00	0.00	0.00
0.00	0.00	0.00	0.01	**1.00**	0.02	0.00	0.00	0.00	0.00	0.04	0.01
0.00	0.00	0.00	0.02	0.00	**1.00**	0.00	0.00	0.00	0.01	0.00	0.01
0.01	0.00	0.00	0.00	0.00	0.00	**1.00**	0.00	0.02	0.00	0.00	0.00
0.02	0.00	0.00	0.00	0.00	0.00	0.00	**1.00**	0.00	0.03	0.03	0.03
0.00	0.00	0.00	0.00	0.00	0.00	0.02	0.00	**1.00**	0.00	0.00	0.00
0.00	0.00	0.00	0.00	0.00	0.00	0.00	0.03	0.00	**1.00**	0.02	0.01
0.00	0.00	0.00	0.00	0.03	0.00	0.00	0.03	0.00	0.02	**0.99**	**0.06**
0.00	0.00	0.00	0.00	0.00	0.01	0.00	0.03	0.00	0.00	**0.05**	**1.00**

The cross-orthogonality checks show that the measured and predicted system modes

Table 6.3: Percent Errors Between Predicted and Measured System Frequencies

Mode	% Error	
#	No Added Damping	Added Damping
1	0.45	1.06
2	−1.30	−1.28
3	−2.41	−2.30
4	−0.31	−0.36
5	0.32	0.34
6	1.81	1.88
7	−0.18	−0.39
8	1.09	1.20
9	−0.10	−0.12
10	−3.08	−3.00
11	−1.44	−1.53
12	−1.25	−1.36
Avg. magnitude % error	1.15	1.24
Standard deviation	0.94	0.87

compare extremely well. When the terms are rounded to two decimal places, all the diagonal terms except one round to 1.00. The largest off-diagonal term is only 0.06, which is consistent with with the errors in the updated substructure models found in Tables 5.2, 5.3, and 5.4. Consequently, the coupling procedure was able to maintain the accuracy of the substructure mode shapes. The errors in frequency are generally good, and only in one case does the error reach above a magnitude of 3%. The larger errors tend to occur in the antenna modes and the out-of-plane bending modes.

These results for both cases show that the Component Mode Substitution Method does yield accurate results. This experimental verification is an important by-product of this project. The results of the main focus of the project, which is the analysis of various damping formulations, are contained in the following chapter.

Chapter 7

Damping Formulations

The Component Mode Substitution Method presented in the last chapter provided a means to predict the undamped mode shapes and natural frequencies associated with the coupled system. There is also a need to approximate the damping properties of the system using information from the substructures. This chapter looks at three distinct methods that attempt to generate a system modal damping matrix from substructure test results. These techniques all utilize the modal damping ratios of the substructure modes, as well as something referred to as the mode participation matrix. The first approach is a straightforward triple matrix product, while the other two are based on a normalized mass fraction approach and a strain energy fraction approach, respectively. These methods are discussed, and the resulting system damping ratios are then presented.

7.1 Triple Matrix Product

The equations of motion of the uncoupled components given by Equation 6.1 can be modified to include damping as follows

$$M\ddot{x} + C\dot{x} + Kx = F \tag{7.1}$$

where

$$C = \begin{bmatrix} [C_B] & 0 \\ 0 & [C_S] \end{bmatrix}$$

Introducing the coordinate transformation $x = Tq$, which employs the coupling transformation, T, defined in Equation 6.15, leads to

$$M^*\ddot{q} + C^*\dot{q} + K^*q = F^* \tag{7.2}$$

In the case of proportional damping, C^* can be shown to be of the form

$$C^* = \begin{bmatrix} \begin{bmatrix} \ddots & & \\ & 2\zeta\omega & \\ & & \ddots \end{bmatrix}_{BL} & [\beta] \\ [\beta]^T & \begin{bmatrix} \ddots & & \\ & 2\zeta\omega & \\ & & \ddots \end{bmatrix}_{S} \end{bmatrix} \tag{7.3}$$

where $[\beta]$ is, in general, fully populated. Non-proportional damping will result in C^* being entirely full. Typically, T^TCT is not directly computed since C is not known. At this point, the usual simplification that is made is to ignore the off-diagonal terms and to generate an approximate C^* using the appropriate substructure modal damping ratios and natural frequencies

$$C^* = \begin{bmatrix} \begin{bmatrix} \ddots & & \\ & 2\zeta\omega & \\ & & \ddots \end{bmatrix}_{BL} & 0 \\ 0 & \begin{bmatrix} \ddots & & \\ & 2\zeta\omega & \\ & & \ddots \end{bmatrix}_{S} \end{bmatrix} \tag{7.4}$$

where the ζ_{BL}'s are the damping ratios obtained during the tests on BV with interface mass loading, and the ω_{BL}'s are the corresponding analytical frequencies from the interface-loaded BV model. The ζ_S's and ω_S's are the actual measured values of the fixed-interface SV modes.

The matrices K^* and M^* yield the coupled system modes Φ. This modal matrix is often called the "modes of modes" or the mode participation matrix. Each column is related to a system mode, while each row is related to a substructure mode. By comparing the magnitudes of the elements in a column, a sense can be gained of the relative participation of the substructure modes in that particular system mode. For instance, if one element is much larger than the remaining elements in the column, then the system mode is composed mainly of that one substructure mode.

Performing the coordinate transformation $q = \Phi\eta$ yields

$$I\ddot{\eta} + \Gamma\dot{\eta} + \Omega^2\eta = \Phi^T F^* \tag{7.5}$$

where Γ is the system modal damping matrix that is desired. Γ is calculated from the triple matrix product $\Phi^T C^* \Phi$, which gives this method its name. Γ will contain off-diagonal terms, and this couples the equations since both I and Ω^2 are diagonal. For simplicity, these terms are often neglected, leaving a diagonal Γ as well. The use of both the fully populated Γ from the triple matrix product (TMP) and a diagonal Γ from the diagonal part of the TMP was studied in a series of transient response tests to determine the validity of the approximations. The remaining two approaches are alternate means of creating a diagonal system modal damping matrix.

7.2 Normalized Mass Fraction

The next method determines the modal damping of each system mode based on a weighted average of the modal damping of the substructure modes. The weighting accounts for the participation of the substructure modes in the generalized system mass. The system modes, Φ, are normalized to produce unity modal system mass in Equation 7.5. The triple product $\Phi^T M^* \Phi = I$ can be partitioned according to substructures as

$$\begin{bmatrix} \Phi_B \\ \Phi_S \end{bmatrix}^T \begin{bmatrix} M^*_{BB} & M^*_{BS} \\ M^*_{SB} & M^*_{SS} \end{bmatrix} \begin{bmatrix} \Phi_B \\ \Phi_S \end{bmatrix} = I \tag{7.6}$$

which when expanded leads to

$$\underbrace{[\Phi_B]^T [M^*_{BB}\Phi_B + M^*_{BS}\Phi_S]}_{\text{BV mass participation}} + \underbrace{[\Phi_S]^T [M^*_{SB}\Phi_B + M^*_{SS}\Phi_S]}_{\text{SV mass participation}} = I \tag{7.7}$$

The system modal damping Γ is assumed to be diagonal (i.e., $\Gamma_{ii} = 2\zeta_i\Omega_i$, where for the ith system mode, ζ_i is the damping ratio and Ω_i is the circular natural frequency). Γ can be thought of as the sum of two parts, namely the component due to BV and the component due to SV. This can be expressed as

$$\Gamma = \begin{bmatrix} \ddots & & \\ & 2\zeta\Omega & \\ & & \ddots \end{bmatrix} = \Gamma_B + \Gamma_S \tag{7.8}$$

The contribution to system damping from BV is approximated as the modal damping of

BV weighted by the mass participation of BV. Written out, this takes the form

$$\Gamma_B = [\Phi_B]^T \left[\begin{array}{c} \ddots \\ & 2\zeta\omega \\ & & \ddots \end{array} \right]_{BL} [M^*_{BB}\Phi_B + M^*_{BS}\Phi_S] \tag{7.9}$$

Similarly, the contribution from SV is

$$\Gamma_S = [\Phi_S]^T \left[\begin{array}{c} \ddots \\ & 2\zeta\omega \\ & & \ddots \end{array} \right]_{S} [M^*_{SB}\Phi_B + M^*_{SS}\Phi_S] \tag{7.10}$$

Placing the expressions for Γ_B and Γ_S into Equation 7.8 results in

$$\begin{aligned} \Gamma = \left[\begin{array}{c} \ddots \\ & 2\zeta\Omega \\ & & \ddots \end{array} \right] &= [\Phi_B]^T \left[\begin{array}{c} \ddots \\ & 2\zeta\omega \\ & & \ddots \end{array} \right]_{BL} [M^*_{BB}\Phi_B + M^*_{BS}\Phi_S] \\ &+ [\Phi_S]^T \left[\begin{array}{c} \ddots \\ & 2\zeta\omega \\ & & \ddots \end{array} \right]_{S} [M^*_{SB}\Phi_B + M^*_{SS}\Phi_S] \end{aligned} \tag{7.11}$$

The right-hand side of the equation will create a matrix that is not diagonal, so the equality holds only if the off-diagonal terms are set to zero.

7.3 Strain Energy Fraction

The final method is similar to the normalized mass fraction approach, but the strain energy participation of the substructure modes in the system modes is used in the weighting. Replacing M^* with K^* in Equation 7.6 and making use of the special form of K^* obtained from Component Mode Substitution (Equation 6.28) leads to

$$\left[\begin{array}{c} \Phi_B \\ \Phi_S \end{array} \right]^T \left[\begin{array}{cc} \left[\begin{array}{c} \ddots \\ & \omega^2_{BL} \\ & & \ddots \end{array} \right] & 0 \\ 0 & \left[\begin{array}{c} \ddots \\ & \omega^2_{S} \\ & & \ddots \end{array} \right] \end{array} \right] \left[\begin{array}{c} \Phi_B \\ \Phi_S \end{array} \right] = \Omega^2 \tag{7.12}$$

and Equation 7.7 becomes

$$\underbrace{[\Phi_B]^T \left[\begin{array}{c} \ddots \\ & \omega^2_{BL} \\ & & \ddots \end{array} \right] [\Phi_B]}_{\text{BV strain energy participation}} + \underbrace{[\Phi_S]^T \left[\begin{array}{c} \ddots \\ & \omega^2_{S} \\ & & \ddots \end{array} \right] [\Phi_S]}_{\text{SV strain energy participation}} = \Omega^2 \tag{7.13}$$

(Note that in order for the last equation to be consistent with the definition of strain energy, factors of $\frac{1}{2}$ should precede each term. For simplicity, these factors were canceled from the equation.)

This time express the system damping ratios ζ as the sum of the substructure contributions ζ_B and ζ_S. Weight the substructure damping ratios by the corresponding strain energy participation as follows.

$$\zeta_B = [\Phi_B]^T \begin{bmatrix} \ddots & & \\ & \zeta & \\ & & \ddots \end{bmatrix}_{BL} \begin{bmatrix} \ddots & & \\ & \omega_{BL}^2 & \\ & & \ddots \end{bmatrix} [\Phi_B] \begin{bmatrix} \ddots & & \\ & \Omega^{-2} & \\ & & \ddots \end{bmatrix} \tag{7.14}$$

Likewise for the SV contribution,

$$\zeta_S = [\Phi_S]^T \begin{bmatrix} \ddots & & \\ & \zeta & \\ & & \ddots \end{bmatrix}_{S} \begin{bmatrix} \ddots & & \\ & \omega_S^2 & \\ & & \ddots \end{bmatrix} [\Phi_S] \begin{bmatrix} \ddots & & \\ & \Omega^{-2} & \\ & & \ddots \end{bmatrix} \tag{7.15}$$

The system modal damping is

$$\begin{aligned} \Gamma = \begin{bmatrix} \ddots & & \\ & 2\zeta\Omega & \\ & & \ddots \end{bmatrix} &= [\Phi_B]^T \begin{bmatrix} \ddots & & \\ & 2\zeta\omega^2 & \\ & & \ddots \end{bmatrix}_{BL} [\Phi_B] \begin{bmatrix} \ddots & & \\ & \Omega^{-1} & \\ & & \ddots \end{bmatrix} \\ &+ [\Phi_S]^T \begin{bmatrix} \ddots & & \\ & 2\zeta\omega^2 & \\ & & \ddots \end{bmatrix}_{S} [\Phi_S] \begin{bmatrix} \ddots & & \\ & \Omega^{-1} & \\ & & \ddots \end{bmatrix} \end{aligned} \tag{7.16}$$

As before, the off-diagonal elements that result in the right-hand side of the equation are set to zero.

7.4 Results

Since there were a total of twelve system modes under consideration, Γ was of size 12×12 for all damping formulations. The TMP method was implemented within the coupling program found in Appendix B.1. Instead of showing the actual Γ that was computed, the coupling index matrix, α, defined by Equation 1.9 will be presented in order to gain a sense of the relative sizes of the off-diagonal elements compared to the diagonal elements. Table 7.1 shows α for the case of no added damping in the system, while Table 7.2 shows the matrix when added damping was present. Only terms greater than 0.10 are given, and the largest off-diagonal elements are underlined. As expected, the case with added

Table 7.1: Coupling Index Matrix for TMP Γ of System Without Added Damping

1.00	–	**0.20**	**0.16**	–	–	**0.22**	–	**0.21**	–	–	–
–	**1.00**	–	–	–	–	–	–	–	–	–	–
0.20	–	**1.00**	–	–	–	**0.13**	–	**0.14**	–	–	–
0.16	–	–	**1.00**	–	–	**0.20**	–	**0.20**	–	–	–
–	–	–	–	**1.00**	–	–	–	–	–	–	–
–	–	–	–	–	**1.00**	–	–	–	–	–	–
0.22	–	**0.13**	**0.20**	–	–	**1.00**	–	**0.44**	–	–	–
–	–	–	–	–	–	–	**1.00**	–	–	–	–
0.21	–	**0.14**	**0.20**	–	–	**0.44**	–	**1.00**	–	–	–
–	–	–	–	–	–	–	–	–	**1.00**	–	–
–	–	–	–	–	–	–	–	–	–	**1.00**	–
–	–	–	–	–	–	–	–	–	–	–	**1.00**

Table 7.2: Coupling Index Matrix for TMP Γ of System With Added Damping

1.00	**0.17**	**0.51**	**0.11**	–	–	**0.26**	–	**0.23**	–	–	–
0.17	**1.00**	–	–	–	–	–	–	–	–	–	–
0.51	–	**1.00**	**0.14**	–	–	**0.13**	–	**0.12**	–	–	–
0.11	–	**0.14**	**1.00**	–	–	**0.48**	–	**0.36**	–	–	–
–	–	–	–	**1.00**	–	–	–	–	–	**0.17**	–
–	–	–	–	–	**1.00**	–	–	–	**0.27**	–	**0.10**
0.26	–	**0.12**	**0.48**	–	–	**1.00**	–	–	–	–	–
–	–	–	–	–	–	–	**1.00**	–	–	–	–
0.23	–	**0.12**	**0.36**	–	–	–	–	**1.00**	–	–	–
–	–	–	–	–	**0.27**	–	–	–	**1.00**	–	–
–	–	–	–	**0.17**	–	–	–	–	–	**1.00**	–
–	–	–	–	–	**0.10**	–	–	–	–	–	**1.00**

damping has more terms, and it has the largest coupling value of 0.51. It is interesting that even when there is no additional damping in the system, there still exist fairly large coupling indices. The maximum value of 0.44 was not expected at all. It occurs between modes 7 and 9, which are both x-bending modes. In fact, all of the off-diagonal terms shown for the no added damping case are based on modes that are characterized by x motion. With the added damping, more terms appear that relate the other two types of modes, but never does a coupling term appear between modes of different types (like, for example, between a torsion mode and a z-bending mode). Also note that the $(9,7)$ element disappears in Table 7.2. This peculiarity, along with the presence of the 0.44 term, could not be explained.

The implementation of the diagonal damping methods was performed via a FORTRAN program that was written, and excerpts from it can be found in Appendix B.2. The methods can be compared by looking at the damping ratios that are predicted for each system mode. Γ in these cases is assumed to be of the form $\Gamma_{ii} = 2\zeta_i\Omega_i$, so by dividing by $2\Omega_i$, the ζ_i's can be obtained for the different methods. The values are given in Table 7.3 and Table 7.4 for the two different damping situations. In addition, the measured value of ζ for each system mode is shown. The average damping value is computed for the different methods, and in both cases, the average of the predictions is higher than the measured average. Although the three damping formulations differ significantly in a few of the modes (particularly in the damped case), the overall averages agree quite well. This seems to indicate that the three methods, in a sense, "conserve" damping for the entire system.

Table 7.3: Predicted and Measured System ζ's (No Added Damping Case; Proportional Damping Assumed)

	ζ (%)			
Mode #	Measured	Diagonal TMP	Strain energy fraction	Normalized mass fraction
1	0.50	0.43	0.45	0.49
2	0.17	0.26	0.26	0.26
3	0.20	0.30	0.28	0.27
4	0.19	0.18	0.19	0.21
5	0.21	0.16	0.17	0.20
6	0.16	0.11	0.11	0.13
7	0.13	0.28	0.22	0.19
8	0.09	0.07	0.08	0.08
9	0.11	0.29	0.21	0.16
10	0.08	0.15	0.14	0.14
11	0.19	0.21	0.21	0.22
12	0.10	0.13	0.14	0.15
Avg.	0.18	0.21	0.21	0.21

Table 7.4: Predicted and Measured System ζ's (Added Damping Case; Proportional Damping Assumed)

	ζ (%)			
Mode #	Measured	Diagonal TMP	Strain energy fraction	Normalized mass fraction
1	1.27	1.37	1.43	1.49
2	0.17	0.27	0.27	0.26
3	0.30	0.40	0.36	0.33
4	1.57	1.52	1.61	1.72
5	0.30	0.29	0.31	0.34
6	0.35	0.32	0.34	0.36
7	1.04	1.07	0.89	0.81
8	0.09	0.07	0.08	0.08
9	0.30	1.16	0.91	0.76
10	0.09	0.17	0.15	0.15
11	0.27	0.26	0.26	0.27
12	0.30	0.34	0.36	0.39
Avg.	0.50	0.60	0.58	0.58

Chapter 8

Transient Response Testing

A series of transient response tests were performed on the coupled structure in order to investigate the different damping formulations. The results from the last chapter show that the diagonal damping methods produced, on the average, similar results for the damping ratios of the system modes. There were some discrepancies in a few modes, and one goal of the transient tests was to determine how significant these differences would be in response predictions that used the various modal damping matrices. Another objective of equal importance was to examine the effect of retaining the off-diagonal terms in the TMP. The coupling index matrices for both damping cases revealed fairly large off-diagonal terms, and it was important to see if the information contained in these terms would lead to better predictions. This chapter describes the tests that were conducted and the data that was measured. The analytical response prediction method is then discussed, and plots are shown that indicate how close the predictions for each damping formulation come to the measured responses. Finally, the results are quantified and used to compare the damping methods.

8.1 Procedure

The transient response tests were similar to the mode survey tests, and as a result, utilized most of the same equipment. A shaker was used to provide the external excitation, and accelerometers measured the responses. The acceleration time histories were desired, which meant that the process of computing FRF's was avoided. The shaker was driven by a band-limited, random signal of a fixed duration, and the responses were measured for the same amount of time. The applied force was also recorded since the response predictions

required a forcing function.

The source signal had a frequency content of 0–30 Hz, which avoided exciting the antenna torsion modes found around 40 Hz. The majority of the system modes, however, are below 30 Hz, including modes that have large coupling terms in the TMP damping matrix; consequently, nothing of significance was lost by restricting the excitation to this frequency range. The data collection occurred at a sampling rate of 2000 Hz and for a duration of 1.024 seconds. This provided more than enough resolution for the frequencies of interest since this resulted in a Δt of 0.0005 second. Not only were signals used that were on for the full acquisition period, but in some instances, the signal was turned off after half of this time period. The first signal type will be referred to as full random, and the second type will be referred to as burst random (50% length). Full random excitation leads to the forced response being dominant, while burst random permits the decay transient to be more readily observed. As a result, the effects of damping should also be more apparent in the burst random responses.

A total of eight separate tests were conducted on BVSV, and they are summarized in Table 8.1. Four tests were run on the original system, and they were then repeated when the damping treatment was added. The two types of source signal were implemented, and the shaker was moved between two locations, which are given in the table in terms of the DOF of the experimental model. The primary location was at a corner of SV in the x direction. The applied force would mainly excite the x-bending and torsion modes. The other location was in the center of the top floor of BV in the z direction, and it was meant to focus on the z-bending modes.

Table 8.1: Transient Response Tests

Test#	Added damping	Source signal	Shaker location
1	No	Full random	SV:7:$-x$
2	No	Full random	BV:21:$+z$
3	No	Burst random	SV:7:$-x$
4	No	Burst random	BV:21:$+z$
5	Yes	Full random	SV:7:$-x$
6	Yes	Full random	BV:21:$+z$
7	Yes	Burst random	SV:7:$-x$
8	Yes	Burst random	BV:21:$+z$

To reduce the amount of collected data, only a subset of the accelerometers from the mode survey tests was selected to provide the measurements. Ten accelerometers distributed throughout the structure were identified, and they are listed in Table 8.2. Each floor, as

Table 8.2: Accelerometer Locations Used for Response Measurements

Accelerometer #	DOF
1	SV:13:$+x$ *
1	SV:13:$+z$ ⋆
2	SV:7:$+z$
3	SV:8:$-x$
4	BV:20:$-z$
5	BV:17:$-x$
6	BV:16:$-z$
7	BV:14:$-x$
8	BV:10:$-z$
9	BV:5:$-x$

* used for tests with excitation in x

⋆ used for tests with excitation in z

well as the top antenna tip mass, contributed a pair of x and z sensors. The location of the force transducer coincided with the DOF at which the shaker was placed. The filter cutoff frequency for each channel was set at 30 Hz in order to reduce any high-frequency noise. Figure 8.1 shows one of the measured force time histories for a full random source signal, and Figure 8.2 shows one for a burst random source signal. Although the signal driving the shaker was turned off at $t \approx 0.5$ second in the second figure, the force transducer still read a reaction force as the structure dragged the shaker during the transient portion.

8.2 Response Prediction

For each test, analytical response predictions were made using the different modal damping matrices. These predictions are based on solving the system equations of motion in modal coordinates, which can be expressed as

$$I\ddot{\eta} + \Gamma\dot{\eta} + \Omega^2\eta = \Phi^T F^* \tag{8.1}$$

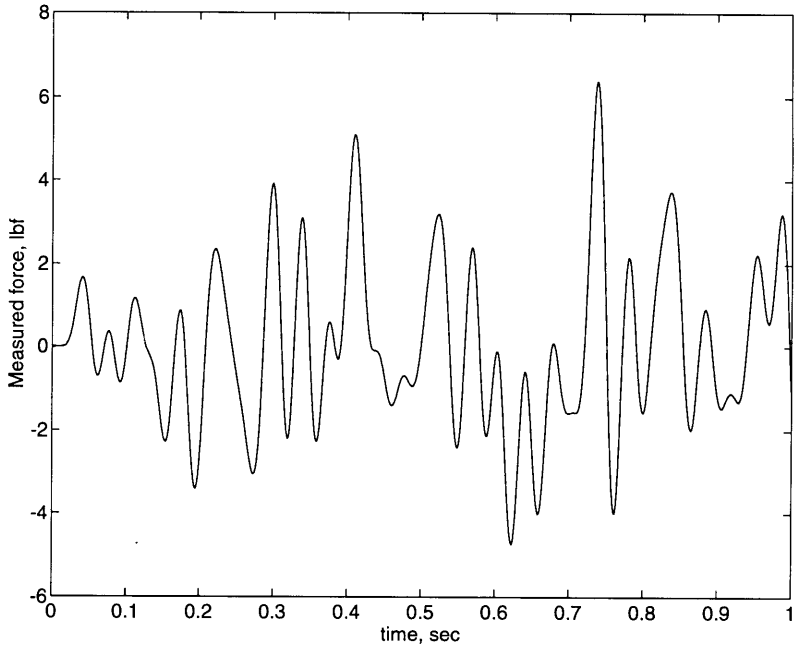

Figure 8.1: Measured force time history (full random).

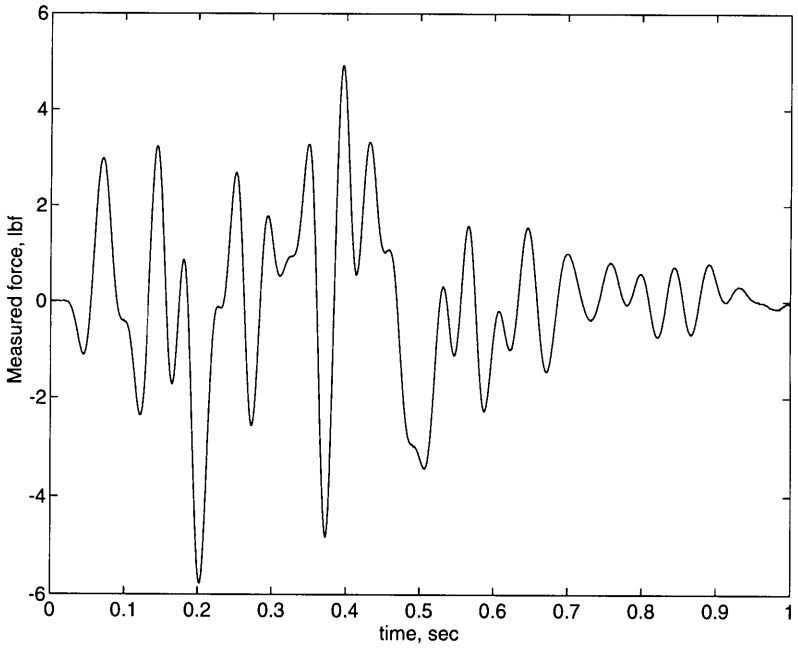

Figure 8.2: Measured force time history (burst random).

For a specified forcing function, F^*, numerical integration techniques can be employed to determine $\eta(t)$, and then the physical responses can be recovered by transforming back to physical coordinates. To isolate differences in the response that arise due to the use of various Γ's, both Ω^2 and Φ should remain the same as responses are computed for each damping formulation. As a result, it was decided to let Ω^2 be composed of the measured system natural frequencies and to let Φ be the analytical modal matrix obtained from Component Mode Substitution. The use of measured frequencies as opposed to the analytical frequencies would allow the predictions to remain close in phase to the measurements. This would permit a better comparison to be made between the two. Since the analytical mode shapes correlated extremely well with the measured mode shapes, the use of an analytical Φ was not seen as a problem.

The Transient Response Program (TRP) developed at The Aerospace Corporation was implemented in order to solve Equation 8.1. The inputs to the program include the system modal damping matrix, Γ, the system modal stiffness matrix, Ω^2, and the force transformation matrix, Φ_F. Φ_F consists of the columns of the transpose of the system modal matrix that correspond to the DOF's at which the forces are applied. In the case of the tests, only a single force was applied (and it coincided with one of the DOF's of the model); therefore, Φ_F was just a column vector. The forcing function F^* is stored in a form such that each record contains a time value, followed by the value(s) of the force(s) applied at that instant in time. Thus, each force is described by a discrete time-history. Because only one shaker was used, F^* was a scalar.

Times to begin and stop the integration are also specified as parameters for the program, along with the integration step size. The actual values used were $t_{\text{start}} = 0.0\,\text{s}$, $t_{\text{stop}} = 1.024\,\text{s}$, and $\Delta t = 0.0005\,\text{s}$. The equations are reduced to a system of first-order differential equations, and the integration is performed by a fourth-order Runge-Kutta method. The physical accelerations are computed at each time step by using an acceleration transformation matrix, T_A, such that $\ddot{x} = T_A\ddot{\eta}$. T_A consists of the rows of the modal matrix Φ that correspond to the DOF's at which the responses are sought. Since a total of nine accelerations were measured in each test, T_A was of size 9×12.

A series of eight plots are shown in Figures 8.3 to 8.6 to provide a visual indication of how the measured and predicted responses compared. They are grouped as follows

- System with no added damping
  - Figure 8.3(a): full random force in x, response in x
  - Figure 8.3(b): full random force in x, response in z
  - Figure 8.4(a): burst random force in x, response in x
  - Figure 8.4(b): burst random force in x, response in z
- System with added damping
  - Figure 8.5(a): full random force in x, response in x
  - Figure 8.5(b): full random force in x, response in z
  - Figure 8.6(a): burst random force in x, response in x
  - Figure 8.6(b): burst random force in x, response in z

A preliminary observation that can be made is that it is very difficult to discern five different responses in each plot. Usually, only two can be distinguished at a time. One is the measured response, and the other is a conglomerate of the predictions. This suggests that the predictions yield almost identical results. Another observation is that the predictions follow the measurements rather well, particularly in Figures 8.3 and 8.4.

The first signs of a breakdown in the predictions can be found in Figures 8.5(a) and 8.6(a). These plots correspond to x motion with added damping in the system, and the latter one represents motion of a point on the same floor as the damping treatment. At $t \approx 0.6$ s in this plot, the analytical responses no longer track the measurement, but at $t \approx 0.68$ s, they follow once again. Then from $t \approx 0.8$ s until the end of the acquisition period, the responses become out of phase, and it appears as if the measurement is responding at a slightly higher frequency than the predictions. One reason for this might be that the abrupt cutoff of the shaker source signal might have excited higher frequency modes above the 0–30 Hz content of the original random signal. Another explanation might be that the damping material itself is responding in a way that is not accounted for in the analytical model. To compare the predictions beyond a simple visual inspection, a more rigorous mathematical approach was undertaken, and the results can be found in the next section.

8.3 Comparison of Damping Formulations

As stated before, the responses of nine DOF's were measured in each of the eight tests. This produced a total of 72 measured time histories. Four separate damping formulations were used in the predictions of each measurement, which led to 288 analytical responses.

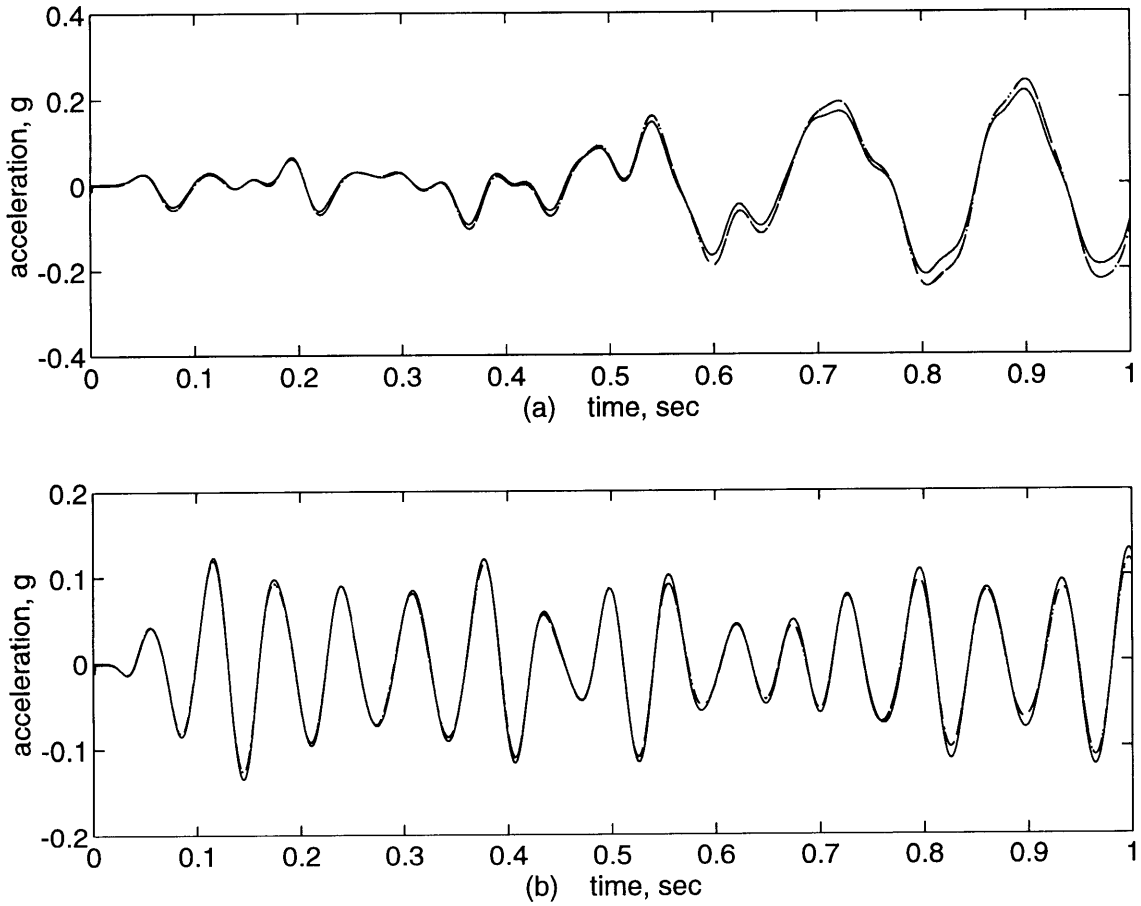

Figure 8.3: Response at (a) SV:13:+x, (b) SV:7:+z ; (—) measured, $(\cdots)$ full TMP, $(-\cdot)$ diagonal TMP, $(--)$ strain energy fraction, $(-\cdot\cdot)$ mass fraction.

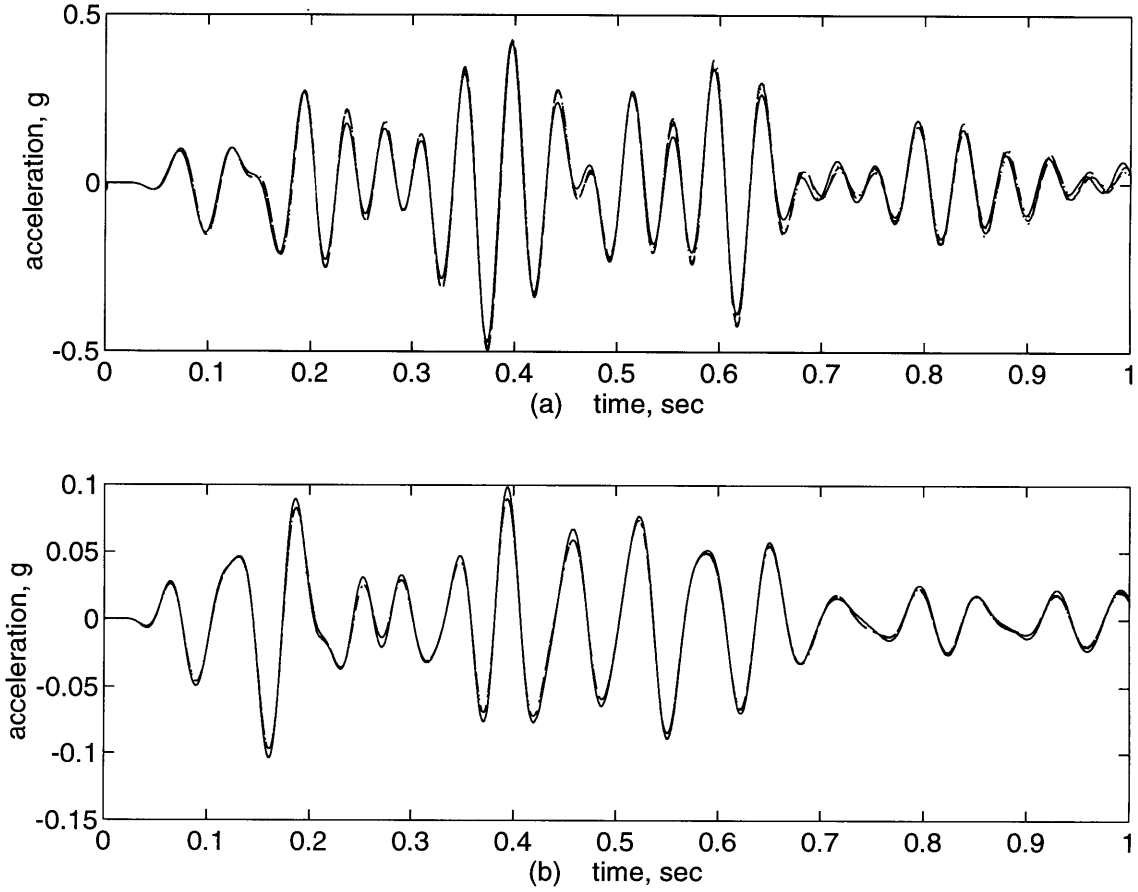

Figure 8.4: Response at (a) BV:17:+x, (b) BV:20:+z ; (—) measured, ($\cdots$) full TMP, ($-\cdot$) diagonal TMP, ($--$) strain energy fraction, ($-\cdot\cdot$) mass fraction.

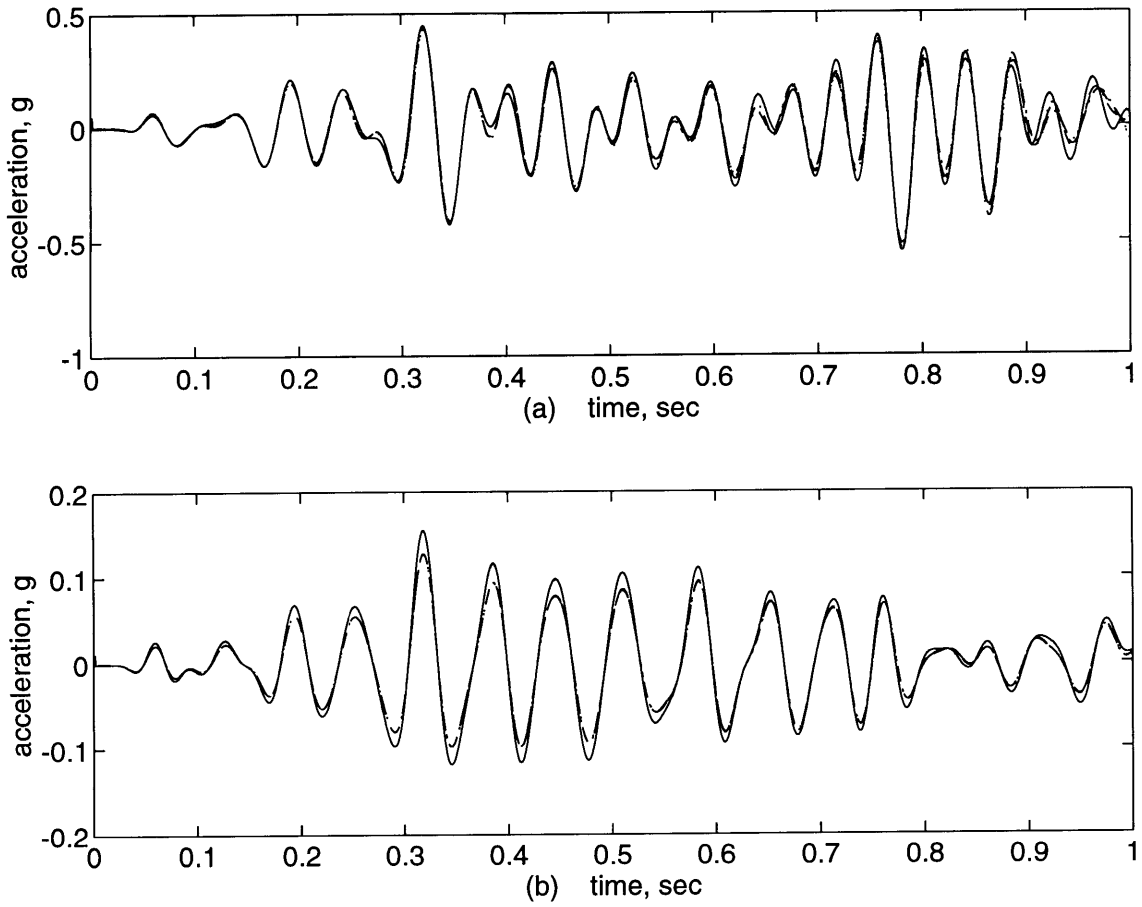

Figure 8.5: Response at (a) BV:14:+x, (b) BV:16:+z ; (—) measured, ($\cdots$) full TMP, ($-\cdot$) diagonal TMP, ($--$) strain energy fraction, ($-\cdot\cdot$) mass fraction.

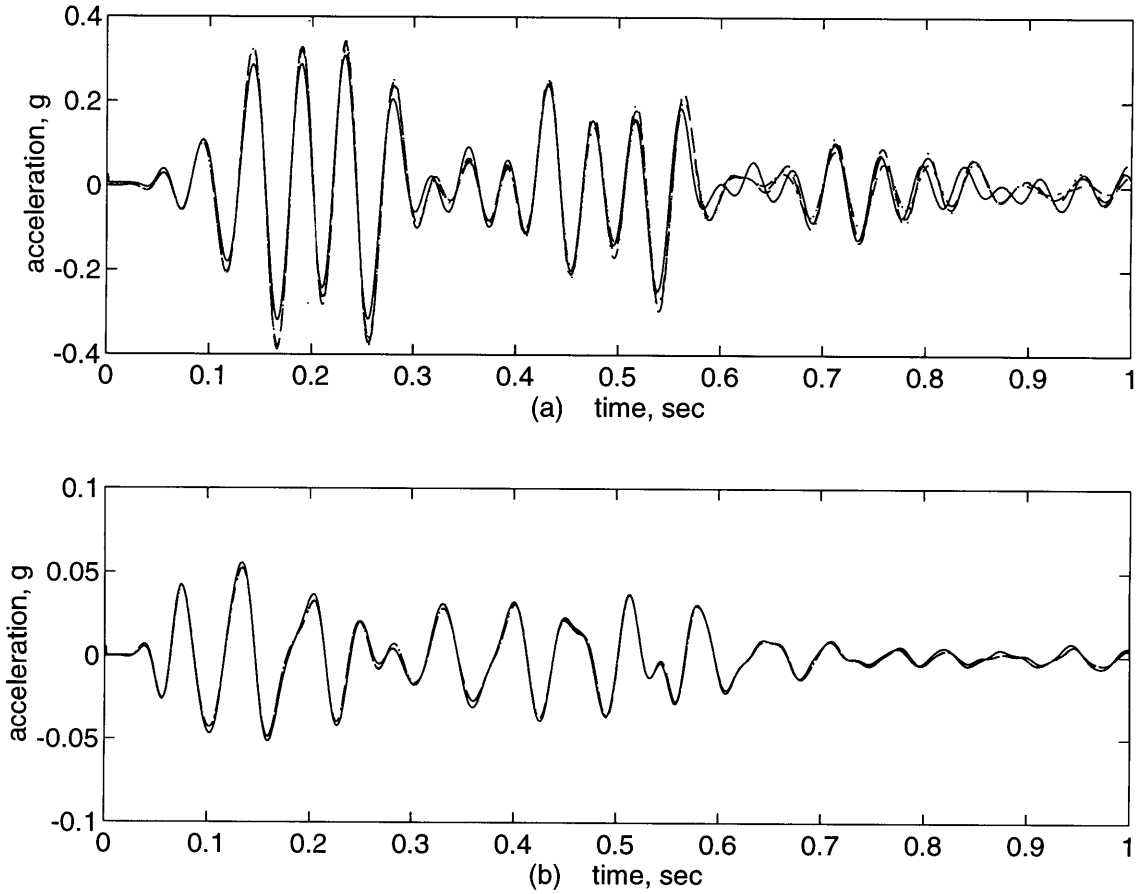

Figure 8.6: Response at (a) BV:5:+x, (b) BV:10:+z ; (—) measured, $(\cdots)$ full TMP, $(-\cdot)$ diagonal TMP, $(--)$ strain energy fraction, $(-\cdot\cdot)$ mass fraction.

Such a large quantity of data required FORTRAN programs to be written that could perform the necessary computations for a specified means of comparison.

One such program compared the methods on the basis of maximum and minimum values of response. These points tend to be driving factors in a loads analysis, and it is important that they be predicted accurately. The program found the maximum and minimum points for a given measurement as well as for the corresponding four predictions. Percent errors were then calculated between the predicted and measured maximum and between the predicted and measured minimum. The average of the absolute values of the two errors was stored for each prediction, and this was repeated for all 72 measurements. An overall average of the errors for a given prediction method (i.e., damping formulation) was then determined for tests without added damping, for tests with added damping, and finally for all tests. Table 8.3 shows the average error of the four formulations in each category. The full TMP method performed the best in all three categories, followed by the diagonal TMP, strain energy fraction, and mass fraction methods. When no added damping was present, both TMP methods yielded nearly identical results, but with added damping, the neglect of the off-diagonal terms appears to have led to a larger discrepancy. From a practical standpoint, the differences in the results are probably not significant. In fact, the use of any of the predicted maxima and minima should be acceptable.

Table 8.3: Average Percent Errors in Predicted Maxima and Minima

	Average % error		
Damping formulation	no added damping	added damping	all tests
Full TMP	16.18	13.17	14.68
Diagonal TMP	16.19	13.24	14.72
Strain energy fraction	16.58	13.41	14.99
Mass fraction	16.87	13.61	15.24

The second means of comparison looked at the entire time history instead of only two points. The cost of a given predicted response was defined to be

$$\text{cost} = \sum_{i=1}^{2048} (a_{\text{meas}}(t_i) - a_{\text{pred}}(t_i))^2 \tag{8.2}$$

At each time value, the predicted acceleration is subtracted from the measured acceleration,

and this result is squared. The cost is then determined by summing the squares over all points. Another program was written that computed the costs of the 288 analytical time histories and found averages for the same three categories mentioned above. The results are presented in Table 8.4. It should be mentioned that even though the values do not appear to change from one category to the next, there are differences if the numbers are written with more decimal places. The numbers do show that the full TMP method had the lowest cost, followed by the diagonal TMP, mass fraction, and strain energy fraction methods. One might argue that such small differences are negligible, but a definite trend seems to be developing, namely the better performance of the two TMP damping formulations.

Table 8.4: Average Cost

	Average cost		
Damping formulation	no added damping	added damping	all tests
Full TMP	1.001	1.001	1.001
Diagonal TMP	1.006	1.006	1.006
Strain energy fraction	1.026	1.026	1.026
Mass fraction	1.021	1.021	1.021

One problem with the cost function in Equation 8.2 is that large errors can accumulate if the two time histories being compared become out of phase. To compensate for this, as well as to provide an additional measure of comparison, a different cost function was defined. Instead of taking the sum of squares of differences, the new approach found the difference of sums of squares. This variation does not depend on phase information and can be expressed as

$$\text{cost} = \left| \frac{\sum_{i=1}^{2048} a^2_{\text{meas}}(t_i) - \sum_{i=1}^{2048} a^2_{\text{pred}}(t_i)}{\sum_{i=1}^{2048} a^2_{\text{meas}}(t_i)} \right| \tag{8.3}$$

The term in the denominator is used to normalize the error found in the numerator. This permits the relative costs of the predictions to be compared instead of the absolute costs. Table 8.5 contains the average costs of the different methods when the new definition is used. As before, the full TMP method has the lowest cost, followed by the diagonal TMP method. The remaining two methods come in third and fourth, but in a different order than before. Contrary to what would be expected, the cost of the diagonal TMP method actually drops when damping is added; however, it is higher than the full TMP cost. The differences are not any more significant than in the other two comparisons, but an undeniable trend has

Table 8.5: Average Cost (Different Cost Definition)

	Average cost		
Damping formulation	no added damping	added damping	all tests
Full TMP	0.3269	0.3269	0.3269
Diagonal TMP	0.3281	0.3276	0.3279
Strain energy fraction	0.3287	0.3287	0.3287
Mass fraction	0.3292	0.3296	0.3294

appeared. Using the fully-populated modal damping matrix from the TMP leads to better results on average. Ignoring the off-diagonal terms causes a slight decrease in prediction accuracy, but still performs better than the strain energy and mass fraction methods, which have comparable results. Some reasons for the fact that none of the methods emerged as a decisive winner are given in the following chapter, along with recommendations for further work that can provide additional information in this area.

Chapter 9

Conclusions and Recommendations

Some general conclusions can be drawn from the results that have been presented for all phases of the project. Not only can some important questions be answered, but new questions arise that require further research to address these issues. These topics are addressed in this chapter, and the scope of the project is summarized.

9.1 Discussion of Results

The major conclusion that can be reached upon examining the results of the transient response tests is that the four damping formulations did produce very similar response predictions. Any of the four could be used in other analyses and still yield fairly accurate results. This suggests that the use of an approximate diagonal system modal damping matrix is sufficient *in this case.* It should be emphasized that this conclusion cannot be extended to other structures in general. The structures that served as test articles in this project did not represent typical, complex structural systems. Rather, they were simple and symmetric, which resulted in well-defined modes. Even with the added viscoelastic material, the levels of damping remained in the light damping regime. The structures went from being severely lightly damped to being only lightly damped. Thus, these results are at most only applicable to systems exhibiting the same amount of complexity and damping.

Nevertheless, some interesting findings occurred in some of the analyses. The most important was the ability of the coupled damping (full TMP) approach to perform con-

sistently better than the other three damping formulations. This cannot be considered a coincidence since this result was obtained in three different methods of comparison, each of which utilized 72 measured responses. In addition, the diagonal TMP formulation, which is derived from the full TMP damping matrix, did only slightly worse on average. This seems to indicate that the off-diagonal terms did play a role, albeit minor. The results, however, were certainly not improved by neglecting these terms. Also, a clear division was visible in the comparisons between the TMP methods and the strain energy fraction and normalized mass fraction methods. The latter two yielded similar system damping ratios but were not as accurate in predicting the time histories or maxima and minima as the TMP approaches. If a guess was to be made prior to the damped tests concerning which formulation should lead to better results, the mass fraction method would probably have been chosen. The type of damping introduced into the system depends more on kinetic energy rather than strain energy, and so a derivation based on mass participation might be more accurate. Contrary to this belief, the mass fraction technique ranked last among the methods in two out of the three comparisons. This is not to say that the mass fraction method is a poor choice to use. For some reason, in the tests that were performed, it did not do as well on average as the other three, but as mentioned before, the differences being compared were minor.

Another contribution of the transient response portion of the project was the confirmation that the numerical integration of the equations of motion can produce accurate response predictions. The analytical time histories were able to follow the measured time histories extremely well, even for a random applied force. In a few instances, the predictions diverged from the measurements, but this cannot be attributed to the integration scheme. Some other phenomena probably contributed to the errors. No significant increase in computation time was observed when a fully-populated modal damping matrix was employed, and this is probably due to the relatively small model sizes and the use of a Cray Y-MP/EL computer.

Experimental verification was also made of the Component Mode Substitution Method. The predicted system modes were very close to the measured modes and exhibited good cross-orthogonality. The frequency errors increased slightly from the errors found in the substructures, but the majority was still below 2%. Such accuracy depended greatly on the success of the finite element model updates. The use of a truncated set of modes did

not cause any significant errors, mainly because the retained substructure modes had large participations in the low-frequency system modes. Furthermore, the implementation of mass loading allowed the measured BV modes to more closely resemble the interface-loaded analytical modes. This permitted the measured damping ratios to be more consistent with the damping associated with the analytical modes.

The FEM updates did not rely on mathematical approaches that blindly altered the mass and stiffness matrices. Instead, regions of uncertainty in the models were identified, and trial and error parameter changes were made based on a qualitative sensitivity analysis. This method did produce acceptable results in a short amount of time, but this can be attributed to an almost one-to-one correspondence between specific modes and parameters. Structures without such a relationship tend to require a more formal treatment of parameter sensitivities.

The procedure used in the mode survey tests resulted in a set of well-extracted modes for the substructures and the coupled system. Even though multiple SIMO tests were conducted in place of MIMO tests, the simplicity of the structures allowed a judiciously placed shaker in the direction of one of the axes to excite desired types of modes. In general, testing of complex spacecraft requires multiple shakers to excite along three axes simultaneously. The curve-fitting of the measured data was done in the time domain, as opposed to popular methods in the frequency domain, and the modal parameters remained consistent from test to test. The estimation of real, normal modes from measured complex modes utilized a method that is not mathematically correct for non-proportionally damped systems, but which was adequate for the slightly complex modes encountered in the project. The fact that the self-orthogonality checks of the measured substructure modes only had small errors enabled the use of an orthogonalization method to correct these errors. A critical assumption that was made was that the mass matrix was exact, which was a reasonable approximation under the circumstances.

9.2 Further Work

In light of the similar predicted responses obtained with the four damping formulations, as well as the small increase in performance seen in the full modal damping matrix approach, several recommendations for additional study can be made. The most obvious is to

increase the coupling between the system modes. The modes of BVSV had a good amount of separation between them, and this lack of modal density contributed to the relative insensitivity of the responses to the type of damping matrix used. In spite of the fact that the coupling index matrix had some rather large off-diagonal terms, the differences seen between methods were almost negligible. Two ways to increase the coupling would be to use either complex structures with high modal densities or highly-damped (but not necessarily complex) structures.

A means of examining the extent of coupling between a pair of modes is to determine how large the frequency separation is when compared to the bandwidth of each mode. An approximate measure of the bandwidth of a mode is given by $2\zeta\omega$, where ζ is the damping ratio of the mode and ω is the frequency. The probability of coupling is small whenever the condition

$$\frac{2\zeta\omega_i}{|\omega_i - \omega_j|} \ll 1 \tag{9.1}$$

is satisfied for a mode at ω_i and a nearby mode at ω_j. For the case of high modal density, the numerator will likely be small. For the case of high damping, the numerator will become large. In both instances, the fraction becomes large, and the condition might no longer be satisfied.

To illustrate these points, consider a simple two DOF example. Let the first mode have $\zeta_1 = 5\%$ and $f_1 = 10\,\text{Hz}$, and let the second mode have $\zeta_2 = 1\%$ and $f_2 = 15\,\text{Hz}$. Then the ratio given in Equation 9.1 becomes 0.2 with respect to the first mode. Figure 9.1 shows the transfer function of the system along with the two individual modal contributions. Now decrease the damping of the first mode to $\zeta_1 = 0.5\%$ and keep its frequency at $f_1 = 10\,\text{Hz}$. If the second mode has $\zeta_2 = 0.3\%$ and $f_2 = 10.5\,\text{Hz}$, then the ratio of Equation 9.1 is still equal to 0.2 for the first mode. The transfer functions appear in Figure 9.2.

Thus, two modes with sufficiently high damping can be separated in frequency by a fair amount (5 Hz in the example) and still be coupled by that damping. Otherwise, two modes must be extremely close (0.5 Hz in the example) to be coupled by light damping. From a practical standpoint, the addition of large amounts of damping to a given test article would be a better solution than trying to increase its modal density. Taking the test articles in the project as an example, major modifications would have to be made to them in order to yield a sufficiently complex structure. One possibility would be to redesign the floors

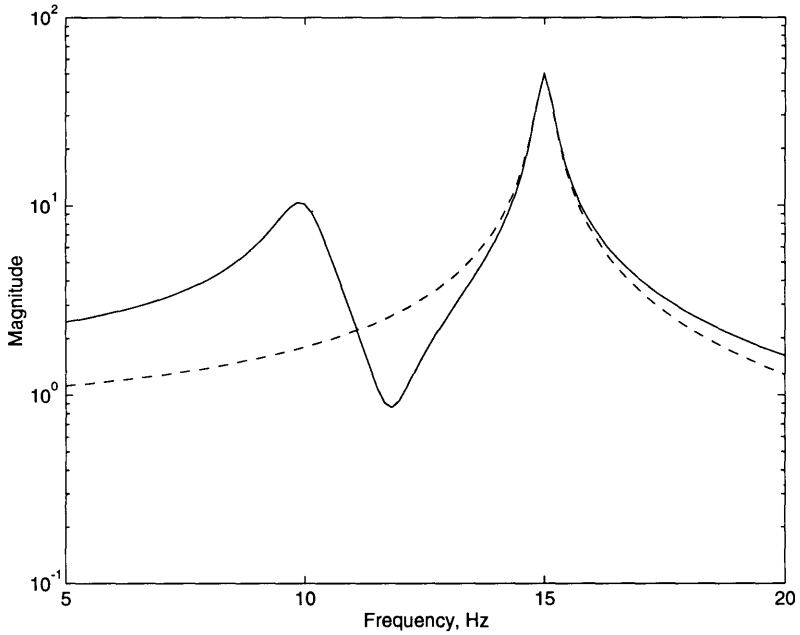

Figure 9.1: Transfer functions of mode 1 ($\cdots$), mode 2 ($--$), and system ($—$).

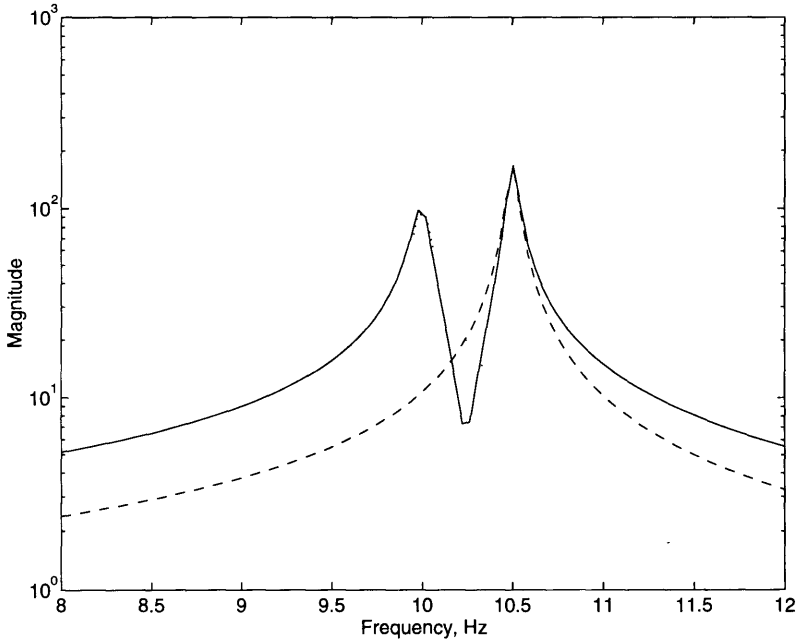

Figure 9.2: Transfer functions of mode 1 ($\cdots$), mode 2 ($--$), and system ($—$).

so that they had a square cross-section when viewed from above. By making the vertical aluminum beams also have a square cross section, the x and z bending modes would have nearly the same frequency since the structure would be almost symmetric about the vertical axis. Even small amounts of damping would be sufficient to cause coupling between the modes. This has the advantage of affecting many pairs of modes.

A slight modification that could also be done would be to try and tune the first antenna mode as close as possible to the first main bending mode. Adding weight to the tip masses would lower the antenna frequencies, and there would be a point when the out-of-phase antenna x-bending mode would coincide with the global x-bending mode. Damping would couple the two modes, and the predicted response of each tip mass might become more sensitive to the type of damping formulation used. A disadvantage would be that only two modes would be strongly coupled, while the other system modes would be neglected.

Increasing the level of damping found in the system was shown not to be a trivial undertaking. If possible, it will result in greater effects of non-proportional damping. An option that had been considered was to replace the vertical aluminum beams with two half-thickness beams that had a layer of VEM sandwiched between them. The use of constrained VEM is a very effective means of damping a structure. Another possibility is to incorporate struts which are damped along their extensional direction by built-in damping elements. The struts could connect adjacent floors, and any relative floor motion would dissipate energy in the dampers. These two methods would, however, change the mass and stiffness properties of the original undamped system, and no direct comparison could be made.

As the amount of damping is increased, new problems will be encountered. One is the estimation of real, normal modes from measured complex test modes. The amplitude normalization method used in this project will not yield accurate results for complex modes which have large imaginary parts. Highly damped modes will possess a high phase dispersion, and the assumption of proportional damping might lead to significant errors in the approximated real modes. If such a situation arises, then techniques such as the one presented in [1] should be utilized.

Another potential problem is that the assumption of proportional damping in the substructures might no longer be valid. The modal damping matrices of the substructures were forced to be diagonal by assuming each diagonal entry was of the form $2\zeta\omega$. For a highly damped substructure, the estimation of a full modal damping matrix might be required.

Such a task has been an object of study for many years (refer to [12] and [13] for several proposed methods); however, a problem that arises is that the modal damping matrix can be non-positive definite. Recently, a successful method was demonstrated experimentally in [1]. Although it is fairly complicated, it should lead to acceptable results.

9.3 Summary

This project analyzed several techniques to generate a system modal damping matrix from substructure test results. It was performed within the context of experimental substructure synthesis. Two test articles were assembled, and their dynamic properties were measured in a series of mode survey tests. Damping in the form of a constrained piece of viscoelastic material was added to one of the substructures in order to examine the effects of an increase in damping. Finite elements models of the structures were adjusted to better match the experimental modes, and the Component Mode Substitution (CMS) Method was employed to analytically couple the substructure models and predict the system modes. The test articles were physically joined, and tests were conducted on the coupled system to extract these modes. The analytical modes compared well with the measured modes for the system with and without the added damping. The system modal damping matrix was then generated via four formulations—a triple-matrix-product (TMP) approach consistent with the CMS Method, a diagonal matrix approach which neglected the off-diagonal elements of the TMP, a strain energy fraction method, and a normalized mass fraction method. Transient response testing was conducted on the system, and response predictions were made by integrating the equations of motion in modal coordinates. The different modal damping matrices were used in the analysis, and the resulting responses were compared to the measurements. In all cases, the damping formulations yielded almost identical results. With added damping in the system, the differences between methods were slightly more apparent, but they could not be considered significant. A probable reason for such similarity among the predictions is the lack of sufficient damping and modal density in the system. Such characteristics should make the responses more sensitive to the variations in the modal damping matrix.

Appendix A

NASTRAN Bulk Data

A.1 Updated BV Model Used For Coupling in the Added Damping Case

```
$############################## COMMENTS ###################################
$
$ The following NASTRAN Bulk Data Cards are used in the creation of
$ the finite element model of BV for the case of added damping. The
$ resulting mass and stiffness matrices are read by a program that
$ performs analytical substructure coupling.  The model differs from
$ the original one as follows:
$        - ASET1 cards specify the active set of DOF's onto which the
$          the mass and stiffness matrices are condensed.
$        - Various properties have been altered during the update
$          process.
$        - New grid points and RBAR's are introduced to allow for a
$          consistent interface with the SV coupling model.
$        - A soft spring is introduced at the location of the damping
$          treatment to account for the non-negligible stiffness.
$
$
$########################## BEGIN BULK DATA CARDS ########################
$
$
$ Specify a reduced set of DOF's
$
ASET1   123     6       8       10      13      15      17
ASET1   123     24      26      28      31      33      35
ASET1   123     42      44      46      49      51      53
```

```
$ These additional DOF's are for coupling compatibility
ASET1   123     424     464     494     534
$
$
$
$       ID      PBAR    1ST     2ND     REFERENCE
$       #       #       NODE    NODE    NODE
$-----------------------------------------------
CBAR    1       1       1       5       12
CBAR    2       2       7       8       15
CBAR    3       2       8       9       16
CBAR    4       1       11      2       4
CBAR    5       1       3       12      5
CBAR    6       2       14      15      8
CBAR    7       2       15      16      9
CBAR    8       1       18      4       2
CBAR    9       3       6       59      14
CBAR    91      3       59      13      14
CBAR    10      4       8       15      16
CBAR    11      3       10      17      16
CBAR    12      1       19      23      30
CBAR    13      2       25      26      33
CBAR    14      2       26      27      34
CBAR    15      1       29      20      22
CBAR    16      1       21      30      23
CBAR    17      2       32      33      26
CBAR    18      2       33      34      27
CBAR    19      1       36      22      20
CBAR    20      3       24      31      32
CBAR    21      4       26      33      34
CBAR    22      3       28      35      34
CBAR    23      1       37      41      48
CBAR    24      2       43      44      51
CBAR    25      2       44      45      52
CBAR    26      1       47      38      40
CBAR    27      1       39      48      41
CBAR    28      2       50      51      44
CBAR    29      2       51      52      45
CBAR    30      1       54      40      38
CBAR    31      3       42      49      50
CBAR    32      4       44      51      52
CBAR    33      3       46      53      52
$
$
$       ID      IND.    DEP.    DOFS
$       #       NODE    NODE
$-------------------------------------
RBAR    1       5       61      123456
```

```
RBAR     2        7        62       123456
RBAR     3        19       63       123456
RBAR     4        11       101      123456
RBAR     5        9        102      123456
RBAR     6        20       103      123456
RBAR     7        12       131      123456
RBAR     8        14       132      123456
RBAR     9        21       133      123456
RBAR     10       18       171      123456
RBAR     11       16       172      123456
RBAR     12       22       173      123456
RBAR     13       23       241      123456
RBAR     14       25       242      123456
RBAR     15       37       243      123456
RBAR     16       29       281      123456
RBAR     17       27       282      123456
RBAR     18       38       283      123456
RBAR     19       30       311      123456
RBAR     20       32       312      123456
RBAR     21       39       313      123456
RBAR     22       36       351      123456
RBAR     23       34       352      123456
RBAR     24       40       353      123456
RBAR     25       41       421      123456
RBAR     26       43       422      123456
RBAR     27       47       461      123456
RBAR     28       45       462      123456
RBAR     29       48       491      123456
RBAR     30       50       492      123456
RBAR     31       54       531      123456
RBAR     32       52       532      123456
RBAR     33       424      423      123456
RBAR     34       464      463      123456
RBAR     35       494      493      123456
RBAR     36       534      533      123456
$
$
$
$        ID       PELAS    1ST      DOF      2ND      DOF
$        #        #        NODE              NODE
$-----------------------------------------------------
CELAS1   301      1        1        1        55       1
CELAS1   302      2        1        2        55       2
CELAS1   303      3        1        3        55       3
CELAS1   304      4        1        4        55       4
CELAS1   305      5        1        5        55       5
CELAS1   306      6        1        6        55       6
CELAS1   307      25       2        1        56       1
```

```
CELAS1  308     26      2       2       56      2
CELAS1  309     27      2       3       56      3
CELAS1  310     28      2       4       56      4
CELAS1  311     29      2       5       56      5
CELAS1  312     30      2       6       56      6
CELAS1  313     1       3       1       57      1
CELAS1  314     2       3       2       57      2
CELAS1  315     3       3       3       57      3
CELAS1  316     4       3       4       57      4
CELAS1  317     5       3       5       57      5
CELAS1  318     6       3       6       57      6
CELAS1  319     25      4       1       58      1
CELAS1  320     26      4       2       58      2
CELAS1  321     27      4       3       58      3
CELAS1  322     28      4       4       58      4
CELAS1  323     29      4       5       58      5
CELAS1  324     30      4       6       58      6
CELAS1  325     7       61      1       6       1
CELAS1  326     8       61      2       6       2
CELAS1  327     9       61      3       6       3
CELAS1  328     10      61      4       6       4
CELAS1  329     11      61      5       6       5
CELAS1  330     12      61      6       6       6
CELAS1  331     7       101     1       10      1
CELAS1  332     8       101     2       10      2
CELAS1  333     9       101     3       10      3
CELAS1  334     10      101     4       10      4
CELAS1  335     11      101     5       10      5
CELAS1  336     12      101     6       10      6
CELAS1  337     7       131     1       13      1
CELAS1  338     8       131     2       13      2
CELAS1  339     9       131     3       13      3
CELAS1  340     10      131     4       13      4
CELAS1  341     11      131     5       13      5
CELAS1  342     12      131     6       13      6
CELAS1  343     7       171     1       17      1
CELAS1  344     8       171     2       17      2
CELAS1  345     9       171     3       17      3
CELAS1  346     10      171     4       17      4
CELAS1  347     11      171     5       17      5
CELAS1  348     12      171     6       17      6
CELAS1  349     7       241     1       24      1
CELAS1  350     8       241     2       24      2
CELAS1  351     9       241     3       24      3
CELAS1  352     10      241     4       24      4
CELAS1  353     11      241     5       24      5
CELAS1  354     12      241     6       24      6
CELAS1  355     7       281     1       28      1
```

```
CELAS1  356     8       281     2       28      2
CELAS1  357     9       281     3       28      3
CELAS1  358     10      281     4       28      4
CELAS1  359     11      281     5       28      5
CELAS1  360     12      281     6       28      6
CELAS1  361     7       311     1       31      1
CELAS1  362     8       311     2       31      2
CELAS1  363     9       311     3       31      3
CELAS1  364     10      311     4       31      4
CELAS1  365     11      311     5       31      5
CELAS1  366     12      311     6       31      6
CELAS1  367     7       351     1       35      1
CELAS1  368     8       351     2       35      2
CELAS1  369     9       351     3       35      3
CELAS1  370     10      351     4       35      4
CELAS1  371     11      351     5       35      5
CELAS1  372     12      351     6       35      6
CELAS1  373     7       421     1       42      1
CELAS1  374     8       421     2       42      2
CELAS1  375     9       421     3       42      3
CELAS1  376     10      421     4       42      4
CELAS1  377     11      421     5       42      5
CELAS1  378     12      421     6       42      6
CELAS1  379     7       461     1       46      1
CELAS1  380     8       461     2       46      2
CELAS1  381     9       461     3       46      3
CELAS1  382     10      461     4       46      4
CELAS1  383     11      461     5       46      5
CELAS1  384     12      461     6       46      6
CELAS1  385     7       491     1       49      1
CELAS1  386     8       491     2       49      2
CELAS1  387     9       491     3       49      3
CELAS1  388     10      491     4       49      4
CELAS1  389     11      491     5       49      5
CELAS1  390     12      491     6       49      6
CELAS1  391     7       531     1       53      1
CELAS1  392     8       531     2       53      2
CELAS1  393     9       531     3       53      3
CELAS1  394     10      531     4       53      4
CELAS1  395     11      531     5       53      5
CELAS1  396     12      531     6       53      6
CELAS1  397     7       6       1       63      1
CELAS1  398     8       6       2       63      2
CELAS1  399     9       6       3       63      3
CELAS1  400     10      6       4       63      4
CELAS1  401     11      6       5       63      5
CELAS1  402     12      6       6       63      6
CELAS1  403     7       10      1       103     1
```

```
CELAS1  404     8       10      2       103     2
CELAS1  405     9       10      3       103     3
CELAS1  406     10      10      4       103     4
CELAS1  407     11      10      5       103     5
CELAS1  408     12      10      6       103     6
CELAS1  409     7       13      1       133     1
CELAS1  410     8       13      2       133     2
CELAS1  411     9       13      3       133     3
CELAS1  412     10      13      4       133     4
CELAS1  413     11      13      5       133     5
CELAS1  414     12      13      6       133     6
CELAS1  415     7       17      1       173     1
CELAS1  416     8       17      2       173     2
CELAS1  417     9       17      3       173     3
CELAS1  418     10      17      4       173     4
CELAS1  419     11      17      5       173     5
CELAS1  420     12      17      6       173     6
CELAS1  421     7       24      1       243     1
CELAS1  422     8       24      2       243     2
CELAS1  423     9       24      3       243     3
CELAS1  424     10      24      4       243     4
CELAS1  425     11      24      5       243     5
CELAS1  426     12      24      6       243     6
CELAS1  427     7       28      1       283     1
CELAS1  428     8       28      2       283     2
CELAS1  429     9       28      3       283     3
CELAS1  430     10      28      4       283     4
CELAS1  431     11      28      5       283     5
CELAS1  432     12      28      6       283     6
CELAS1  433     7       31      1       313     1
CELAS1  434     8       31      2       313     2
CELAS1  435     9       31      3       313     3
CELAS1  436     10      31      4       313     4
CELAS1  437     11      31      5       313     5
CELAS1  438     12      31      6       313     6
CELAS1  439     7       35      1       353     1
CELAS1  440     8       35      2       353     2
CELAS1  441     9       35      3       353     3
CELAS1  442     10      35      4       353     4
CELAS1  443     11      35      5       353     5
CELAS1  444     12      35      6       353     6
CELAS1  445     13      6       1       62      1
CELAS1  446     14      6       2       62      2
CELAS1  447     15      6       3       62      3
CELAS1  448     16      6       4       62      4
CELAS1  449     17      6       5       62      5
CELAS1  450     18      6       6       62      6
CELAS1  451     13      10      1       102     1
```

```
CELAS1  452     14      10      2       102     2
CELAS1  453     15      10      3       102     3
CELAS1  454     16      10      4       102     4
CELAS1  455     17      10      5       102     5
CELAS1  456     18      10      6       102     6
CELAS1  457     13      13      1       132     1
CELAS1  458     14      13      2       132     2
CELAS1  459     15      13      3       132     3
CELAS1  460     16      13      4       132     4
CELAS1  461     17      13      5       132     5
CELAS1  462     18      13      6       132     6
CELAS1  463     13      172     1       17      1
CELAS1  464     14      172     2       17      2
CELAS1  465     15      172     3       17      3
CELAS1  466     16      172     4       17      4
CELAS1  467     17      172     5       17      5
CELAS1  468     18      172     6       17      6
CELAS1  469     13      24      1       242     1
CELAS1  470     14      24      2       242     2
CELAS1  471     15      24      3       242     3
CELAS1  472     16      24      4       242     4
CELAS1  473     17      24      5       242     5
CELAS1  474     18      24      6       242     6
CELAS1  475     13      28      1       282     1
CELAS1  476     14      28      2       282     2
CELAS1  477     15      28      3       282     3
CELAS1  478     16      28      4       282     4
CELAS1  479     17      28      5       282     5
CELAS1  480     18      28      6       282     6
CELAS1  481     13      31      1       312     1
CELAS1  482     14      31      2       312     2
CELAS1  483     15      31      3       312     3
CELAS1  484     16      31      4       312     4
CELAS1  485     17      31      5       312     5
CELAS1  486     18      31      6       312     6
CELAS1  487     13      35      1       352     1
CELAS1  488     14      35      2       352     2
CELAS1  489     15      35      3       352     3
CELAS1  490     16      35      4       352     4
CELAS1  491     17      35      5       352     5
CELAS1  492     18      35      6       352     6
CELAS1  493     13      42      1       422     1
CELAS1  494     14      42      2       422     2
CELAS1  495     15      42      3       422     3
CELAS1  496     16      42      4       422     4
CELAS1  497     17      42      5       422     5
CELAS1  498     18      42      6       422     6
CELAS1  499     13      46      1       462     1
```

```
CELAS1  500     14      46      2       462     2
CELAS1  501     15      46      3       462     3
CELAS1  502     16      46      4       462     4
CELAS1  503     17      46      5       462     5
CELAS1  504     18      46      6       462     6
CELAS1  505     13      49      1       492     1
CELAS1  506     14      49      2       492     2
CELAS1  507     15      49      3       492     3
CELAS1  508     16      49      4       492     4
CELAS1  509     17      49      5       492     5
CELAS1  510     18      49      6       492     6
CELAS1  511     13      53      1       532     1
CELAS1  512     14      53      2       532     2
CELAS1  513     15      53      3       532     3
CELAS1  514     16      53      4       532     4
CELAS1  515     17      53      5       532     5
CELAS1  516     18      53      6       532     6
CELAS1  517      7      42      1       423     1
CELAS1  518      8      42      2       423     2
CELAS1  519      9      42      3       423     3
CELAS1  520     10      42      4       423     4
CELAS1  521     11      42      5       423     5
CELAS1  522     12      42      6       423     6
CELAS1  523      7      46      1       463     1
CELAS1  524      8      46      2       463     2
CELAS1  525      9      46      3       463     3
CELAS1  526     10      46      4       463     4
CELAS1  527     11      46      5       463     5
CELAS1  528     12      46      6       463     6
CELAS1  529      7      49      1       493     1
CELAS1  530      8      49      2       493     2
CELAS1  531      9      49      3       493     3
CELAS1  532     10      49      4       493     4
CELAS1  533     11      49      5       493     5
CELAS1  534     12      49      6       493     6
CELAS1  535      7      53      1       533     1
CELAS1  536      8      53      2       533     2
CELAS1  537      9      53      3       533     3
CELAS1  538     10      53      4       533     4
CELAS1  539     11      53      5       533     5
CELAS1  540     12      53      6       533     6
CELAS1  541     19      59      1       591     1
CELAS1  542     20      59      2       591     2
CELAS1  543     21      59      3       591     3
CELAS1  544     22      59      4       591     4
CELAS1  545     23      59      5       591     5
CELAS1  546     24      59      6       591     6
$
```

```
$
$
CONM2   201     6               0.00272
        0.00231         0.00362                 0.00320
CONM2   202     10              0.00272
        0.00231         0.00362                 0.00320
CONM2   203     13              0.00272
        0.00231         0.00362                 0.00320
CONM2   204     17              0.00272
        0.00231         0.00362                 0.00320
CONM2   205     24              0.00272
        0.00231         0.00362                 0.00320
CONM2   206     28              0.00272
        0.00231         0.00362                 0.00320
CONM2   207     31              0.00272
        0.00231         0.00362                 0.00320
CONM2   208     35              0.00272
        0.00231         0.00362                 0.00320
CONM2   209     42              0.00272
        0.00231         0.00362                 0.00320
CONM2   210     46              0.00272
        0.00231         0.00362                 0.00320
CONM2   211     49              0.00272
        0.00231         0.00362                 0.00320
CONM2   212     53              0.00272
        0.00231         0.00362                 0.00320
$
$
$
EIGR    100     MGIV    0.0     70.0                                    +EIG
+EIG    MASS
$
$
$
$       ID              X       Y       Z
$       #               (in.)   (in.)   (in.)
$-----------------------------------------------
GRID    1               0.0     0.0     16.0
GRID    2               12.25   0.0     16.0
GRID    3               0.0     0.0     0.0
GRID    4               12.25   0.0     0.0
GRID    5               0.0     10.0    16.0
GRID    6               0.375   11.0    16.0
GRID    61              0.375   11.0    16.0
GRID    62              0.375   11.0    16.0
GRID    63              0.375   11.0    16.0
GRID    7               0.625   11.0    16.0
GRID    8               6.125   11.0    16.0
```

```
GRID     9               11.625  11.0    16.0
GRID     10              11.875  11.0    16.0
GRID     101             11.875  11.0    16.0
GRID     102             11.875  11.0    16.0
GRID     103             11.875  11.0    16.0
GRID     11              12.25   10.0    16.0
GRID     12              0.0     10.0    0.0
GRID     13              0.375   11.0    0.0
GRID     131             0.375   11.0    0.0
GRID     132             0.375   11.0    0.0
GRID     133             0.375   11.0    0.0
GRID     14              0.625   11.0    0.0
GRID     15              6.125   11.0    0.0
GRID     16              11.625  11.0    0.0
GRID     17              11.875  11.0    0.0
GRID     171             11.875  11.0    0.0
GRID     172             11.875  11.0    0.0
GRID     173             11.875  11.0    0.0
GRID     18              12.25   10.0    0.0
GRID     19              0.0     12.0    16.0
GRID     20              12.25   12.0    16.0
GRID     21              0.0     12.0    0.0
GRID     22              12.25   12.0    0.0
GRID     23              0.0     22.0    16.0
GRID     24              0.375   23.0    16.0
GRID     241             0.375   23.0    16.0
GRID     242             0.375   23.0    16.0
GRID     243             0.375   23.0    16.0
GRID     25              0.625   23.0    16.0
GRID     26              6.125   23.0    16.0
GRID     27              11.625  23.0    16.0
GRID     28              11.875  23.0    16.0
GRID     281             11.875  23.0    16.0
GRID     282             11.875  23.0    16.0
GRID     283             11.875  23.0    16.0
GRID     29              12.25   22.0    16.0
GRID     30              0.0     22.0    0.0
GRID     31              0.375   23.0    0.0
GRID     311             0.375   23.0    0.0
GRID     312             0.375   23.0    0.0
GRID     313             0.375   23.0    0.0
GRID     32              0.625   23.0    0.0
GRID     33              6.125   23.0    0.0
GRID     34              11.625  23.0    0.0
GRID     35              11.875  23.0    0.0
GRID     351             11.875  23.0    0.0
GRID     352             11.875  23.0    0.0
GRID     353             11.875  23.0    0.0
```

```
GRID    36              12.25   22.0    0.0
GRID    37              0.0     24.0    16.0
GRID    38              12.25   24.0    16.0
GRID    39              0.0     24.0    0.0
GRID    40              12.25   24.0    0.0
GRID    41              0.0     34.0    16.0
GRID    42              0.375   35.0    16.0
GRID    421             0.375   35.0    16.0
GRID    422             0.375   35.0    16.0
GRID    423             0.375   35.0    16.0
GRID    424             0.0     36.0    16.0
GRID    43              0.625   35.0    16.0
GRID    44              6.125   35.0    16.0
GRID    45              11.625  35.0    16.0
GRID    46              11.875  35.0    16.0
GRID    461             11.875  35.0    16.0
GRID    462             11.875  35.0    16.0
GRID    463             11.875  35.0    16.0
GRID    464             12.25   36.0    16.0
GRID    47              12.25   34.0    16.0
GRID    48              0.0     34.0    0.0
GRID    49              0.375   35.0    0.0
GRID    491             0.375   35.0    0.0
GRID    492             0.375   35.0    0.0
GRID    493             0.375   35.0    0.0
GRID    494             0.0     36.0    0.0
GRID    50              0.625   35.0    0.0
GRID    51              6.125   35.0    0.0
GRID    52              11.625  35.0    0.0
GRID    53              11.875  35.0    0.0
GRID    531             11.875  35.0    0.0
GRID    532             11.875  35.0    0.0
GRID    533             11.875  35.0    0.0
GRID    534             12.25   36.0    0.0
GRID    54              12.25   34.0    0.0
GRID    55              0.0     0.0     16.0            123456
GRID    56              12.25   0.0     16.0            123456
GRID    57              0.0     0.0     0.0             123456
GRID    58              12.25   0.0     0.0             123456
GRID    59              0.375   11.0    8.0
GRID    591             0.375   11.0    8.0             123456
$
$
$ DESCRIPTION OF PBAR  AND MATERIAL TYPES
$ -------------------------------------
$
$ PBAR  1 = VERTICAL ALUMINUM BEAMS
$ PBAR  2 = STEEL BEAMS, X DIRECTION
```

```
$ PBAR  3 = STEEL BEAMS, Z DIRECTION
$ PBAR  4 = STEEL PLATES (XZ PLANE)
$
$
$
$       #       E (psi)         NU      DENSITY (snails/in^3)
$-------------------------------------------------------------
MAT1    1       1.+7            0.33    0.000250
MAT1    2       3.+7            0.29    0.000701
MAT1    3       3.+7            0.29    0.000702
MAT1    4       3.+7            0.29    0.000699
$
PARAM,GRDPNT,0
PARAM,NEWSEQ,-1
PARAM,USETPRT,0
PARAM,AUTOSPC,YES
PARAM,COUPMASS,1
$ In the original model, the last card was omitted.  It was
$ discovered during the update process that using a consistent
$ mass matrix helped to improve the results for torsion modes.
$
$
$       #       MAT1    AREA    I1      I2      J
$                       (in^2)  (in^4)  (in^4)  (in^4)
$-----------------------------------------------------
PBAR    1       1       0.250   0.0208  0.0013  0.004
PBAR    2       2       1.0     0.0208  0.3333  0.070
PBAR    3       3       1.0     0.0208  0.3333  0.070
PBAR    4       4       3.0     9.0     0.0625  0.237
$
$
$
$ FLOOR JOINTS (GRIDS 1 AND 3)
PELAS   1       1.+10   0.0             2       1.+10   0.0
PELAS   3       1.+10   0.0             4       1.8+5   0.0
PELAS   5       1.+10   0.0             6       3.5+4   0.0
$ REGULAR JOINTS
PELAS   7       1.+10   0.0             8       1.+10   0.0
PELAS   9       1.+10   0.0             10      1.2+6   0.0
PELAS   11      1.+10   0.0             12      1.+5    0.0
$ INTERSECTION OF X AND Z STEEL FRAMES
PELAS   13      1.+10   0.0             14      1.+10   0.0
PELAS   15      1.+10   0.0             16      1.+10   0.0
PELAS   17      1.+10   0.0             18      1.+10   0.0
$ MODEL OF VISCOELASTIC ADDED STIFFNESS
PELAS   19      5.+1    0.0             20      0.0     0.0
PELAS   21      7.+1    0.0             22      0.0     0.0
PELAS   23      0.0     0.0             24      0.0     0.0
```

```
$ FLOOR JOINTS (GRIDS 2 AND 4)
PELAS   25      1.+10   0.0             26      1.+10   0.0
PELAS   27      1.+10   0.0             28      1.4+5   0.0
PELAS   29      1.+10   0.0             30      3.5+4   0.0
$
$
ENDDATA
```

A.2 Updated SV Model Used For Coupling

```
$################################ COMMENTS ################################
$
$ The following NASTRAN Bulk Data Cards are used in the creation of
$ the finite element model of SV. The resulting mass and stiffness
$ matrices are read by a program that performs analytical substructure
$ coupling.   The model differs from the original one as follows:
$        - ASET1 cards specify the active set of DOF's onto which the
$          the mass and stiffness matrices are condensed.
$        - The DOF's at the base are no longer fixed in order to have
$          mass and stiffness matrices for a free interface.
$        - Various properties have been altered during the update
$          process.
$
$
$########################## BEGIN BULK DATA CARDS ######################
$
$
ASET1   123     6       8       10      13      15      17      22
ASET1   123     19      25
ASET1   5       22      25
ASET1   123     28      29      30      31
$
$
$
$       ID      PBAR    1ST     2ND     REFERENCE
$       #       #       NODE    NODE    NODE
$-------------------------------------------------
CBAR    1       1       1       5       12
CBAR    2       2       7       8       15
CBAR    3       2       8       9       16
CBAR    4       1       11      2       4
CBAR    5       1       3       12      5
CBAR    6       2       14      15      8
CBAR    7       2       15      16      9
CBAR    8       1       18      4       2
CBAR    9       3       6       13      14
CBAR    10      5       26      19      23
CBAR    11      5       19      27      20
CBAR    12      3       10      17      16
CBAR    13      6       20      21      26
CBAR    14      6       23      24      27
$
$
$       ID      IND.    DEP.    DOFS
```

```
$       #       NODE    NODE
$-------------------------------------
RBAR    1       5       61      123456
RBAR    2       7       62      123456
RBAR    3       11      101     123456
RBAR    4       9       102     123456
RBAR    5       12      131     123456
RBAR    6       14      132     123456
RBAR    7       18      171     123456
RBAR    8       16      172     123456
RBAR    9       19      201     123456
RBAR    10      19      231     123456
RBAR    11      22      211     123456
RBAR    12      25      241     123456
RBAR    13      8       261     123456
RBAR    14      15      271     123456
$
$       ID      PELAS   1ST     DOF     2ND     DOF
$       #       #       NODE            NODE
$-----------------------------------------------
CELAS1  301     1       1       1       28      1
CELAS1  302     2       1       2       28      2
CELAS1  303     3       1       3       28      3
CELAS1  304     4       1       4       28      4
CELAS1  305     5       1       5       28      5
CELAS1  306     6       1       6       28      6
CELAS1  307     1       2       1       29      1
CELAS1  308     2       2       2       29      2
CELAS1  309     3       2       3       29      3
CELAS1  310     4       2       4       29      4
CELAS1  311     5       2       5       29      5
CELAS1  312     6       2       6       29      6
CELAS1  313     1       3       1       30      1
CELAS1  314     2       3       2       30      2
CELAS1  315     3       3       3       30      3
CELAS1  316     4       3       4       30      4
CELAS1  317     5       3       5       30      5
CELAS1  318     6       3       6       30      6
CELAS1  319     1       4       1       31      1
CELAS1  320     2       4       2       31      2
CELAS1  321     3       4       3       31      3
CELAS1  322     4       4       4       31      4
CELAS1  323     5       4       5       31      5
CELAS1  324     6       4       6       31      6
CELAS1  325     7       61      1       6       1
CELAS1  326     8       61      2       6       2
CELAS1  327     9       61      3       6       3
CELAS1  328     10      61      4       6       4
```

```
CELAS1  329     11      61      5       6       5
CELAS1  330     12      61      6       6       6
CELAS1  331     7       101     1       10      1
CELAS1  332     8       101     2       10      2
CELAS1  333     9       101     3       10      3
CELAS1  334     10      101     4       10      4
CELAS1  335     11      101     5       10      5
CELAS1  336     12      101     6       10      6
CELAS1  337     7       131     1       13      1
CELAS1  338     8       131     2       13      2
CELAS1  339     9       131     3       13      3
CELAS1  340     10      131     4       13      4
CELAS1  341     11      131     5       13      5
CELAS1  342     12      131     6       13      6
CELAS1  343     7       171     1       17      1
CELAS1  344     8       171     2       17      2
CELAS1  345     9       171     3       17      3
CELAS1  346     10      171     4       17      4
CELAS1  347     11      171     5       17      5
CELAS1  348     12      171     6       17      6
CELAS1  349     13      6       1       62      1
CELAS1  350     14      6       2       62      2
CELAS1  351     15      6       3       62      3
CELAS1  352     16      6       4       62      4
CELAS1  353     17      6       5       62      5
CELAS1  354     18      6       6       62      6
CELAS1  355     13      10      1       102     1
CELAS1  356     14      10      2       102     2
CELAS1  357     15      10      3       102     3
CELAS1  358     16      10      4       102     4
CELAS1  359     17      10      5       102     5
CELAS1  360     18      10      6       102     6
CELAS1  361     13      13      1       132     1
CELAS1  362     14      13      2       132     2
CELAS1  363     15      13      3       132     3
CELAS1  364     16      13      4       132     4
CELAS1  365     17      13      5       132     5
CELAS1  366     18      13      6       132     6
CELAS1  367     13      172     1       17      1
CELAS1  368     14      172     2       17      2
CELAS1  369     15      172     3       17      3
CELAS1  370     16      172     4       17      4
CELAS1  371     17      172     5       17      5
CELAS1  372     18      172     6       17      6
CELAS1  373     19      261     1       26      1
CELAS1  374     20      261     2       26      2
CELAS1  375     21      261     3       26      3
CELAS1  376     22      261     4       26      4
```

```
CELAS1  377     23      261     5       26      5
CELAS1  378     24      261     6       26      6
CELAS1  379     19      271     1       27      1
CELAS1  380     20      271     2       27      2
CELAS1  381     21      271     3       27      3
CELAS1  382     22      271     4       27      4
CELAS1  383     23      271     5       27      5
CELAS1  384     24      271     6       27      6
CELAS1  385     25      201     1       20      1
CELAS1  386     26      201     2       20      2
CELAS1  387     27      201     3       20      3
CELAS1  388     28      201     4       20      4
CELAS1  389     29      201     5       20      5
CELAS1  390     30      201     6       20      6
CELAS1  391     31      231     1       23      1
CELAS1  392     32      231     2       23      2
CELAS1  393     33      231     3       23      3
CELAS1  394     34      231     4       23      4
CELAS1  395     35      231     5       23      5
CELAS1  396     36      231     6       23      6
CELAS1  397     37      21      1       211     1
CELAS1  398     38      21      2       211     2
CELAS1  399     39      21      3       211     3
CELAS1  400     40      21      4       211     4
CELAS1  401     41      21      5       211     5
CELAS1  402     42      21      6       211     6
CELAS1  403     37      24      1       241     1
CELAS1  404     38      24      2       241     2
CELAS1  405     39      24      3       241     3
CELAS1  406     40      24      4       241     4
CELAS1  407     41      24      5       241     5
CELAS1  408     42      24      6       241     6
$
$
$
$
$ ADD ACCELEROMETER MASSES TO CONCENTRATED TIP MASSES;
$ INCREASE FROM 0.0026 TO 0.00268 FOR #201 AND #202
CONM2   201     22              0.00268
        0.00108         0.00173                 0.00108
CONM2   202     25              0.00268
        0.00108         0.00173                 0.00108
CONM2   203     6               0.00272
        0.00231         0.00362                 0.00320
CONM2   204     10              0.00272
        0.00231         0.00362                 0.00320
CONM2   205     13              0.00272
        0.00231         0.00362                 0.00320
```

```
CONM2   206     17              0.00272
        0.00231         0.00362                 0.00320
$
$
$
EIGR    100     MGIV    0.0     100.0                                   +EIG
+EIG    MASS
$
$
$
$       ID              X       Y       Z
$       #               (in.)   (in.)   (in.)
$-----------------------------------------------
GRID    1               0.0     0.0     16.0
GRID    2               12.25   0.0     16.0
GRID    3               0.0     0.0     0.0
GRID    4               12.25   0.0     0.0
GRID    5               0.0     10.0    16.0
GRID    6               0.375   11.0    16.0
GRID    61              0.375   11.0    16.0
GRID    62              0.375   11.0    16.0
GRID    7               0.625   11.0    16.0
GRID    8               6.125   11.0    16.0
GRID    9               11.625  11.0    16.0
GRID    10              11.875  11.0    16.0
GRID    101             11.875  11.0    16.0
GRID    102             11.875  11.0    16.0
GRID    11              12.25   10.0    16.0
GRID    12              0.0     10.0    0.0
GRID    13              0.375   11.0    0.0
GRID    131             0.375   11.0    0.0
GRID    132             0.375   11.0    0.0
GRID    14              0.625   11.0    0.0
GRID    15              6.125   11.0    0.0
GRID    16              11.625  11.0    0.0
GRID    17              11.875  11.0    0.0
GRID    171             11.875  11.0    0.0
GRID    172             11.875  11.0    0.0
GRID    18              12.25   10.0    0.0
GRID    19              6.125   11.0    8.0
GRID    20              6.125   10.75   8.0
GRID    201             6.125   10.75   8.0
$ Y VALUES CHANGED FROM 3.75 TO 3.8125 AND 3.25 to 3.3125
GRID    21              6.125   3.8125  8.0
GRID    211             6.125   3.8125  8.0
GRID    22              6.125   3.3125  8.0
$
GRID    23              6.125   11.25   8.0
```

```
GRID    231             6.125   11.25   8.0
$ Y VALUES CHANGED FROM 18.25 TO 18.3125 AND 18.75 to 18.8125
GRID    24              6.125   18.3125 8.0
GRID    241             6.125   18.3125 8.0
GRID    25              6.125   18.8125 8.0
$
GRID    26              6.125   11.0    14.75
GRID    261             6.125   11.0    14.75
GRID    27              6.125   11.0    1.25
GRID    271             6.125   11.0    1.25
GRID    28              0.0     0.0     16.0            46
GRID    29              12.25   0.0     16.0            46
GRID    30              0.0     0.0     0.0             46
GRID    31              12.25   0.0     0.0             46
$
$
$ DESCRIPTION OF PBAR  AND MATERIAL TYPES
$ -------------------------------------
$
$ PBAR  1 = VERTICAL ALUMINUM BEAMS
$ PBAR  2 = STEEL BEAMS, X DIRECTION
$ PBAR  3 = STEEL BEAMS, Z DIRECTION
$ PBAR  5 = HORIZONTAL SUPPORT BEAM FOR TIP MASS BEAM (ALUMINUM)
$ PBAR  6 = TIP MASS BEAM (ALUMINUM)
$
$
$
$       #       E (psi)         NU      DENSITY (snails/in^3)
$-----------------------------------------------------------
MAT1    1       1.+7            0.33    0.000250
MAT1    2       3.+7            0.29    0.000698
MAT1    3       3.+7            0.29    0.000702
MAT1    5       1.+7            0.33    0.000258
MAT1    6       1.+7            0.33    0.000291
$
PARAM,GRDPNT,0
PARAM,NEWSEQ,-1
PARAM,USETPRT,0
PARAM,AUTOSPC,YES
PARAM,COUPMASS,1
$ The last card was originally omitted before the update process.
$
$
$       #       MAT1    AREA    I1      I2      J
$                       (in^2)  (in^4)  (in^4)  (in^4)
$-------------------------------------------------
PBAR    1       1       0.250   0.0208  0.0013  0.004
PBAR    2       2       1.0     0.0208  0.3333  0.070
```

```
PBAR    3       3       1.0     0.0208  0.3333  0.070
PBAR    5       5       0.250   0.0052  0.0052  0.009
PBAR    6       6       0.0625  0.0013  8.E-5   0.0003
$
$
$
$ FLOOR JOINTS
PELAS   1       1.+10   0.0             2       1.+10   0.0
PELAS   3       1.+10   0.0             4       1.5+5   0.0
PELAS   5       1.+8    0.0             6       3.5+4   0.0
$ REGULAR JOINTS
PELAS   7       1.+10   0.0             8       1.+10   0.0
PELAS   9       1.+10   0.0             10      5.+5    0.0
PELAS   11      1.+10   0.0             12      1.+5    0.0
$ INTERSECTION OF X AND Z STEEL FRAMES
PELAS   13      1.+10   0.0             14      1.+10   0.0
PELAS   15      1.+10   0.0             16      1.+10   0.0
PELAS   17      1.+10   0.0             18      1.+10   0.0
$ ANGLED BRACKETS
PELAS   19      1.+10   0.0             20      1.+10   0.0
PELAS   21      1.+10   0.0             22      1.+10   0.0
PELAS   23      1.+10   0.0             24      1.+10   0.0
$ LOWER INTERSECTION OF SUPPORT BEAM AND TIP MASS BEAM
PELAS   25      1.+8    0.0             26      1.+8    0.0
PELAS   27      1.+8    0.0             28      1.8+4   0.0
PELAS   29      3.2+2   0.0             30      2.1+3   0.0
$ UPPER INTERSECTION OF SUPPORT BEAM AND TIP MASS BEAM
PELAS   31      1.+8    0.0             32      1.+8    0.0
PELAS   33      1.+8    0.0             34      2.4+4   0.0
PELAS   35      3.2+2   0.0             36      2.+3    0.0
$ CONNECTIONS BETWEEN END OF TIP MASS BEAMS AND TIP MASSES
PELAS   37      1.+8    0.0             38      1.+8    0.0
PELAS   39      1.+8    0.0             40      1.+8    0.0
PELAS   41      1.+6    0.0             42      1.+6    0.0
$
$
ENDDATA
```

Appendix B

FORTRAN Code

B.1 Program to Perform Component Mode Substitution

```
      SUBROUTINE MATCOMP
      COMMON / ERR / ITEST
C
C     PROGRAM TO COUPLE THE TWO SUBSTRUCTURE MODELS (SV,BV) AND PREDICT THE
C     SYSTEM MODES BY USING THE COMPONENT MODE SUBSTITUTION METHOD.  THIS
C     IS FOR THE UNDAMPED CASE.
C
C
      OPEN(30,FILE='sv2coup2.out4',FORM='UNFORMATTED')
C
C     sv2coup2 CONTAINS 2 ROTATIONAL DOF's
C
      OPEN(20,FILE='bv2coup.out4',FORM='UNFORMATTED')
C
      DO 10 I=10,12
         CALL NASMAT(30,I)       !     M_sv = 10, K_sv = 11
         CALL NASMAT(20,I+3)     !     M_bv = 13, K_bv = 14
 10   CONTINUE
C
C     DETERMINE NUMBER OF DOF'S FOR BOTH MODELS
C
      CALL SIZE(10,NDSV,NDSV)        ! NDSV = TOTAL # OF SV DOF'S
      NI = 12                        ! NI = # OF INTERFACE DOF'S
      NNISV = NDSV - NI              ! NNISV = # OF SV NONINTERFACE DOF'S
      CALL SIZE(13,NDBV,NDBV)        ! NDBV = TOTAL # OF BV DOF'S
      NNIBV = NDBV - NI              ! NNIBV = # OF BV NONINTERFACE DOF'S
C
C     OBTAIN THE SUBMATRICES K_NN AND K_NI OF THE FREE-FREE SV MODEL
```

```
C
      CALL EXTRACT(11,31,1,1,NNISV,NNISV)          ! K_NN = 31
      CALL EXTRACT(11,32,1,NNISV+1,NNISV,NI)       ! K_NI = 32
C
C     COMPUTE THE CONSTRAINT MODES, T_cb = -(K_NN^-1)*(K_NI)
C
      CALL INVSYM(31,1)
      CALL SCALAR(1,2,-1.0)
      CALL MULTI(2,32,33)       !    T_cb = 33
C
C     COMPUTE THE REDUCED INTERFACE COORDINATE MASS AND STIFFNESS MATRICES
C
      CALL SETDIAG(1,1.0,NI,NI)           ! CREATE IDENTITY MATRIX AND
      CALL ROWAUG(33,1,2)                 ! AUGMENT IT BELOW T_cb
      CALL TRIPROD(-2,10,34)              ! M_BAR = 34
      CALL TRIPROD(-2,11,35)              ! K_BAR = 35
C
C     "OVERLOAD" MASS AND STIFFNESS MATRICES OF BV WITH M_BAR AND K_BAR
C     AFTER GROUPING INTERFACE DOF'S
C
      CALL MOVE(13,36)
      CALL MOVE(14,37)
      CALL ADDIN(36,34,38,NNIBV+1,NNIBV+1)   ! M_bv (OVERLOADED) = 38
      CALL ADDIN(37,35,39,NNIBV+1,NNIBV+1)   ! K_bv (OVERLOADED) = 39
C
C     COMPUTE THE NORMAL MODES AND FREQUENCIES OF BV THAT INCLUDE
C     APPROXIMATE EFFECTS OF SV
C
      CALL DEVEC(39,38,40,41,0.0) ! EIGENVALUES = 40, VECTORS = 41
      CALL PRTFREQ(40,'bvmsldf')
C
C     USE A TRUNCATED SET OF MODES
C
      NA = 7     ! NA = NUMBER OF MODES USED FROM INTERFACE-LOADED BV MODEL
      CALL EXTRACT(40,42,1,1,NA,NA)        ! EXTRACT FIRST NA EIGENVALUES
      CALL EXTRACT(41,60,1,1,NDBV,NA)      ! EXTRACT FIRST NA EIGENVECTORS
C                                            PHI_pa = 60
      OPEN(69,FILE='bvmsrdmodes',FORM='UNFORMATTED')
      REWIND(69)
      CALL TRANSP(69,1)
      OPEN(20,FILE='bv2aset.out4',FORM='UNFORMATTED')
C
      DO 15 I=7,7
         CALL NASMAT(20,I)    !     M_bv = 7
 15   CONTINUE
      CALL MULTI(1,7,2)
      CALL EXTRACT(60,3,1,1,54,7)
      CALL TRIPROD(-3,7,8)
```

```
      CALL SQRTELM(8,9)
      CALL INVDIAG(9,8)
      CALL MULTI(3,8,4)
      CALL MULTI(2,4,1)
      CALL PRMAT(-1,-2,'bvxorth')
C
C     COMPUTE THE FIXED-INTERFACE NORMAL MODES OF SV
C
      CALL EXTRACT(10,43,1,1,NNISV,NNISV)    ! M_NN (SV) = 43
      CALL DEVEC(31,43,44,45,0.0) !
      CALL PRTFREQ(44,'sv freq')
C
C     USE A TRUNCATED SET OF SV MODES
C
      NB = 9        ! NB = NUMBER OF SV CANTILEVER MODES USED
      CALL EXTRACT(44,21,1,1,NB,NB)        ! EXTRACT FIRST NB EIGENVALUES
      CALL EXTRACT(45,22,1,1,NNISV,NB)     ! EXTRACT FIRST NB EIGENVECTORS
      CALL MOVE(22,45)                     ! PHIHAT_sv = 45
C
C     THE SYSTEM MODAL STIFFNESS MATRIX CONSISTS OF THE TWO SETS OF
C     EIGENVALUES PLACED ALONG THE DIAGONAL
C
      OPEN(46,FILE='kstar',FORM='UNFORMATTED')
      REWIND(46)
      CALL ADDIN(42,21,46,NA+1,NA+1)         ! K^* = 46
C
C     THE FOLLOWING STEPS PERFORM THE NECESSARY OPERATIONS TO FORM THE
C     SYSTEM MODAL MASS MATRIX
C
      CALL EXTRACT(60,47,NNIBV+1,1,NI,NA)     ! PHIBAR_pa = 47
      CALL EXTRACT(10,48,1,NNISV+1,NNISV,NI)  ! M_NI (SV) = 48
      CALL TRANSP(45,1)
      CALL MULTI(1,43,2)
      CALL MULTI(2,33,3)
      CALL MULTI(3,47,2)
      CALL MULTI(1,48,3)
      CALL MULTI(3,47,4)
      CALL ADD(2,4,49)                     ! M^* (LOWER LEFT CORNER) = 49
      CALL TRANSP(49,50)                   ! M^* (UPPER RIGHT CORNER) = 50
      CALL SETDIAG(51,1.0,NA+NB,NA+NB)
      CALL ADDIN(51,49,52,NA+1,1)
      OPEN(53,FILE='mstar',FORM='UNFORMATTED')
      REWIND(53)
      CALL ADDIN(52,50,53,1,NA+1)            ! M^* = 53
C
C     COMPUTE THE EIGENVALUES AND EIGENVECTORS USING K^* AND M^*
C
      CALL DEVEC(46,53,54,55,100000.0)
```

```
C
C
C     THE EIGENVALUES ARE THE SYSTEM CIRCULAR NATURAL FREQUENCIES SQUARED
C
      CALL PRTFREQ(54,10HFREQ      )
C
C     FORM C^* BY PLACING THE SUBSTRUCTURE DIAGONAL MODAL DAMPING MATRICES
C     ALONG ITS DIAGONAL.  THEN USE THE COMPUTED EIGENVECTORS TO OBTAIN THE
C     SYSTEM MODAL DAMPING MATRIX
C
      OPEN(65,FILE='bvmasslddmp2',FORM='UNFORMATTED')
      CALL SQRTELM(42,3)
      REWIND(12)
      OPEN(12,FILE='bvifl_w',FORM='UNFORMATTED')
      CALL MOVE(3,12)
      CALL SQRTELM(42,4)
      CALL MULTI(4,65,1)
      CALL SCALAR(1,2,0.02)
      OPEN(66,FILE='svmsrddamp',FORM='UNFORMATTED')
      CALL ADDIN(2,66,67,NA+1,NA+1)
      CALL EXTRACT(67,1,1,1,NA+5,NA+5)
      CALL EXTRACT(67,2,NA+6,NA+6,2,2)
      CALL NULL(67,NA+NB,NA+NB)
      CALL ADDIN(1,2,67,NA+8,NA+8)    ! C^* = 67
      CALL TRIPROD(-55,67,68)  ! <------- TMP METHOD USED HERE TO GENERATE
      CALL REORDE2(68,1,0)     !          SYSTEM MODAL DAMPING MATRIX
      CALL MOVE(1,68)
      CALL PRMAT(-68,0,'SYSDAMP')
C
C     COMPUTE % DIFFERENCE BETWEEN MEASURED AND PREDICTED VALUES OF SYSTEM
C     FREQUENCIES AND DAMPING
C
      OPEN(23,FILE='bvsvmsrdfreqs',FORM='UNFORMATTED')
      OPEN(24,FILE='bvsvmsrddamp',FORM='UNFORMATTED')
      NBVSV = 12                ! NBVSV = # OF MEASURED SYSTEM MODES
      CALL REORDE2(54,1,0)
      CALL SQRTELM(1,2)
      CALL MOVE(2,1)
      CALL EXTDIAG(68,3)
      CALL PRMAT(-23,-2,'BVSVFRE')
      CALL SCALAR(23,8,6.28318530718)
      CALL SUBTRAC(1,8,2)
      CALL DIVEBYE(2,8,4)
      CALL SCALAR(4,7,100.0)
      CALL PRMAT(-7,-3,'FR%DIFF')
      CALL DIVEBYE(3,1,4)
      CALL SCALAR(4,7,50.0)
      CALL PRMAT(-7,-3,'PREDDMP')
```

```
      CALL DIVEBYE(24,8,4)
      CALL SCALAR(4,9,50.0)
      CALL PRMAT(-9,-3,'MSRDDMP')
      CALL SUBTRAC(7,9,2)
      CALL DIVEBYE(2,9,4)
      CALL SCALAR(4,7,100.0)
      CALL PRMAT(-7,-3,'DM%DIFF')
C
C     THE EIGENVECTORS NEED TO BE TRANSFORMED TO PHYSICAL COORDINATES WITH
C     REDUNDANT DOF'S REMOVED
C
      CALL MULTI(33,47,1)
      CALL ADDIN(60,1,2,NDBV+1,1)
      CALL ADDIN(2,45,1,NDBV+1,NA+1)
      CALL ADDIN(1,47,56,NDBV+NNISV+1,1)         ! T5 = 56
      CALL MULTI(56,55,57)                       ! SYSTEM MODES = 57
      CALL SETDIAG(58,1.0,NDBV+NNISV,NDBV+NDSV)  ! T6 = 58
      CALL MULTI(58,57,59)   ! SYSTEM MODES WITH REDUNDANT DOF'S REMOVED
C
C     PERFORM CROSS-ORTHOGONALITY CHECK BETWEEN COUPLED MODES AND MEASURED
C     SYSTEM MODES
C
      CALL REORDE2(59,62,0)  ! REORDER COUPLED MODES TO MATCH SYSTEM MODES
      OPEN(26,FILE='bvsv2aset.out4',FORM='UNFORMATTED')
      DO 20 I=27,27
         CALL NASMAT(26,I)    ! M = 27
 20   CONTINUE
      CALL REORDE2(27,3,0)   ! REORDER NASTRAN MASS MATRIX
C
C     NORMALIZE MODES
C
      CALL TRIPROD(-62,3,7)
      CALL SQRTELM(7,8)
      CALL INVDIAG(8,9)
      CALL MULTI(62,9,4)
      CALL TRANSP(4,1)
      CALL MULTI(1,3,2)
      OPEN(28,FILE='bvsvmsrdmodes',FORM='UNFORMATTED')
      CALL TRIPROD(-28,3,7)
      CALL PRMAT(-7,-2,'ORTHO')
      CALL MULTI(2,28,61)
      CALL PRMAT(-61,-2,'XORTHO')
      OPEN(29,FILE='mode_partic',FORM='UNFORMATTED')
      REWIND(29)
      CALL MOVE(55,29)
      OPEN(19,FILE='system_w2',FORM='UNFORMATTED')
      REWIND(19)
      CALL MOVE(54,19)
```

```
      OPEN(25,FILE='damping_synth',FORM='UNFORMATTED')
      REWIND(25)
      CALL MOVE(68,25)
      OPEN(17,FILE='synth_modes',FORM='UNFORMATTED')
      REWIND(17)
      CALL MOVE(4,17)
      RETURN
      END
```

B.2 Portion of Diagonal Damping Program

```
C
C     THE FOLLOWING LINES OF CODE ARE FOUND IN THE PROGRAM THAT CREATES
C     DIAGONAL MODAL DAMPING MATRICES USING THE DIAGONAL TMP METHOD, THE
C     STRAIN ENERGY FRACTION METHOD, AND THE NORMALIZED MASS FRACTION
C     METHOD
C     DATASET KEY: 19 = FULL SYSTEM MODAL DAMPING MATRIX FROM TMP
C                  33 = ZETA_BV (MEASURED MASS LOADED)
C                  34 = ZETA_SV (MEASURED)
C                  35 = BV MODE PARTICIPATION MATRIX
C                  36 = SV MODE PARTICIPATION MATRIX
C                  37 = BV OMEGA^2 (INTERFACE-LOADED)
C                  38 = SV OMEGA^2
C                  39 = SYSTEM OMEGA
C                  42 = SYSTEM OMEGA^2
C
C
C     DIAGONAL TMP METHOD
C
      CALL EXTDIAG(19,1)    ! EXTRACT DIAGONAL
      OPEN(23,FILE='diagdamping_synthd',FORM='UNFORMATTED')
      REWIND(23)
      CALL MOVE(1,23)
C
C     STRAIN ENERGY FRACTION METHOD
C
      CALL MULTI(37,33,1)
      CALL TRIPROD(-35,1,2)
      CALL MULTI(38,34,3)
      CALL TRIPROD(-36,3,4)
      CALL ADD(2,4,7)
      CALL DIVEBYE(7,42,8)
      CALL EXTDIAG(8,9)
      CALL PRMAT(-9,-8,'zeta se')
      CALL MULTI(9,39,1)
```

```
      CALL SCALAR(1,2,2.0)
      OPEN(24,FILE='damping_se',FORM='UNFORMATTED')
      REWIND(24)
      CALL MOVE(2,24)
C
C     NORMALIZED MASS FRACTION METHOD
C
      CALL EXTRACT(40,1,1,1,NBV,NBV)          ! 1 = MSTAR_BB
      CALL EXTRACT(40,2,1,NBV+1,NBV,NSV)      ! 2 = MSTAR_BS
      CALL EXTRACT(40,3,NBV+1,1,NSV,NBV)      ! 3 = MSTAR_SB
      CALL EXTRACT(40,4,NBV+1,NBV+1,NSV,NSV)  ! 4 = MSTAR_SS
      CALL MULTI(1,35,7)                !   / \
      CALL MULTI(2,36,8)                !    |
      CALL ADD(7,8,9)                   !    |
      CALL SQRTELM(37,50)               !    BV
      CALL MULTI(50,33,51)              !  PORTION
      CALL MULTI(51,9,52)               !    |
      CALL TRANSP(35,53)                !    |
      CALL MULTI(53,52,54)              !   \ /
      CALL MULTI(3,35,7)                !   / \
      CALL MULTI(4,36,8)                !    |
      CALL ADD(7,8,9)                   !    |
      CALL SQRTELM(38,50)               !    SV
      CALL MULTI(50,34,51)              !  PORTION
      CALL MULTI(51,9,52)               !    |
      CALL TRANSP(36,53)                !    |
      CALL MULTI(53,52,55)              !   \ /
      CALL ADD(54,55,56)
      CALL DIVEBYE(56,39,57)
      CALL EXTDIAG(57,58)
      CALL PRMAT(-58,-8,'zeta mf')
      CALL MULTI(58,39,1)
      CALL SCALAR(1,2,2.0)
      OPEN(25,FILE='damping_mf',FORM='UNFORMATTED')
      REWIND(25)
      CALL MOVE(2,25)
```

Bibliography

[1] E. Balmès. *Experimental/Analytical Predictive Models of Damped Structural Dynamics.* PhD thesis, Massachusetts Intstitute of Technology, 1993.

[2] E. Balmès. A finite element updating procedure using frequency response functions: Applications to the MIT/SERC interferometer testbed. *International Modal Analysis Conference*, pages 176–182, 1993.

[3] W.A. Benfield and R.F. Hruda. Vibration analysis of structures by component mode substitution. *AIAA Journal*, 9(7):1255–1261, 1971.

[4] T.K. Caughey. Classical normal modes in damped linear dynamic systems. *ASME Journal of Applied Mechanics*, pages 269–271, 1960.

[5] Jay-Chung Chen. Evaluation of spacecraft modal test methods. *Journal of Spacecraft and Rockets*, 24(1):52–62, 1986.

[6] R. R. Craig, Jr. *Structural Dynamics: An Introduction to Computer Methods.* John Wiley & Sons, New York, 1981.

[7] R.R. Craig, Jr. A review of time-domain and frequency-domain component-mode synthesis methods. *Journal of Experimental and Analytical Modal Analysis*, 2(2):59–72, 1987.

[8] R.R. Craig, Jr. and M.C.C. Bampton. Coupling of substructures for dynamic analyses. *AIAA Journal*, 6(7):1313–1319, 1968.

[9] D.J. Ewins. *Modal Testing: Theory and Practice.* John Wiley & Sons, Inc., New York, 1984.

[10] R.J Guyan. Reduction of mass and stiffness matrices. *AIAA Journal*, 3(2):380, 1965.

[11] N.W. Hagood and A. von Flotow. Damping of structural vibrations with piezoelectric materials and passive electrical networks. *Journal of Sound and Vibration*, 146(2):243–268, 1991.

[12] T.K. Hasselman. Method for constructing a full modal damping matrix from experimental measurements. *AIAA Journal*, 10(4):526–527, 1972.

[13] T.K. Hasselman, J.D. Chrostowski, and R. Pappa. Estimation of full modal damping matrices from complex test modes. In *Proceedings of the 34th AIAA/ASME/AHS/ASC Structures, Structural Dynamics and Materials Conference*, pages 3388–3398, April 1993. AIAA Paper No. 93-1668-CP.

[14] J. He and D.J. Ewins. Compatibility of measured and predicted vibration modes in model improvement studies. *AIAA Journal*, 29(5):798–803, 1991.

[15] R.M. Hintz. Analytical methods in component modal synthesis. *AIAA Journal*, 13(8):1007–1016, 1975.

[16] C. Hsiao and M.C. Kim. Dynamic loads analysis of non-classically damped structures. ASME Paper presented at 1993 ASME Winter Annual Meeting.

[17] W.C. Hurty. Dynamic analysis of structural systems using component modes. *AIAA Journal*, 3(4):678–685, 1965.

[18] S.R. Ibrahim. Computation of normal modes from identified complex modes. *AIAA Journal*, 21(3):446–451, 1983.

[19] A.M. Kabe. Stiffness matrix adjustment using mode data. *AIAA Journal*, 23(9):1431–1436, 1985.

[20] Leuven Measurements and Systems, Leuven, Belgium. *LMS CADA-X Software: The Integrated Solution for Computer Aided Dynamic Testing and Analysis*, 1993.

[21] C.S. Lin. Location of modeling errors using modal test data. *AIAA Journal*, 28(9):1650–1654, 1990.

[22] L. Meirovitch. *Elements of Vibration Analysis.* McGraw-Hill, Inc., New York, 1986.

[23] S. Park, I. Park, and F. Ma. Decoupling approximation of nonclassically damped structures. *AIAA Journal*, 30(9):2348–2351, 1992.

[24] N.A. Roy, A. Girard, and L.-P. Bugeat. Expansion of experimental mode shapes—An improvement of the projection technique. *International Modal Analysis Conference*, pages 152–158, 1993.

[25] S. Rubin. Improved component-mode representation for structural dynamic analysis. *AIAA Journal*, 13(8):995–1006, 1975.

[26] W.P. Targoff. Orthogonality check and correction of measured modes. *AIAA Journal*, 14(2):164–167, 1976.

[27] N. Tengler. Damping method updates for STS/payload dynamic analysis: Background. Briefing given at Technical Interchange Meeting at Rockwell International (Downey, CA) on March 19, 1991.

[28] G.B. Warburton and S.R. Soni. Errors in response calculations for non-classically damped structures. *Earthquake Engineering Structural Dynamics*, 5:365–376, 1977.

[29] K. Xu and T. Igusa. Dynamic characteristics of non-classically damped structures. *Earthquake Engineering Structural Dynamics*, 20:1127–1144, 1991.